

Optimal Radio Resource Management for ISAC Under Imperfect Information: A Resource Economy-Driven Perspective

Luis F. Abanto-Leon and Setareh Maghsudi



Abstract—This work investigates the radio resource management (RRM) design for downlink integrated sensing and communications (ISAC) systems, jointly optimizing timeslot allocation, beam adaptation, functionality selection, and user-target pairing, with the goal of economizing resource consumption under imperfect information. Timeslot allocation assigns a number of discrete channel uses to targets and users, while beam adaptation selects transmit and receive beams with suitable directions, power levels, and beamwidths. Functionality selection determines whether each timeslot is used for sensing, communication, or their simultaneous operation, while user-target pairing specifies which users and targets are jointly served within the same timeslot. To ensure reliable operation, information imperfections arising from motion, quantization, feedback delays, and hardware limitations are considered. Resource economization is achieved by minimizing energy and time consumption through a multi-objective function, with strict prioritization of time savings.

The resulting RRM problem is formulated as a semi-infinite, nonconvex mixed-integer nonlinear program (MINLP). Given the lack of generic methods for solving such problems, we propose a tailor-made approach that exploits the underlying structure of the problem to uncover hidden convexities. This enables an exact reformulation as a mixed-integer semidefinite program (MISDP), which can be solved to global optimality. Simulations reveal important interdependencies among the considered RRM components and show that the proposed approach achieves substantial performance improvements over baseline schemes, with gains up to 88%.

Index Terms—Integrated sensing and communications, radio resource management, beam adaptation, timeslot allocation, functionality selection, user-target pairing, imperfect information.

1 INTRODUCTION

Integrated sensing and communications (ISAC) marks a groundbreaking advancement in wireless technology by seamlessly combining sensing and communications functionalities within the same hardware, spectrum, and waveform [1], [2]. This tight integration promises to maximize radio resource utilization efficiency and reduce costs, enabling enhanced performance and capabilities across a wide range of applications [3].

Millimeter-wave and terahertz frequencies offer compelling advantages for both sensing and communications. Their shorter wavelengths enable finer angular resolution

and higher Doppler sensitivity, which translate into improved localization accuracy, enhanced target discrimination, and high-resolution imaging [4]. These frequencies also provide access to vast amounts of underutilized spectrum, facilitating high-throughput communications [5]. This dual benefit has motivated numerous studies to explore the synergy between ISAC and higher frequency bands as a key enabler for fulfilling the stringent and diverse requirements of next-generation wireless networks [6]–[8].

Unlocking the full potential of ISAC at high frequencies hinges on the effectiveness of radio resource management (RRM) design. Beamforming stands out as a crucial enabler among ISAC’s RRM components, drawing significant attention across a wide range of applications, including multicasting [8], [9], autonomous driving [10], [11], physical-layer security [12], [13], and industrial IoT [14]. While digital beamforming offers fine-grained control over the beampattern, its hardware complexity and power consumption scale unfavorably with both operating frequency and array size, making it impractical for large antenna arrays at millimeter-wave and terahertz frequencies [15]–[17]. In this context, analog beamforming constitutes an attractive alternative due to its superior energy and cost efficiency. Although its beampattern control is inherently more constrained, analog beamforming aligns well with current and near-term high-frequency hardware capabilities and can still deliver competitive performance when combined with appropriate beam selection strategies.

Motivated by this, numerous studies on analog beamforming for ISAC have focused on beam selection as a central design mechanism [18], [19]. However, most existing works optimize only the beam direction while assuming constant power and constant beamwidth, e.g., [20], [21]. Such assumptions can be restrictive, as ISAC systems must accommodate heterogeneous user and target requirements, necessitating beams with adaptive power and beamwidth. While some works explored power control, e.g., [22]–[24], they assumed infinitesimal power resolution, which is incompatible with the discrete power levels supported by practical hardware. Beamwidth adaptation has received even less attention within ISAC [25], [26], despite its established role in communication systems, e.g., [27]–[29]. Moreover, existing ISAC beamforming research has predominantly focused on the transmit side, often overlooking the

Luis F. Abanto-Leon and Setareh Maghsudi are affiliated to Ruhr University Bochum, with emails luis.abantoleon@ruhr-uni-bochum.de and setareh.maghsudi@ruhr-uni-bochum.de.

Accepted for publication in IEEE Transactions on Mobile Computing. © 2026 IEEE. Personal use of this material is permitted. Permission from IEEE must be obtained for all other uses, in any current or future media, including reprinting/republishing this material for advertising or promotional purposes, creating new collective works, for resale or redistribution to servers or lists, or reuse of any copyrighted component of this work in other works.

receive side, which is critical for effective self-interference management [30], [31]. *This highlights the need for a comprehensive ISAC RRM design that jointly adapts beam direction, power, and beamwidth for both transmit and receive sides, while maintaining strong practical relevance.*

From a system-level perspective, another fundamental aspect of analog beamforming is time allocation. Owing to the shared radio-frequency (RF) chain inherent to analog architectures, the system cannot support the simultaneous handling of multiple data streams, which makes time-sharing an essential design consideration. Although time allocation has been studied extensively in standalone sensing e.g., [32], [33], and communication systems, e.g., [34], [35], its integration into ISAC remains limited, e.g., [22], [36]. Notably, [36] considered continuous-time allocation, whereas [22] examined discrete-time allocation. The latter is particularly relevant for practical systems, as it aligns with the discretized frame structures of modern wireless standards and facilitates flexible timeslot sharing among users and targets. *Thus, timeslot allocation becomes essential for meeting heterogeneous sensing and communication demands in analog beamforming-based ISAC systems, highlighting the need for RRM designs that explicitly account for this key resource.*

While the concurrent operation of sensing and communication is commonly assumed in the literature, enforcing this requirement can reduce flexibility and degrade performance, as the two functionalities may not always be jointly feasible or efficient, given system requirements and resource constraints. To alleviate this, a few studies explored adaptive functionality selection strategies. For instance, [37] considered mutually exclusive sensing and communication operation, while [8] introduced a priority-based approach in which one functionality is opportunistically enabled according to predefined hierarchies. However, these approaches did not account for the temporal domain of resources and lack support for flexible functionality selection, where each timeslot can be dynamically assigned to sensing, communication, or their simultaneous operation. *Hence, incorporating flexible, timeslot-level functionality selection into the RRM design is essential for improving performance, as it enables the system to dynamically determine the active functionalities in each timeslot based on instantaneous requirements and resource availability.*

Most existing studies assumed that user-target pairs are predetermined and provided as prior information. However, recent research, e.g., [38]–[40], has demonstrated that optimizing user-target pairing can significantly enhance system efficiency. Despite this progress, most of these studies, e.g., [38], [39], assumed independent waveforms for communication and sensing, failing to fully exploit the benefits of single-waveform ISAC. An exception is [40], which addressed user-target pairing under a single-waveform assumption, albeit restricted to a single channel use. *Incorporating dynamic user-target pairing is essential, particularly under resource-constrained conditions, as optimally pairing users and targets to share a common waveform can significantly improve system performance and reduce overall resource consumption.*

Information available for RRM design is often compromised by errors caused by factors such as motion, quantization, feedback delay, and hardware deficiencies. Despite their relevance, these errors are frequently overlooked in ISAC literature, with only a few exceptions accounting for

them, e.g., [36], [41]–[44]. Such errors can result in imperfect estimations of channel state information (CSI) [41], [42], angle of departure (AOD) [36], [42], reflection coefficient (RC) [36], [43], and residual self-interference (RSI) [44]. Ignoring potential imperfections in the RRM design can lead to infeasible solutions, thereby resulting in degraded system performance, unmet quality-of-service requirements, and frequent, inefficient resource re-allocations. *Therefore, robust RRM formulations that explicitly account for information uncertainty are essential to ensure stable and reliable ISAC operation.*

Adopting an economy-driven perspective in RRM design is essential for achieving efficient radio resource utilization. While a substantial body of ISAC literature has focused on minimizing energy consumption, owing to its direct impact on interference mitigation and carbon footprint reduction, e.g., [43], [45], [46], other critical resources, particularly time, remain understudied. Minimizing time resource consumption is essential not only for meeting latency requirements in time-sensitive applications, but also because analog beamforming supports only a single signal stream at a time. *Hence, the joint minimization of time and energy consumption is paramount for achieving resource efficiency and for provisioning ISAC systems to meet future demands.*

Building on the above motivation, this paper advances the ISAC literature by investigating a novel and comprehensive RRM problem with unique characteristics. Particularly, **Table A.1 in Appendix A** presents a detailed comparison of our work against existing literature¹. The key contributions of this work are as follows.

- To address the inherent limitation of analog beamforming in supporting only a single data stream at a time, we introduce a timeslot allocation mechanism that efficiently assigns timeslots to users and targets according to their specific service requirements. In parallel, we optimize beam adaptation on a per-timeslot basis, including direction, power, and beamwidth, at both the transmit and receive sides, by employing a column-generation approach and formulating beam selection as a multiple-choice constraint.
- To enable flexible control over sensing and communication operations, we incorporate timeslot-level functionality selection that allows each timeslot to be allocated exclusively to sensing, communication, or both. Furthermore, motivated by recent evidence on the benefits of optimized user-target pairing, we extend the pairing process to a dynamic, per-timeslot basis, thereby further enhancing overall system efficiency.
- To ensure reliability under practical imperfections, we develop a robust design accounting for uncertainties in CSI, AOD, RC, and RSI. We also introduce a multi-objective function that jointly minimizes energy and time consumption. Energy consumption is modeled as the sum of transmit and receive energies, while time consumption is modeled as a weighted sum of timeslots, with weights designed to promote contiguous allocation and improve temporal cohesion. The multi-objective function is then transformed into a weighted trade-off function, allowing the concurrent optimization of energy and time consumption.

1. This paper includes an appendix that provides additional material.

- Integrating the above elements, we formulate a comprehensive RRM problem as a semi-infinite, nonconvex mixed-integer nonlinear program (MINLP), posing significant challenges for its solution. To address this, we propose a tailored solution approach that exploits the problem structure to uncover hidden convexities, enabling an exact reformulation as a mixed-integer semidefinite program (MISDP) solvable to global optimality using general-purpose solvers.
- We evaluate the proposed RRM framework under a wide range of parameter settings and varying levels of imperfections to demonstrate its robustness and adaptability. We also benchmark its performance against baselines, demonstrating gains of up to 88%.

Notation: Boldface capital letters \mathbf{A} and boldface lowercase letters \mathbf{a} denote matrices and vectors, respectively. The transpose, Hermitian transpose, and trace of \mathbf{A} are denoted by \mathbf{A}^T , \mathbf{A}^H , and $\text{Tr}(\mathbf{A})$, respectively. Also, $j \triangleq \sqrt{-1}$ is the imaginary unit, $\mathbb{E}\{\cdot\}$ denotes statistical expectation, and $\mathcal{CN}(v, \xi^2)$ represents the complex Gaussian distribution with mean v and variance ξ^2 . Symbols $|\cdot|$, $\|\cdot\|_2$, and $\|\cdot\|_F$ denote the absolute value, ℓ_2 -norm, and Frobenius norm, respectively. In addition, \wedge and \vee represent logical ‘AND’ and logical ‘OR’ operators, respectively. Vectorization, Kronecker product, and Hadamard product are represented by $\text{vec}(\cdot)$, \otimes , and \circ , respectively. Finally, a generic set is defined as $\mathcal{X} = \{\mathbf{X} \mid \text{Condition}(\mathbf{X})\}$, where $\text{Condition}(\mathbf{X})$ specifies the defining property of the set.

2 SYSTEM MODEL AND PROBLEM FORMULATION

2.1 Preliminaries

Consider an ISAC system where a base station (BS), equipped with N_{tx} transmit antennas and N_{rx} receive antennas, serves U single-antenna users and senses T targets. Users and targets are assumed to lie in the far field of the BS, i.e., at distances exceeding the Rayleigh distance. The BS operates in a full-duplex downlink mode, utilizing analog beamforming for both transmission and reception with perfectly calibrated arrays. The transmit antenna array emits signals that serve a dual purpose: (i) delivering data to users and (ii) acting as radar waveforms for target sensing. Meanwhile, the receive antenna array captures reflected signals from targets.

The analog transmit beamformer can steer signals across a predefined set of angular directions, with multiple configurable options for power levels and beamwidths at each direction. Similarly, the analog receive beamformer is selected from a discrete set of angular directions, power levels, and beamwidths. Since analog beamforming is limited to processing one signal at a time, the BS employs timeslot allocation to efficiently coordinate the communication and sensing demands of users and targets over a finite horizon of S timeslots. These timeslots may be exclusively allocated for communication, exclusively for sensing, or configured to support both functionalities simultaneously. Enabling a timeslot to support both functionalities implies that a user-target pair is jointly served within that timeslot. Additionally, measurements of CSI, AOD, RC, and RSI are available at the BS for RRM design, albeit impaired by unknown errors that introduce uncertainty.

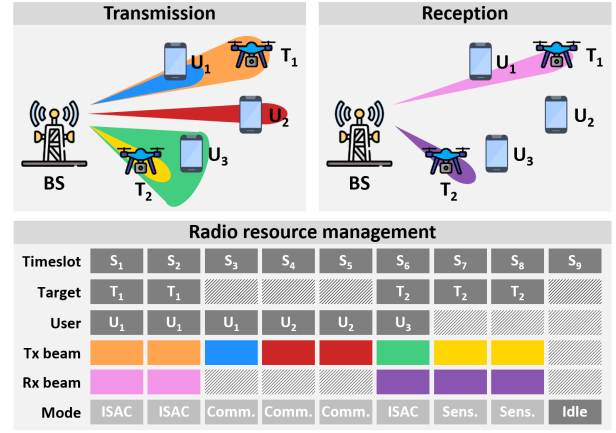


Fig. 1: System model comprising a BS, users, and targets.

The allocation of timeslots and beams, along with user-target pairing and timeslot functionality decisions, is driven by the goal of minimizing energy and time consumption while ensuring that the communication and sensing requirements are met. For simplicity, we denote the u -th user, t -th target, and s -th timeslot as U_u , T_t , and S_s , respectively. We define the sets of users, targets, and timeslots as $\mathcal{U} = \{1, \dots, U\}$, $\mathcal{T} = \{1, \dots, T\}$, and $\mathcal{S} = \{1, \dots, \tilde{S}\}$, respectively, where \tilde{S} is the maximal number of timeslots required by the BS for RRM. The system model is illustrated in Fig. 1, and all parameters and variables used in this work are summarized in **Table B.1** in **Appendix B**.

EXAMPLE. Fig. 1 illustrates 3 users (U_1, U_2, U_3) and 2 targets (T_1, T_2), which must be serviced over 9 timeslots (S_1 to S_9), aiming to minimize time and energy consumption. In $S_1 - S_2$, U_1 and T_1 are paired and jointly serviced by the orange beam, leveraging their angular alignment. During $S_1 - S_2$, the pink beam enables sensing of T_1 . In S_3 , U_1 is served alone by the blue beam, as T_1 's requirements have been fully met in $S_1 - S_2$, while U_1 requires an additional timeslot. Although the orange beam could have been maintained in S_3 , switching to the lower-power blue beam minimizes energy consumption. No receive beam is used in S_3 since no target is sensed. In $S_4 - S_5$, U_2 is served alone by the red beam. In S_6 , T_2 and U_3 are simultaneously served by the broad green beam, reducing time usage. In $S_7 - S_8$, T_2 is served alone by the narrower yellow beam. This shift occurs because U_3 's requirements are met in S_6 , while T_2 still requires additional sensing time. Continuing to serve T_2 with the green beam beyond S_6 would be energy-inefficient. Thus, the narrower yellow beam is selected as a more efficient alternative. Throughout $S_6 - S_8$, the purple beam enables sensing of T_2 . Finally, S_9 remains idle, ensuring no unnecessary resource expenditure.

2.2 Functionality selection

To determine which functionalities take place in each timeslot, we introduce constraints

$$C_1 : \kappa_s = \{0, 1\}, \forall s \in \mathcal{S},$$

$$C_2 : \zeta_s = \{0, 1\}, \forall s \in \mathcal{S},$$

where $\kappa_s = 1$ indicates that S_s is used for communication, and $\kappa_s = 0$ otherwise. Similarly, $\zeta_s = 1$ indicates that S_s is used for sensing, and $\zeta_s = 0$ otherwise. In particular, any

timeslot can support both functionalities simultaneously when feasible.

To determine whether a given timeslot is active, meaning it is in use, we introduce constraint

$$C_3 : \gamma_s = \kappa_s \vee \zeta_s, \forall s \in \mathcal{S}.$$

Here, $\gamma_s = 1$ indicates that S_s is active, while $\gamma_s = 0$ indicates that S_s is idle. The former case occurs when sensing, communication, or both take place in S_s , and the latter case occurs when neither functionality is implemented in S_s . Additionally, we include constraint

$$C_4 : \sum_{s \in \mathcal{S}} \gamma_s \leq S,$$

to ensure that the RRM design is confined within a finite horizon of S timeslots. In practice, we choose $S \ll \tilde{S}$ because a smaller value of S promotes the pairing of users and targets so that they can share timeslots, which is key to realizing the benefits of ISAC. Additional details on parameters S and \tilde{S} are provided in **Appendix C**.

2.3 Timeslot allocation and user-target pairing

To allocate timeslots to users, we introduce constraint

$$C_5 : \mu_{u,s} \in \{0, 1\}, \forall u \in \mathcal{U}, s \in \mathcal{S},$$

where $\mu_{u,s} = 1$ indicates that U_u is served in S_s , and $\mu_{u,s} = 0$ otherwise. We also include constraint

$$C_6 : \kappa_s = \sum_{u \in \mathcal{U}} \mu_{u,s}, \forall s \in \mathcal{S},$$

to ensure that each timeslot serves at most one user. This is guaranteed because κ_s is binary, meaning that at most one of the variables $\mu_{u,s}$ can equal one. This restriction arises from the use of analog beamforming at the BS, which confines signal processing to a single stream within any given timeslot.

To allocate timeslots to targets, we introduce constraint

$$C_7 : \tau_{t,s} \in \{0, 1\}, \forall t \in \mathcal{T}, s \in \mathcal{S},$$

where $\tau_{t,s} = 1$ indicates that T_t is served in S_s , and $\tau_{t,s} = 0$ otherwise. Furthermore, we add constraint

$$C_8 : \zeta_s = \sum_{t \in \mathcal{T}} \tau_{t,s}, \forall s \in \mathcal{S},$$

to restrict each timeslot to serve no more than one target. This is guaranteed because ζ_s is binary, ensuring that at most one of the variables $\tau_{t,s}$ can equal one.

User-target pairing determines which users and targets are jointly served within a given timeslot. This departs from existing approaches that rely on fixed associations or consider pairing for a single channel use, without exploiting the time dimension. In our framework, pairing is enabled only when it is feasible and leads to reduced time and energy consumption. Pairing is particularly beneficial when a user and a target are closely aligned in the angular domain, allowing them to be served simultaneously through a shared beam. However, angular similarity alone is not sufficient, as all system factors also influence the pairing decision. Therefore, treating user-target pairing as an optimizable variable is essential for achieving adaptive and resource-efficient RRM. In our framework, user-target pairing is enforced through constraints C_1, C_2, C_5, C_6, C_7 , and C_8 , which collectively ensure a one-to-one pairing between users and targets whenever feasible. Complementary details on this aspect are provided in **Appendix D**.

2.4 Beam adaptation

To achieve highly flexible beamforming and accommodate diverse sensing and communication requirements, the BS can adjust the direction, power, and beamwidth of its transmit and receive beampatterns. For practical implementation, these adaptations are restricted to a finite set of feasible configurations. To achieve this effectively, we adopt a column generation approach [47] and construct a predefined codebook, where each codeword corresponds to a unique combination of direction, power, and beamwidth. In each active timeslot, the BS selects one codeword for transmission, and another for reception when sensing is enabled.

Consider D_{tx} different angular directions $\tilde{\theta}_i, i \in \{1, \dots, D_{\text{tx}}\}$, in which the transmit signal can be steered. For each $\tilde{\theta}_i$, assume B_{tx} different beamwidths, leading to normalized codewords $\tilde{\mathbf{b}}_{i,j}$, such that $\|\tilde{\mathbf{b}}_{i,j}\|_2 = 1$, where $j \in \{1, \dots, B_{\text{tx}}\}$. Additionally, for each codeword $\tilde{\mathbf{b}}_{i,j}$, up to P_{tx} different powers can be applied, resulting in codewords $\hat{\mathbf{b}}_{i,j,k}$ where $k \in \{1, \dots, P_{\text{tx}}\}$. The complete set of codewords $\hat{\mathbf{b}}_{i,j,k}$ results in $L_{\text{tx}} = D_{\text{tx}} B_{\text{tx}} P_{\text{tx}}$ distinct transmit beampatterns. To facilitate a column-generation formulation, we replace the nested indices i, j , and k with a single subindex $b \in \mathcal{L}_{\text{tx}}$, where $\mathcal{L}_{\text{tx}} = \{1, \dots, L_{\text{tx}}\}$. The effective transmit codewords are thus denoted as $\mathbf{b}_b \in \mathbb{C}^{N_{\text{tx}} \times 1}$, with $\mathbf{b}_b \in \{\hat{\mathbf{b}}_{1,1,1}, \hat{\mathbf{b}}_{1,1,2}, \dots, \hat{\mathbf{b}}_{D_{\text{tx}}, B_{\text{tx}}, P_{\text{tx}}}\}$. Similarly, on the receive side, we consider D_{rx} directions, B_{rx} beamwidths, and P_{rx} power levels, resulting in $L_{\text{rx}} = D_{\text{rx}} B_{\text{rx}} P_{\text{rx}}$ distinct receive beampatterns. These are indexed by $c \in \mathcal{L}_{\text{rx}}$, with $\mathcal{L}_{\text{rx}} = \{1, \dots, L_{\text{rx}}\}$, and the corresponding effective receive codewords are denoted as $\mathbf{c}_c \in \mathbb{C}^{N_{\text{rx}} \times 1}$, where $\mathbf{c}_c \in \{\hat{\mathbf{c}}_{1,1,1}, \hat{\mathbf{c}}_{1,1,2}, \dots, \hat{\mathbf{c}}_{D_{\text{rx}}, B_{\text{rx}}, P_{\text{rx}}}\}$.

To enable transmit beamforming, we introduce

$$C_9 : \chi_{b,s} \in \{0, 1\}, \forall b \in \mathcal{L}_{\text{tx}}, s \in \mathcal{S},$$

where $\chi_{b,s} = 1$ indicates that codeword \mathbf{b}_b is used in S_s , and $\chi_{b,s} = 0$ otherwise. Furthermore, we introduce constraint

$$C_{10} : \sum_{b \in \mathcal{L}_{\text{tx}}} \chi_{b,s} = \gamma_s, \forall s \in \mathcal{S},$$

to ensure that transmit codewords are selected solely for timeslots that are active, as indicated by γ_s . Specifically, no codeword is selected for idle timeslots. Thus, the transmit beamformer employed in S_s is defined by constraint

$$C_{11} : \mathbf{w}_s = \sum_{b \in \mathcal{L}_{\text{tx}}} \mathbf{b}_b \cdot \chi_{b,s}, \forall s \in \mathcal{S}.$$

To enable receive beamforming, we introduce

$$C_{12} : \rho_{c,s} \in \{0, 1\}, \forall c \in \mathcal{L}_{\text{rx}}, s \in \mathcal{S},$$

where $\rho_{c,s} = 1$ indicates that codeword \mathbf{c}_c is used in S_s , and $\rho_{c,s} = 0$ otherwise. Additionally, we include constraint

$$C_{13} : \sum_{c \in \mathcal{L}_{\text{rx}}} \rho_{c,s} = \zeta_s, \forall s \in \mathcal{S},$$

to ensure that receive codewords are selected only for timeslots performing sensing, as indicated by ζ_s . The receive beamformer used in S_s is given by constraint

$$C_{14} : \mathbf{v}_s = \sum_{c \in \mathcal{L}_{\text{rx}}} \mathbf{c}_c \cdot \rho_{c,s}, \forall s \in \mathcal{S}.$$

2.5 Communication metric

Let $d_s \in \mathbb{C}$ denote the symbol transmitted by the BS in timeslot S_s . This symbol may be used for communication,

sensing, or both functionalities simultaneously. The transmitted symbol follows a complex Gaussian distribution with zero mean and unit variance, i.e., $\mathbb{E}\{d_s d_s^*\} = 1$.

Although calibrated antenna arrays are assumed, impairments such as mutual coupling among neighboring antennas may still be present. Mutual coupling alters the beam pattern shape by modifying the effective beamforming vectors applied at the antenna ports. Accordingly, when a nominal transmit codeword \mathbf{w}_s is selected in timeslot S_s , the effective beamformed transmit signal is given by

$$\mathbf{x}_s = \mathbf{Z}_{\text{tx}} \mathbf{w}_s d_s, \quad (1)$$

where $\mathbf{Z}_{\text{tx}} \in \mathbb{C}^{N_{\text{tx}} \times N_{\text{tx}}}$ denotes the transmit-side mutual coupling matrix, defined with banded Toeplitz structure,

$$\mathbf{Z}_{\text{tx}} = \begin{bmatrix} 1 & \delta_{\text{tx}} & 0 & 0 & \cdots & 0 & 0 \\ \delta_{\text{tx}} & 1 & \delta_{\text{tx}} & 0 & \cdots & 0 & 0 \\ 0 & \delta_{\text{tx}} & 1 & \delta_{\text{tx}} & \cdots & 0 & 0 \\ \vdots & \vdots & \vdots & \vdots & \ddots & \vdots & \vdots \\ 0 & 0 & 0 & 0 & \cdots & 1 & \delta_{\text{tx}} \\ 0 & 0 & 0 & 0 & \cdots & \delta_{\text{tx}} & 1 \end{bmatrix}, \quad (2)$$

where $|\delta_{\text{tx}}| \ll 1$ represents the coupling strength between adjacent antenna elements [48], [49].

The signal received by U_u in S_s is therefore expressed as

$$\begin{aligned} y_{\text{com}}^{u,s} &= \mathbf{h}_u^H \mathbf{x}_s \cdot \mu_{u,s} + n_{\text{com},u}, \\ &= \mathbf{h}_u^H \mathbf{Z}_{\text{tx}} \mathbf{w}_s d_s \cdot \mu_{u,s} + n_{\text{com},u}, \end{aligned} \quad (3)$$

where $\mathbf{h}_u \in \mathbb{C}^{N_{\text{tx}} \times 1}$ is the communication channel between the BS and U_u , while $n_{\text{com},u} \sim \mathcal{CN}(0, \sigma_{\text{com}}^2)$ represents additive white Gaussian noise (AWGN). The communication signal-to-noise ratio (SNR) for U_u in S_s is defined as

$$\text{SNR}_{\text{com}}^{u,s} = \frac{|\mathbf{h}_u^H \mathbf{Z}_{\text{tx}} \mathbf{w}_s \cdot \mu_{u,s}|^2}{\sigma_{\text{com}}^2}. \quad (4)$$

In practice, BSs operate with imperfect CSI due to factors such as quantization and feedback delay, which introduce errors. These errors can significantly affect communication performance, making it essential to incorporate them into the RRM design. Imperfect CSI is modeled via constraint

$$C_{15} : \mathcal{H}_u \triangleq \left\{ \mathbf{h}_u \mid \mathbf{h}_u = \bar{\mathbf{h}}_u + \Delta \mathbf{h}_u, \|\Delta \mathbf{h}_u\|_2^2 \leq \epsilon_{\text{CSI}}^2 \right\}, \forall u \in \mathcal{U},$$

using the model from [50], [51], where \mathbf{h}_u is the actual but unknown channel, $\bar{\mathbf{h}}_u$ is the estimated channel, $\Delta \mathbf{h}_u$ is the random channel error whose power is bounded by ϵ_{CSI}^2 , and \mathcal{H}_u represents the uncertainty set of all possible channel vectors for U_u .

To ensure reliable communication performance, we introduce constraint

$$C_{16} : \min_{\mathbf{h}_u \in \mathcal{H}_u} \text{SNR}_{\text{com}}^{u,s} \geq \Upsilon_{\text{snr},u} \cdot \mu_{u,s}, \forall u \in \mathcal{U}, s \in \mathcal{S},$$

which guarantees a predefined SNR $\Upsilon_{\text{snr},u}$ for each user U_u across its allocated timeslots, while accounting for imperfect CSI. Additionally, we include constraint

$$C_{17} : \sum_{s \in \mathcal{S}} \mu_{u,s} = S_{\text{com},u}, \forall u \in \mathcal{U},$$

to ensure that each U_u is allocated exactly $S_{\text{com},u}$ timeslots.

2.6 Sensing metric

Targets are assumed to lie in the far field of the BS and are modeled as single point scatterers. The BS operates in a monostatic configuration, implying identical AOD and angle of

arrival (AOA). Although the far-field assumption removes any explicit dependence of the AOD on the physical extent of the target, practical AOD estimates remain affected by estimation errors, discrete-time tracking effects, and target micro-motion. To capture these imperfections, we adopt the modeling approach in [52], [53] and introduce constraint

$$C_{18} : \Theta_t \triangleq \left\{ \theta_t \mid \theta_t = \bar{\theta}_t + \Delta \theta_t, |\Delta \theta_t|^2 \leq \epsilon_{\text{AOD}}^2 \right\}, \forall t \in \mathcal{T},$$

where θ_t is the actual but unknown AOD, $\bar{\theta}_t$ is the estimated AOD, $\Delta \theta_t$ is the random AOD error whose power is bounded by ϵ_{AOD}^2 , and Θ_t represents the uncertainty set of all possible AODs for T_t .

Another important factor is the RC, which captures both the target's radar cross-section and the round-trip path-loss relative to the BS [54]. However, due to quantization errors and interference from clutter, the RC is typically not perfectly known. To account for potential errors in this parameter, we adopt the model from [36] and introduce

$$C_{19} : \Psi_t \triangleq \left\{ \psi_t \mid \psi_t = \bar{\psi}_t + \Delta \psi_t, |\Delta \psi_t|^2 \leq \epsilon_{\text{RC}}^2 \right\}, \forall t \in \mathcal{T},$$

where ψ_t is the actual but unknown RC, $\bar{\psi}_t$ is the estimated RC, $\Delta \psi_t$ is the random RC error whose power is bounded by ϵ_{RC}^2 , and Ψ_t represents the uncertainty set of all possible RCs for T_t .

REMARK 1. The nominal RC $\bar{\psi}_t$ corresponds to the estimated AOD $\bar{\theta}_t$. In practice, the actual RC varies with the aspect angle. This effect is captured through the bounded uncertainty term $\Delta \psi_t$ in C_{19} , where parameter ϵ_{RC} encompasses both measurement errors and aspect-angle RC fluctuations, thereby including even the worst-case deviation within the angular uncertainty set Θ_t .

Considering the AOD and RC, the sensing channel between the BS and T_t is defined as

$$\mathbf{G}_t = \psi_t \cdot \mathbf{a}_{\text{rx}}(\theta_t) \mathbf{a}_{\text{tx}}^H(\theta_t) = \psi_t \cdot \mathbf{A}(\theta_t), \quad (5)$$

where the transmit and receive steering vectors are given by

$$\mathbf{a}_l(\theta_t) = \frac{1}{\sqrt{N_l}} e^{j\phi_l \cos(\theta_t)}, \quad (6)$$

with $l = \{\text{tx}, \text{rx}\}$. Besides, vector ϕ_l is defined as

$$\phi_l = \frac{2\pi d_l}{\lambda} \left[\frac{-N_l+1}{2}, \dots, \frac{N_l-1}{2} \right]^T, \quad (7)$$

where λ represents the wavelength and d_l denotes the antenna spacings of the transmit/receive array.

REMARK 2. An extended target can be modeled as a set of M scattering centers, with the sensing channel expressed as $\mathbf{G}_t = \sum_{m \in \mathcal{M}} \psi_{t,m} \cdot \mathbf{A}(\theta_{t,m})$, where $\theta_{t,m}$ and $\psi_{t,m}$ denote the AOD and RC of the m -th scattering center, respectively, for $m \in \mathcal{M} = \{1, \dots, M\}$. In this work, we focus on the special case of a single effective scattering center, i.e., $M = 1$. Notably, the proposed framework and solution can be directly extended to an arbitrary number of resolved scattering centers ($M > 1$), where the sensing SINR follows from incoherent power summation across all centers.

Note that matrix \mathbf{G}_t is linear with respect to ψ_t but nonlinear with respect to θ_t . The nonlinearity in θ_t complicates the model's tractability for further optimization. To address it, we adopt the linear model employed in [52], [53], originally designed for transmit and receive steering vectors of equal length. We extend this model to accommodate transmit and receive arrays of different lengths, resulting

in a more general construct. Since $\mathbf{A}(\theta_t)$ is the component of \mathbf{G}_t that encapsulates the nonlinear dependence on θ_t , we adopt a linearized approximation of $\mathbf{A}(\theta_t)$, given by

$$\mathbf{A}(\theta_t) \approx \mathbf{A}(\bar{\theta}_t) + \tilde{\mathbf{A}}(\bar{\theta}_t) \Delta\theta_t, \quad (8)$$

where $\mathbf{A}(\bar{\theta}_t) = \frac{1}{\sqrt{N_{\text{rx}}N_{\text{tx}}}} e^{j\Phi \cos(\bar{\theta}_t)}$, $\Phi = \mathbf{1}^T \otimes \phi_{\text{rx}} - \mathbf{1} \otimes \phi_{\text{tx}}^T$, $\tilde{\mathbf{A}}(\bar{\theta}_t) = \mathbf{A}(\bar{\theta}_t) \circ \mathbf{E}(\bar{\theta}_t)$, $\mathbf{E}(\bar{\theta}_t) = -j\Phi \sin(\bar{\theta}_t)$. The derivation of this model is detailed in **Appendix E**.

In full-duplex systems, the transmit and receive arrays at the BS are typically placed in close proximity, which causes the receive array to capture strong leakage from the transmit array. As a result, in addition to the echoes reflected from the target of interest and environmental clutter, the received signal contains a self-interference component arising from direct coupling between the transmit and receive arrays.

Before processing the target reflections, the BS applies standard monostatic radar clutter-filtering techniques [55]–[57]. Static clutter (e.g., buildings) is typically removed using Doppler windowing or high-pass filters, while dynamic clutter (e.g., moving objects) is mitigated through subspace projection or low-rank filtering. These operations primarily suppress external environmental reflections and are assumed not to significantly distort the deterministic self-interference component. After clutter suppression, the signal received at the BS from target T_t during S_s is

$$\begin{aligned} y_{\text{sen}}^{t,s} &= \mathbf{v}_s^H \mathbf{Z}_{\text{rx}}^H (\mathbf{G}_t + \tilde{\mathbf{I}}) \mathbf{x}_s \cdot \tau_{t,s} + \mathbf{v}_s^H \mathbf{Z}_{\text{rx}}^H \mathbf{n}_{\text{sen},t}, \\ &= \underbrace{\mathbf{v}_s^H \mathbf{Z}_{\text{rx}}^H \mathbf{G}_t \mathbf{Z}_{\text{tx}} \mathbf{w}_s d_s \cdot \tau_{t,s}}_{\text{desired signal}} + \underbrace{\mathbf{v}_s^H \mathbf{Z}_{\text{rx}}^H \tilde{\mathbf{I}} \mathbf{Z}_{\text{tx}} \mathbf{w}_s d_s \cdot \tau_{t,s}}_{\text{self-interference}} \\ &\quad + \underbrace{\mathbf{v}_s^H \mathbf{Z}_{\text{rx}}^H \mathbf{n}_{\text{sen},t}}_{\text{noise}}, \end{aligned} \quad (9)$$

where $\tilde{\mathbf{I}}$ denotes the direct self-interference channel between the transmit and receive arrays, and $\mathbf{n}_{\text{sen},t} \sim \mathcal{CN}(\mathbf{0}, \sigma_{\text{sen}}^2 \mathbf{I})$ models thermal noise and any residual clutter remaining after suppression [55], [56]. Receive-side mutual coupling is modeled via the matrix $\mathbf{Z}_{\text{rx}} \in \mathbb{C}^{N_{\text{rx}} \times N_{\text{rx}}}$, parameterized by coupling strength δ_{rx} , similarly to (2).

Afterwards, the BS employs analog and/or digital signal processing techniques to mitigate self-interference [58]. These techniques operate on the already clutter-filtered signal and rely on estimates of the self-interference channel. Due to hardware imperfections and channel estimation errors, cancellation is inherently imperfect and results in RSI. Specifically, the BS performs self-interference cancellation by subtracting $\mathbf{v}_s^H \mathbf{Z}_{\text{rx}}^H \tilde{\mathbf{I}} \mathbf{Z}_{\text{tx}} \mathbf{w}_s d_s \cdot \tau_{t,s}$ from $y_{\text{sen}}^{t,s}$, where $\tilde{\mathbf{I}}$ is an estimate of $\tilde{\mathbf{I}}$. The post-cancellation signal is expressed as

$$\begin{aligned} \bar{y}_{\text{sen}}^{t,s} &= y_{\text{sen}}^{t,s} - \mathbf{v}_s^H \mathbf{Z}_{\text{rx}}^H \tilde{\mathbf{I}} \mathbf{Z}_{\text{tx}} \mathbf{w}_s d_s \cdot \tau_{t,s} \\ &= \mathbf{v}_s^H \mathbf{Z}_{\text{rx}}^H \mathbf{G}_t \mathbf{Z}_{\text{tx}} \mathbf{w}_s d_s \cdot \tau_{t,s} \\ &\quad + \mathbf{v}_s^H \mathbf{Z}_{\text{rx}}^H \mathbf{R} \mathbf{Z}_{\text{tx}} \mathbf{w}_s d_s \cdot \tau_{t,s} + \mathbf{v}_s^H \mathbf{Z}_{\text{rx}}^H \mathbf{n}_{\text{sen},t}, \end{aligned} \quad (10)$$

where $\mathbf{R} = \tilde{\mathbf{I}} - \tilde{\mathbf{I}}$ is the RSI channel and $\mathbf{v}_s^H \mathbf{Z}_{\text{rx}}^H \mathbf{R} \mathbf{Z}_{\text{tx}} \mathbf{w}_s d_s \cdot \tau_{t,s}$ represents the interfering signal. The primary challenge in achieving complete interference cancellation lies in the imperfect knowledge of \mathbf{R} . Following the models in [59], [60], the RSI channel is characterized by constraint

$$\mathcal{C}_{20} : \mathcal{R} \triangleq \left\{ \mathbf{R} \mid \mathbf{R} = v\bar{\mathbf{R}} + v\Delta\mathbf{R}, \|\Delta\mathbf{R}\|_{\text{F}}^2 \leq \epsilon_{\text{RSI}}^2 \right\},$$

where \mathcal{R} is the uncertainty set encompassing all RSI pos-

sibilities. Here, \mathbf{R} consists of a deterministic and a random component, denoted by $\bar{\mathbf{R}}$ and $\Delta\mathbf{R}$, respectively. The deterministic component depends on the relative geometry between arrays, and is defined as

$$[\bar{\mathbf{R}}]_{\bar{m},\bar{n}} = \frac{\lambda}{4\pi d_{\bar{m},\bar{n}}} \frac{1}{\sqrt{N_{\text{rx}}N_{\text{tx}}}} e^{-j\frac{2\pi}{\lambda} d_{\bar{m},\bar{n}}}. \quad (11)$$

Specifically, $d_{\bar{m},\bar{n}}$ denotes the distance between the \bar{m} -th receive antenna and the \bar{n} -th transmit antenna [61], [62], with the centers of the antenna arrays separated by a distance \bar{d}_c . Meanwhile, the random component accounts for spurious self-interference whose power is bounded by ϵ_{RSI}^2 . Parameter v quantifies the severity of self-interference in the processed signal. Thus, $v = 0$ indicates perfect self-interference cancellation, while $v = 1$ signifies the absence of any cancellation.

REMARK 3. *The norm-bounded uncertainty set that models RSI is designed to capture the aggregate residual self-interference after analog/digital cancellation. This modeling approach accounts not only for linear estimation errors but also for distortions arising from nonlinear RF impairments, such as power amplifier saturation and IQ imbalance. These nonlinear effects are implicitly captured through the parameter ϵ_{RSI} , which upper-bounds the total residual interference energy after cancellation.*

From (10), the sensing signal-to-interference-plus-noise ratio (SINR) for target T_t in S_s is defined as

$$\text{SINR}_{\text{sen}}^{t,s} = \frac{|\mathbf{v}_s^H \mathbf{Z}_{\text{rx}}^H \mathbf{G}_t \mathbf{Z}_{\text{tx}} \mathbf{w}_s \cdot \tau_{t,s}|^2}{|\mathbf{v}_s^H \mathbf{Z}_{\text{rx}}^H \mathbf{R} \mathbf{Z}_{\text{tx}} \mathbf{w}_s \cdot \tau_{t,s}|^2 + \sigma_{\text{sen}}^2 \|\mathbf{Z}_{\text{rx}} \mathbf{v}_s\|_2^2}. \quad (12)$$

Additionally, we include constraint

$$\mathcal{C}_{21} : \min_{\psi_t \in \Psi_t} \min_{\theta_t \in \Theta_t} \min_{\mathbf{R} \in \mathcal{R}} \text{SINR}_{\text{sen}}^{t,s} \geq \Lambda_{\text{sinr},t} \cdot \tau_{t,s}, \forall t \in \mathcal{T},$$

which ensures that the sensing SINR in every allocated timeslot for each target remains above a predefined threshold $\Lambda_{\text{sinr},t}$, even under uncertainties in the RC, AOA, and RSI. Furthermore, each target is allocated $S_{\text{sen},t}$ timeslots, which dictates the dwell time and is enforced through

$$\mathcal{C}_{22} : \sum_{s \in \mathcal{S}} \tau_{t,s} = S_{\text{sen},t}, \forall t \in \mathcal{T}.$$

REMARK 4. *Sufficient cumulative SINR for accurate Doppler estimation can be achieved by jointly tuning the dwell time $S_{\text{sen},t}$ and the sensing SINR threshold $\Lambda_{\text{sinr},t}$. These parameters can be traded off to meet a required Doppler resolution, with longer dwell times compensating for lower SINR thresholds and vice versa.*

2.7 Objective function

We define the multi-objective function

$$\mathbf{f}(\boldsymbol{\Omega}) \triangleq \begin{bmatrix} f_1(\boldsymbol{\Omega}) \\ f_2(\boldsymbol{\Omega}) \end{bmatrix}, \quad (13)$$

where $\boldsymbol{\Omega}$ represents the set of all decision variables. Functions $f_1(\boldsymbol{\Omega})$ and $f_2(\boldsymbol{\Omega})$ are defined as follows

$$\begin{aligned} f_1(\boldsymbol{\Omega}) &\triangleq S_{\text{dur}} \sum_{s \in \mathcal{S}} \|\mathbf{w}_s\|_2^2 + S_{\text{dur}} \sum_{s \in \mathcal{S}} \|\mathbf{v}_s\|_2^2, \\ f_2(\boldsymbol{\Omega}) &\triangleq S_{\text{dur}} \sum_{s \in \mathcal{S}} \omega_s \cdot \gamma_s. \end{aligned}$$

Function $f_1(\boldsymbol{\Omega})$ represents the total energy consumption of the BS for both transmit and receive beamforming over all allocated timeslots, where S_{dur} denotes the duration of each timeslot. In particular, minimizing this function helps reduce the carbon footprint while also limiting interference to neighboring networks.

Function $f_2(\Omega)$ represents the total consumption of time resources, modeled as a weighted sum of timeslots. Minimizing $f_2(\Omega)$ helps reduce the number of active timeslots, fostering timeslot reuse by pairing users and targets. Here, weights ω_s are carefully chosen to mitigate sparsity in timeslot utilization, promoting a more cohesive allocation that eliminates idle timeslots between active ones. This ensures contiguous timeslot usage, allowing subsequent allocations to start earlier. In particular, **Lemma 1** presents a family of weights designed to enhance reuse and compactness in timeslot allocation.

Lemma 1. *A set of weights that promotes compact timeslot allocation in $f_2(\Omega)$ is given by $\omega_s = \Delta_0 + (s-1) \cdot \Delta_\omega, \forall s \in \mathcal{S}$, where $\Delta_\omega > 0$.*

Proof. Please, refer to **Appendix F**. ■

Minimizing energy consumption alone is insufficient, as it does not account for the duration over which the energy is expended. Conversely, minimizing consumption of time resources alone overlooks the amount of power used. Hence, jointly considering both aspects is essential to achieve true resource economy and high efficiency.

2.8 Problem formulation

We formulate the RRM design as

$$\mathcal{P}(\Omega) : \underset{\Omega}{\text{minimize}} \quad \mathbf{f}(\Omega) \quad \text{s.t.} \quad C_1 - C_{22}.$$

Problem $\mathcal{P}(\Omega)$ is challenging to solve due to the presence of couplings between variables and the semi-infinite number of constraints arising from imperfect knowledge of CSI, RC, AOD, and RSI. Specifically, $\mathcal{P}(\Omega)$ is a nonconvex MINLP, for which no generic solution methods exist.

3 PROPOSED OPTIMAL APPROACH

This section presents an equivalent transformation of problem $\mathcal{P}(\Omega)$ that preserves optimality. The complicating terms within $\mathcal{P}(\Omega)$ are reformulated into more tractable expressions, revealing that the problem is convex, specifically, a MISDP that can be solved to global optimality. For clarity, Fig. 2 outlines the steps involved in simplifying the challenging expressions. This process results in a transformed problem $\mathcal{P}'(\Omega')$, where Ω' denotes the updated set of decision variables.

In the following, we delve into each of the steps that facilitate this transformation.

3.1 Addressing the logical couplings induced by C_3

We introduce **Proposition 1** to cope with the logical operator \vee appearing in constraint C_3 , which links variables κ_s and ζ_s . We decouple the binary variables and reformulate C_3 into an equivalent set of linear inequalities.

Proposition 1. *Constraint C_3 can be equivalently rewritten as constraints D_1, D_2, D_3 , and D_4 , shown below*

$$C_3 \Leftrightarrow \begin{cases} D_1 : \gamma_s \leq \kappa_s + \zeta_s, \forall s \in \mathcal{S}, \\ D_2 : \gamma_s \geq \kappa_s, \forall s \in \mathcal{S}, \\ D_3 : \gamma_s \geq \zeta_s, \forall s \in \mathcal{S}, \\ D_4 : \gamma_s \leq 1, \forall s \in \mathcal{S}. \end{cases}$$

Proof. For the detailed derivation, refer to **Appendix G**. ■

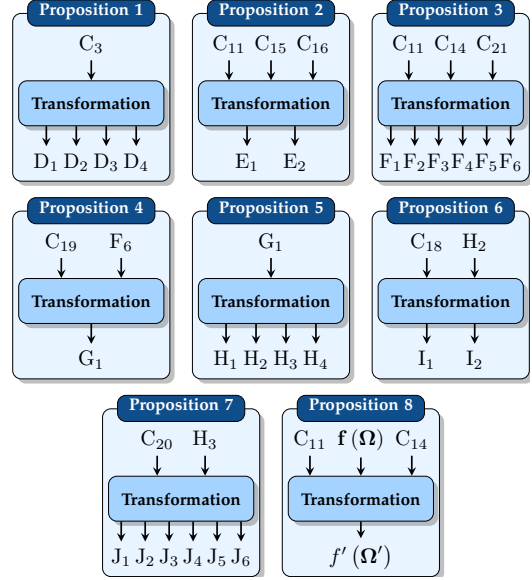


Fig. 2: Diagram illustrating the proposed approach.

3.2 Addressing the couplings between variables and the infinite constraints in C_{11}, C_{15} , and C_{16}

We introduce **Proposition 2** to address the challenges posed by C_{11}, C_{15} , and C_{16} , stemming from variable coupling and the infinite constraint set due to imperfect CSI. Specifically, we decouple variables \mathbf{w}_s and $\mu_{u,s}$ in C_{16} , by analyzing the expressions in which the coupling appears and deriving equivalent reformulations that preserve the original solution space. This step is critical to our approach, as it allows us to restructure the expressions in a way that eliminates couplings without introducing additional variables. Furthermore, to manage the infinite constraint set induced by C_{15} , we employ the *S-Procedure*, outlined in **Lemma 2**, which transforms an infinite constraint set into a finite and computationally tractable form. The overall procedure reformulates C_{11}, C_{15} , and C_{16} into an equivalent set of linear inequalities, while ensuring that the solution space of these constraints remains unchanged.

Proposition 2. *Constraints C_{11}, C_{15} , and C_{16} can be equivalently rewritten as constraints E_1 and E_2 , shown below,*

$$C_{11}, C_{15}, C_{16} = \begin{cases} E_1 : \begin{bmatrix} \mathbf{E}_{u,s}^a & \mathbf{e}_{u,s}^b \\ \mathbf{e}_{u,s}^c & e_{u,s}^d \end{bmatrix} \succcurlyeq \mathbf{0}, \forall u \in \mathcal{U}, s \in \mathcal{S}, \\ E_2 : \alpha_u \geq 0, \forall u \in \mathcal{U}, \end{cases}$$

where $\mathbf{E}_{u,s}^a = \alpha_u \mathbf{I} - \mathbf{L}_s$, $\mathbf{e}_{u,s}^b = -\mathbf{L}_s \bar{\mathbf{h}}_u$, $\mathbf{e}_{u,s}^c = -\bar{\mathbf{h}}_u^H \mathbf{L}_s$, $e_{u,s}^d = -\alpha_u \cdot \epsilon_{\text{CSI}}^2 - \bar{\mathbf{h}}_u^H \mathbf{L}_s \bar{\mathbf{h}}_u - \Upsilon_{\text{snr},u} \cdot \mu_{u,s}$, $\mathbf{L}_s = -\sum_{b \in \mathcal{L}_{\text{tx}}} \frac{1}{\sigma_{\text{com}}^2} \mathbf{Z}_{\text{tx}} \mathbf{b}_b \mathbf{b}_b^H \mathbf{Z}_{\text{tx}}^H \chi_{b,s}$, and α_u are newly introduced variables.

Proof. For the detailed derivation, refer to **Appendix H**. ■

Lemma 2 (S-Procedure). *Let $h_i(\mathbf{x}) \triangleq \mathbf{x}^H \mathbf{A}_i \mathbf{x} + \mathbf{b}_i^H \mathbf{x} + \mathbf{x}^H \mathbf{b}_i + c_i$, for $i = 1, 2$, be quadratic functions, where $\mathbf{A}_i \in \mathbb{C}^{N \times N}$ is Hermitian, $\mathbf{b}_i \in \mathbb{C}^{N \times 1}$, and $c_i \in \mathbb{R}$. Thus, the following two statements are equivalent:*

i) *If \mathbf{x} satisfies $h_1(\mathbf{x}) \leq 0$, then $h_2(\mathbf{x}) \leq 0$ also holds.*

ii) *There exists $\alpha \geq 0$ such that $\alpha \begin{bmatrix} \mathbf{A}_1 & \mathbf{b}_1 \\ \mathbf{b}_1^H & c_1 \end{bmatrix} - \begin{bmatrix} \mathbf{A}_2 & \mathbf{b}_2 \\ \mathbf{b}_2^H & c_2 \end{bmatrix} \succcurlyeq \mathbf{0}$, where α is a newly introduced variable.*

3.3 Addressing the couplings between variables in C_{11} , C_{14} , and C_{21}

We introduce **Proposition 3** to deal with the multiplicative coupling between variables \mathbf{w}_s , \mathbf{v}_s , and $\tau_{t,s}$, posed by C_{11} , C_{14} , and C_{21} . We reformulate these constraints into an equivalent set of equations and inequalities without altering the original solution space.

Proposition 3. *Constraints C_{11} , C_{14} , and C_{21} can be equivalently written as constraints F_1 , F_2 , F_3 , F_4 , F_5 , and F_6 (see bottom of this page), where $\ell_{t,s}(\Omega') \triangleq \min_{\mathbf{R} \in \mathcal{R}} \frac{|\sum_{c \in \mathcal{L}_{\text{rx}}} \sum_{b \in \mathcal{L}_{\text{tx}}} \mathbf{c}_c^H \mathbf{Z}_{\text{rx}}^H \mathbf{A}(\theta_t) \mathbf{Z}_{\text{tx}} \mathbf{b}_b \cdot \pi_{b,c,t,s}|^2}{|\sum_{c \in \mathcal{L}_{\text{rx}}} \sum_{b \in \mathcal{L}_{\text{tx}}} \mathbf{c}_c^H \mathbf{Z}_{\text{rx}}^H \mathbf{R} \mathbf{Z}_{\text{tx}} \mathbf{b}_b \cdot \pi_{b,c,t,s}|^2 + \sigma_{\text{sen}}^2 \sum_{c \in \mathcal{L}_{\text{rx}}} \|\mathbf{Z}_{\text{rx}} \mathbf{c}_c\|_{2\rho_{c,s}}^2}$ and $\pi_{b,c,t,s}$ are newly introduced variables.*

Proof. For the detailed derivation, refer to **Appendix I**. ■

3.4 Addressing the infinite constraints in C_{19} and F_6

We present **Proposition 4** to address the infinite constraint set arising from imperfect RC, which affects C_{19} and F_6 . Specifically, we rearrange these constraints to disentangle the effects of imperfect RC from those caused by imperfect RSI and AOD. After isolating the effect of imperfect RC, we observe that it effectively scales and magnifies the nominal SINR threshold, leading to a more demanding sensing performance requirement. Notably, the scaled SINR threshold admits a closed-form expression, facilitating further analysis and optimization. Overall, this transformation converts the infinite constraint set induced by imperfect RC into a more tractable form, leading to an equivalent set of inequalities.

Proposition 4. *Constraints C_{19} and F_6 can be equivalently rewritten as constraints G_1 , shown below,*

$$C_{19}, F_6 \Leftrightarrow G_1 : \min_{\theta_t \in \Theta_t} \ell_{t,s}(\Omega') \geq \bar{\Lambda}_{\text{sinr},t} \cdot \tau_{t,s}, \forall t \in \mathcal{T}, s \in \mathcal{S},$$

$$\text{where } \bar{\Lambda}_{\text{sinr},t} = \frac{\Lambda_{\text{sinr},t}}{(|\bar{\psi}_t| - \epsilon_{\text{RC}})^2} \text{ and } \ell_{t,s}(\Omega') \triangleq \min_{\mathbf{R} \in \mathcal{R}} \frac{|\sum_{c \in \mathcal{L}_{\text{rx}}} \sum_{b \in \mathcal{L}_{\text{tx}}} \mathbf{c}_c^H \mathbf{Z}_{\text{rx}}^H \mathbf{A}(\theta_t) \mathbf{Z}_{\text{tx}} \mathbf{b}_b \cdot \pi_{b,c,t,s}|^2}{|\sum_{c \in \mathcal{L}_{\text{rx}}} \sum_{b \in \mathcal{L}_{\text{tx}}} \mathbf{c}_c^H \mathbf{Z}_{\text{rx}}^H \mathbf{R} \mathbf{Z}_{\text{tx}} \mathbf{b}_b \cdot \pi_{b,c,t,s}|^2 + \sigma_{\text{sen}}^2 \sum_{c \in \mathcal{L}_{\text{rx}}} \|\mathbf{Z}_{\text{rx}} \mathbf{c}_c\|_{2\rho_{c,s}}^2}.$$

Proof. For the detailed derivation, refer to **Appendix J**. ■

3.5 Addressing the rational nature of the SINR in G_1

We introduce **Proposition 5** to address the rational nature of G_1 . This is accomplished by introducing additional variables that separate the numerator and denominator of the SINRs, leading to an equivalent set of inequalities that preserve the original solution space of G_1 . Importantly, this transformation facilitates the decoupling of effects arising from imperfect AOD and imperfect RSI, allowing us to address them independently in subsequent steps.

Proposition 5. *Constraint G_1 can be equivalently rewritten as constraints H_1 , H_2 , H_3 , and H_4 , shown below,*

$$G_1 \Leftrightarrow \begin{cases} H_1 : z_{t,s} \geq 0, \forall t \in \mathcal{T}, s \in \mathcal{S}, \\ H_2 : \hat{\ell}_{t,s}(\Omega') \geq z_{t,s}, \forall t \in \mathcal{T}, s \in \mathcal{S}, \\ H_3 : \check{\ell}_{t,s}(\Omega') \leq z_{t,s}, \forall t \in \mathcal{T}, s \in \mathcal{S}, \\ H_4 : z_{t,s} \leq \tau_{t,s} \cdot \dot{M}_t^{\text{UB}}, \forall t \in \mathcal{T}, s \in \mathcal{S}, \end{cases}$$

where $\hat{\ell}_{t,s}(\Omega') \triangleq \frac{1}{\sigma_{\text{sen}}^2} \min_{\theta_t \in \Theta_t} |\sum_{c \in \mathcal{L}_{\text{rx}}} \sum_{b \in \mathcal{L}_{\text{tx}}} \mathbf{c}_c^H \mathbf{Z}_{\text{rx}}^H \mathbf{A}(\theta_t) \mathbf{Z}_{\text{tx}} \mathbf{b}_b \cdot \pi_{b,c,t,s}|^2$, $\check{\ell}_{t,s}(\Omega') \triangleq \frac{1}{\sigma_{\text{sen}}^2} \bar{\Lambda}_{\text{sinr},t} \cdot \tau_{t,s} \cdot \max_{\mathbf{R} \in \mathcal{R}} |\sum_{c \in \mathcal{L}_{\text{rx}}} \sum_{b \in \mathcal{L}_{\text{tx}}} \mathbf{c}_c^H \mathbf{Z}_{\text{rx}}^H \mathbf{R} \mathbf{Z}_{\text{tx}} \mathbf{b}_b \cdot \pi_{b,c,t,s}|^2 + \bar{\Lambda}_{\text{sinr},t} \cdot \tau_{t,s} \sum_{c \in \mathcal{L}_{\text{rx}}} \|\mathbf{Z}_{\text{rx}} \mathbf{c}_c\|_{2\rho_{c,s}}^2$, and $\dot{M}_t^{\text{UB}} = \max_{b \in \mathcal{L}_{\text{tx}}} \max_{c \in \mathcal{L}_{\text{rx}}} \frac{|\mathbf{c}_c^H \mathbf{Z}_{\text{rx}}^H \mathbf{A}(\theta_t) \mathbf{Z}_{\text{tx}} \mathbf{b}_b|^2}{\sigma_{\text{sen}}^2}$.

Proof. For the detailed derivation, refer to **Appendix K**. ■

3.6 Addressing the infinite constraints in C_{18} and H_2

We introduce **Proposition 6** to address the infinite constraint set arising from imperfect AOD in C_{18} and H_2 . Specifically, we first restructure H_2 and then employ the *S-Procedure*, as detailed in **Lemma 2**, to transform the infinite constraint set into a finite collection of linear inequalities. The overall procedure ensures that the original solution space is preserved.

Proposition 6. *Constraints C_{18} and H_2 can be equivalently rewritten as constraints I_1 and I_2 , shown below,*

$$C_{18}, H_2 \Leftrightarrow \begin{cases} I_1 : \begin{bmatrix} i_{t,s}^a & i_{t,s}^b \\ i_{t,s}^c & i_{t,s}^d \end{bmatrix} \succcurlyeq \mathbf{0}, \forall t \in \mathcal{T}, s \in \mathcal{S}, \\ I_2 : \xi_t \geq 0, \forall t \in \mathcal{T}, \end{cases}$$

where $i_{t,s}^a = \xi_t - \tilde{\mathbf{a}}(\bar{\theta}_t)^H \mathbf{F}_{t,s} \tilde{\mathbf{a}}(\bar{\theta}_t)$, $i_{t,s}^b = -\tilde{\mathbf{a}}(\bar{\theta}_t)^H \mathbf{F}_{t,s} \mathbf{a}(\bar{\theta}_t)$, $i_{t,s}^c = -\mathbf{a}(\bar{\theta}_t)^H \mathbf{F}_{t,s} \tilde{\mathbf{a}}(\bar{\theta}_t)$, $i_{t,s}^d = -\xi_t \cdot \epsilon_{\text{AOD}}^2 - \mathbf{a}(\bar{\theta}_t)^H \mathbf{F}_{t,s} \mathbf{a}(\bar{\theta}_t) - z_{t,s}$, $\mathbf{a}(\bar{\theta}_t) = \text{vec}(\mathbf{A}(\bar{\theta}_t))$, $\tilde{\mathbf{a}}(\bar{\theta}_t) = \text{vec}(\tilde{\mathbf{A}}(\bar{\theta}_t))$, $\mathbf{F}_{t,s} = -\sum_{c \in \mathcal{L}_{\text{rx}}} \sum_{b \in \mathcal{L}_{\text{tx}}} \frac{1}{\sigma_{\text{sen}}^2} \mathbf{d}_{b,c} \mathbf{d}_{b,c}^H \pi_{b,c,t,s}$, $\mathbf{d}_{b,c} = (\mathbf{Z}_{\text{tx}}^* \mathbf{b}_b^* \otimes \mathbf{Z}_{\text{rx}} \mathbf{c}_c)$, and ξ_t are newly introduced variables.

Proof. For the detailed derivation, refer to **Appendix L**. ■

3.7 Addressing the infinite constraints in C_{20} and H_3

We introduce **Proposition 7** to handle the couplings between variables $\rho_{c,s}$ and $\tau_{t,s}$ as well as the infinite constraint set resulting from imperfect RSI affecting C_{20} and H_3 . First, we apply propositional calculus to eliminate the binary couplings, simplifying the constraint structure. Subsequently, we leverage the *S-Procedure*, as detailed in **Lemma 2**, to convert the infinite constraint set into a finite set of linear inequalities. The overall procedure ensures that the original solution space remains unaltered.

$$C_{11}, C_{14}, C_{21} \Leftrightarrow \begin{cases} F_1 : \chi_{b,s} \geq \pi_{b,c,t,s}, \forall b \in \mathcal{L}_{\text{tx}}, c \in \mathcal{L}_{\text{rx}}, t \in \mathcal{T}, s \in \mathcal{S}, \\ F_2 : \rho_{c,s} \geq \pi_{b,c,t,s}, \forall b \in \mathcal{L}_{\text{tx}}, c \in \mathcal{L}_{\text{rx}}, t \in \mathcal{T}, s \in \mathcal{S}, \\ F_3 : \tau_{t,s} \geq \pi_{b,c,t,s}, \forall b \in \mathcal{L}_{\text{tx}}, c \in \mathcal{L}_{\text{rx}}, t \in \mathcal{T}, s \in \mathcal{S}, \\ F_4 : 2 + \pi_{b,c,t,s} \geq \chi_{b,s} + \rho_{c,s} + \tau_{t,s}, \forall b \in \mathcal{L}_{\text{tx}}, c \in \mathcal{L}_{\text{rx}}, t \in \mathcal{T}, s \in \mathcal{S}, \\ F_5 : \pi_{b,c,t,s} \in [0, 1], \forall b \in \mathcal{L}_{\text{tx}}, c \in \mathcal{L}_{\text{rx}}, t \in \mathcal{T}, s \in \mathcal{S}, \\ F_6 : \min_{\psi_t \in \Psi_t} \min_{\theta_t \in \Theta_t} \ell_{t,s}(\Omega') \geq \bar{\Lambda}_{\text{sinr},t} \cdot \tau_{t,s}, \forall t \in \mathcal{T}. \end{cases}$$

Proposition 7. Constraints C_{20} and H_3 can be equivalently rewritten as constraints $J_1, J_2, J_3, J_4, J_5,$ and $J_6,$ shown below,

$$C_{20} \Leftrightarrow \begin{cases} J_1 : \delta_{c,t,s} \leq \rho_{c,s}, \forall c \in \mathcal{L}_{\text{rx}}, t \in \mathcal{T}, s \in \mathcal{S}, \\ J_2 : \delta_{c,t,s} \leq \tau_{t,s}, \forall c \in \mathcal{L}_{\text{rx}}, t \in \mathcal{T}, s \in \mathcal{S}, \\ J_3 : \delta_{c,t,s} \geq \rho_{c,s} + \tau_{t,s} - 1, \forall c \in \mathcal{L}_{\text{rx}}, t \in \mathcal{T}, s \in \mathcal{S}, \\ J_4 : \delta_{c,t,s} \in [0, 1], \forall c \in \mathcal{L}_{\text{rx}}, t \in \mathcal{T}, s \in \mathcal{S}, \\ J_5 : \begin{bmatrix} \mathbf{J}_{t,s}^a & \mathbf{j}_{t,s}^b \\ \mathbf{j}_{t,s}^c & \mathbf{j}_{t,s}^d \end{bmatrix} \succeq \mathbf{0}, \forall t \in \mathcal{T}, s \in \mathcal{S}, \\ J_6 : \iota \geq 0, \end{cases}$$

where $\mathbf{J}_{t,s}^a = \iota \mathbf{I} + v^2 \bar{\Lambda}_{\text{sinr},t} \mathbf{F}_{t,s}, \mathbf{j}_{t,s}^b = v^2 \bar{\Lambda}_{\text{sinr},t} \mathbf{F}_{t,s} \bar{\mathbf{r}},$
 $\mathbf{j}_{t,s}^c = v^2 \bar{\Lambda}_{\text{sinr},t} \bar{\mathbf{r}}^H \mathbf{F}_{t,s}, \mathbf{j}_{t,s}^d = -\iota \cdot \epsilon_{\text{RSI}}^2 +$
 $v^2 \bar{\Lambda}_{\text{sinr},t} \bar{\mathbf{r}}^H \mathbf{F}_{t,s} \bar{\mathbf{r}} - \bar{\Lambda}_{\text{sinr},t} \sum_{c \in \mathcal{L}_{\text{rx}}} \|\mathbf{Z}_{\text{rx}} \mathbf{c}_c\|_2^2 \delta_{c,t,s} + z_{t,s},$
 $\mathbf{F}_{t,s} = -\sum_{c \in \mathcal{L}_{\text{rx}}} \sum_{b \in \mathcal{L}_{\text{tx}}} \frac{1}{\sigma_{\text{sen}}^2} \mathbf{d}_{b,c} \mathbf{d}_{b,c}^H \pi_{b,c,t,s},$ and
 $\mathbf{d}_{b,c} = (\mathbf{Z}_{\text{tx}}^* \mathbf{b}_b^*) \otimes (\mathbf{Z}_{\text{rx}} \mathbf{c}_c),$ while $\delta_{c,t,s}$ and ι are newly introduced variables.

Proof. For the detailed derivation, refer to **Appendix M.** ■

3.8 Addressing the vector nature of $\mathbf{f}(\Omega)$ and its dependence on C_{11} and C_{14}

We introduce **Proposition 8** to first reformulate the vector-valued function $\mathbf{f}(\Omega)$ into a scalarized form using carefully designed weights η_1 and η_2 . These weights are constructed to ensure that $\eta_1 f_1(\Omega)$ and $\eta_2 f_2(\Omega)$ map to distinct, non-overlapping intervals, with the explicit intent of prioritizing the minimization of time over energy consumption as a special case². Subsequently, we analyze the quadratic terms in $f_1(\Omega)$ which introduce complexity through their quadratic dependence on both \mathbf{w}_s and \mathbf{v}_s . By exploiting the binary-variable dependence of \mathbf{w}_s and \mathbf{v}_s , as specified in constraints C_{11} and C_{14} , we transform $f_1(\Omega)$ into an equivalent linear expression that is more tractable.

Proposition 8. Vector function $\mathbf{f}(\Omega)$ and constraints C_{11}, C_{14} is rewritten as $f'(\Omega)$, shown below,

$$\mathbf{f}(\Omega), C_{11}, C_{14} \Leftrightarrow f'(\Omega') \triangleq \eta_1 f'_1(\Omega') + \eta_2 f'_2(\Omega'),$$

where the coefficients η_1 and η_2 are weights that determine the relative priorities of $f'_1(\Omega')$ and $f'_2(\Omega')$, respectively. Here, $f'_1(\Omega') = S_{\text{dur}} \sum_{s \in \mathcal{S}} (\sum_{b \in \mathcal{L}_{\text{tx}}} \|\mathbf{b}_b\|_2^2 \cdot \chi_{b,s} + \sum_{c \in \mathcal{L}_{\text{rx}}} \|\mathbf{c}_c\|_2^2 \cdot \rho_{c,s})$ and $f'_2(\Omega') = S_{\text{dur}} \sum_{s \in \mathcal{S}} \omega_s \cdot \gamma_s$.

Proof. For the detailed derivation, refer to **Appendix N.** ■

3.9 Adding custom cutting planes to reduce binary search burden

To alleviate the burden of binary search, we introduce a set of problem-specific cutting planes, inspired by the approaches in [63], [64], but adapted to the structure of our problem. These tailored constraints, denoted as K_1 and K_2 , eliminate infeasible or redundant solutions³.

2. Prioritization of energy minimization can be addressed by adjusting the weights η_1 and η_3 . While this case is not the primary focus of our study, its impact is examined in **Appendix Q.**

3. Cutting planes are optional but they are highly effective in accelerating binary search by eliminating infeasible and redundant solutions.

We add constraint K_1 to impose an upper bound \bar{M}_u^{UB} on the numerator of the SNR, as shown below,

$$K_1 : \left| \mathbf{h}_u^H \mathbf{Z}_{\text{tx}} \mathbf{w}_s \right|^2 \leq \bar{M}_u^{\text{UB}}, \forall u \in \mathcal{U}, s \in \mathcal{S},$$

where $\bar{M}_u^{\text{UB}} = (\|\mathbf{Z}_{\text{tx}}^H \bar{\mathbf{h}}_u\|_2 + \epsilon_{\text{CSI}} \|\mathbf{Z}_{\text{tx}}\|_F)^2 P_{\text{tx}}^{\text{max}}$, and $P_{\text{tx}}^{\text{max}}$ is the maximum transmit power of the BS, i.e. $P_{\text{tx}}^{\text{max}} = \max_{b \in \mathcal{L}_{\text{tx}}} \|\mathbf{b}_b\|_2^2$. Here, \bar{M}_u^{UB} is an upper bound on the left-hand-side (LHS) of K_1 , obtained by applying the triangle inequality and the Cauchy-Schwarz inequality.

Additionally, we include constraint K_2 to address the inherent redundancy in the temporal ordering of users and targets, as shown below,

$$K_2 : \bar{\ell}_{s+1}(\Omega') \geq \bar{\ell}_s(\Omega'), \forall s \in \mathcal{S} \setminus \{S\},$$

where $\bar{\ell}_s(\Omega') \triangleq \sum_{b \in \mathcal{L}_{\text{tx}}} \|\mathbf{b}_b\|_2^2 \cdot \chi_{b,s} + \sum_{c \in \mathcal{L}_{\text{rx}}} \|\mathbf{c}_c\|_2^2 \cdot \rho_{c,s}$ represents the allocated power in S_s . Since the sequence in which users or targets are served over time does not affect the final outcome, it is beneficial to eliminate equivalent permutations. To this end, we enforce a non-increasing ordering of power allocation across timeslots. By requiring power to decrease or remain constant over time, we prune equivalent configurations that differ only in their ordering, thus significantly reducing the solution space. For the detailed derivation leading to K_1 and K_2 , refer to **Appendix O.**

The transformed problem $\mathcal{P}'(\Omega')$, which constitutes a MISDP, is presented below, while the full formulation of $\mathcal{P}'(\Omega')$, including the explicit set of constraints, is provided in **Appendix P** for further reference.

$$\begin{aligned} \mathcal{P}'(\Omega') : \min_{\Omega'} \quad & f'(\Omega') \\ \text{s.t.} \quad & C_1, C_2, C_4, C_5, C_6, C_7, C_8, C_9, C_{10}, \\ & C_{12}, C_{13}, C_{17}, C_{22}, D_1, D_2, D_3, D_4, \\ & E_1, E_2, F_1, F_2, F_3, F_4, F_5, H_1, H_4, \\ & I_1, I_2, J_1, J_2, J_3, J_4, J_5, J_6, K_1, K_2. \end{aligned}$$

The computational complexity of solving $\mathcal{P}'(\Omega')$ is highly dependent on the specific cuts, relaxations, and built-in heuristics employed by the solvers, in this case, MOSEK, CVX, and YALMIP. While it is not feasible to determine the exact computational complexity due to these factors, we provide an upper bound represented by the worst-case complexity, denoted by $\mathcal{C}_{\text{complexity}} = \mathcal{O}\left(\sum_{y=0}^Y \frac{X!}{(X-y)!} \left(L_{\text{tx}}^{X+y} L_{\text{rx}}^T\right) (m^2 n^2 + mn^3 + n^6)\right)$, where $X = \max\{U, T\}$, $Y = \min\{U, T\}$, $m = US + 2TS$, and $n = N_{\text{tx}} N_{\text{rx}} + N_{\text{tx}} + 2$.

4 SIMULATION RESULTS

We evaluate the investigated problem $\mathcal{P}'(\Omega')$ under various configurations, varying the SNR and SINR requirements, the number of allocated timeslots, the number of users and targets, and the severity of imperfect information.

We consider the Rician fading channel model, which allows line-of-sight (LoS) and non-LoS (NLoS) channel components. The channel for U_u is given by $\mathbf{h}_u = \gamma_u \mathbf{v}_u$, where γ_u accounts for large-scale fading and

$$\mathbf{v}_u = \sqrt{K/(K+1)} \mathbf{v}_u^{\text{LoS}} + \sqrt{1/(K+1)} \mathbf{v}_u^{\text{NLoS}}, \forall u \in \mathcal{U},$$

is the normalized small-scale fading, with $K = 100$ being the Rician fading factor. The LoS component is given by

TABLE 1: Simulation parameters.

Scenario	U	T	S_{com}	S_{sen}	S	β_u	$\theta_t \bar{\theta}_t$	r_u	$\psi_t \bar{\psi}_t$	Υ_{snr}	Λ_{sinr}	$\frac{\epsilon_{\text{CSI}}}{\sigma_{\text{com}}}$	ϵ_{AOD}	$\frac{\epsilon_{\text{RC}}}{\psi}$	$\frac{\epsilon_{\text{RSI}}}{\ \mathbf{R}\ _{\text{F}}}$	v	\bar{d}_c
I	1	1	1	1	1	90	[86, 134]	50	10^{-3}	80	2	0	0	0	0	0	—
II	1	1	1	1	1, 2	90	90, ..., 130	50	10^{-3}	[10, 150]	[0, 15]	0	0	0	0	0	—
III	1	1	1	1	1	90	90, 110, 130	50	10^{-3}	50	1, 2, 3	0	[0, 4.8]	[0, 1]	0	0	—
IV	1	1	1	1	1	90	90, 110, 130	50	10^{-3}	50, 70	1, 2, 3	[0, 10]	0	0	[0, 1]	[0, 0.3]	0.1, 0.2, 0.3
V	1	1	4	2	10	90	110	50	10^{-3}	50	2	0	0	0	0	0	—
VI	3	2	1	1	5	[45, 135]	[50, 130]	[40, 70]	[4, 12] 10^{-4}	50	4	0	0	0	0	0	—
VII	6	4	3	3	30	[45, 135]	[50, 130]	[40, 70]	[4, 12] 10^{-4}	50	[1, 6]	4, 14	2, 3	0.1, 0.3	0.3, 0.6	0.2	0.2

$\mathbf{v}_u^{\text{LoS}} = \frac{1}{\sqrt{N_{\text{tx}}}} e^{j\phi_{\text{tx}} \cos(\beta_u)}$, where β_u is the LoS angle, and the NLoS components are defined as $\mathbf{v}_u^{\text{NLoS}} \sim \mathcal{CN}(\mathbf{0}, \mathbf{I})$. For large-scale fading, we adopt the UMa channel model [65], modeled as $\gamma_u = 28 + 22 \log_{10}(r_u) + 20 \log_{10}(f_c)$ dB, where $f_c = 41$ GHz is the carrier frequency, and r_u denotes the distance between the BS and U_u , ranging in the interval [40, 70] m. We assume communication and sensing noise powers $\sigma_{\text{com}}^2 = -110$ dBm and $\sigma_{\text{sen}}^2 = -70$ dBm, respectively, which reflect the distinct operational environments. Specifically, sensing is often clutter/interference-limited, whereas communication is typically noise-limited.

The BS is equipped with $N_{\text{tx}} = 8$ transmit antennas and $N_{\text{rx}} = 16$ receive antennas. The transmit and receive directions span the interval from 45° to 135° with spacing of 5° degrees, yielding $D_{\text{tx}} = 19$ and $D_{\text{rx}} = 19$ distinct directions for transmission and reception, respectively. The transmit power ranges from 0.1 to 1 W in increments of 0.1 W, resulting in $P_{\text{tx}} = 10$ distinct power levels, while the receive power is fixed⁴ at 0.1 W, yielding $P_{\text{rx}} = 1$. The available beamwidths for transmission are $\{13^\circ, 26^\circ, 60^\circ\}$, while the beamwidth options for reception are $\{6^\circ, 13^\circ, 26^\circ\}$, leading to $B_{\text{tx}} = 3$ and $B_{\text{rx}} = 3$ beamwidth configurations. The mutual coupling parameters are set to $\delta_{\text{tx}} = \delta_{\text{rx}} = 0$, unless stated otherwise. The number of users U varies in the set $\{1, 2, 3, 4, 5, 6\}$, while the number of targets T ranges over $\{1, 2, 3, 4\}$.

The LoS angles of the user channels vary according to $\beta_u \in [45^\circ, 135^\circ]$, while the target AODs are drawn from $\theta_t \in [50^\circ, 130^\circ]$. Both the communication SNR and sensing SINR requirements are assumed to be identical across all users and targets, denoted by Υ_{snr} and Λ_{sinr} , respectively. Specifically, Υ_{snr} ranges within [10, 150], and Λ_{sinr} varies in the interval [1, 15]. Similarly, the number of timeslots allocated for communication and sensing, denoted by S_{com} and S_{sen} , respectively, are identical across users and targets, with values selected from the interval [1, 10]. The RC varies according to $\bar{\psi}_t \in [4 \cdot 10^{-4}, 12 \cdot 10^{-4}]$.

The normalized CSI error varies within $\frac{\epsilon_{\text{CSI}}}{\sigma_{\text{com}}} \in [0, 10]$ and the AOD error ranges as $\epsilon_{\text{AOD}} \in [0^\circ, 4.8^\circ]$. The normalized RC error lies within $\frac{\epsilon_{\text{RC}}}{\psi} \in [0, 1]$. The severity of RSI is controlled via v and ϵ_{RSI} , which are varied in the intervals $v \in [0, 1]$ and $\frac{\epsilon_{\text{RSI}}}{\|\mathbf{R}\|_{\text{F}}} \in [0, 1]$. Additionally, the distance between the antenna array centers ranges over $\bar{d}_c \in \{0, 0.1, 0.2, 0.3\}$ m, while the timeslot duration, S_{dur} ,

4. Power scaling in receive beamforming does not enhance the sensing SINR, as seen in (12), because numerator and the denominator are scaled proportionally, leaving the SINR unchanged. Thus, receive power is typically maintained at a fixed and low level.

is set to 1 ms. When not specified, all simulation results are the average over 50 independent realizations.

We consider two sets of scenarios: (i) single-user, single-target, single-timeslot settings (**Scenario I** to **Scenario IV**), and (ii) multi-user, multi-target, multi-timeslot settings (**Scenario V** to **Scenario VII**). The first set of scenarios provides key insights into how the various parameters influence system performance. Specifically, we examine the impact of user-target alignment, SNR and SINR requirements, beam adaptation, functionality selection, and imperfect information. The second set of scenarios reflects more general configurations, aiming to evaluate system performance at a larger scale. We evaluate our optimal user-target pairing against a state-of-the-art heuristic, analyze the time-energy trade-off, and benchmark the proposed approach against baseline methods. For clarity, **Table 1** provides a summary of the most relevant parameters for each scenario⁵.

4.1 Scenario I: Impact of user-target alignment

In this scenario, we analyze how the angular alignment between user and target influences the adaptation of power, direction, and beamwidth. The setup consists of a single user and a single target, with requirements, $\Upsilon_{\text{snr}} = 80$ and $\Lambda_{\text{sinr}} = 2$, assuming $S = S_{\text{com}} = S_{\text{sen}} = 1$. The user's LoS angle is $\beta = 90^\circ$, while the target's AOD θ varies from 86° to 134° , resulting in varying degrees of alignment. We also evaluate the impact of mutual coupling on beampattern shape and power consumption.

In Fig. 3(a), both user and target are perfectly aligned at 90° , and accordingly, the transmit and receive beams are also directed towards this angle. The transmit power to jointly serve both is 0.3 W, while the receive power for target sensing remains constant at 0.1 W. The transmit beamwidth is 13° , while the receive beamwidth is 6° , which remains fixed across all cases in Fig. 3, as there is no self-interference to mitigate, i.e., $v = 0$ (see Table 1).

As the target moves to 110° , as shown in Fig. 3(b), the transmit beam adapts by broadening its beamwidth to 26° and steering to 95° to accommodate the target's angular shift. Additionally, the transmit power increases to 0.5 W to compensate for the reduced radiated power due to beam widening. This adaptation is necessary, as the beam configuration from Fig. 3(a) is no longer suitable to jointly serve both the user and the target.

5. Throughout **Scenario I** to **Scenario IV**, we adopt $\eta_1 = 1$, $\eta_2 = 1$, and $\omega_1 = 1$, unless stated otherwise. In **Scenario V** to **Scenario VII**, η_1 remains fixed at 1, while η_2 is selected based on the weighting conditions derived in **Proposition 8**. For these scenarios, the structured weights ω_s are generated assuming $\Delta_\omega = \Delta_0 = 2$.

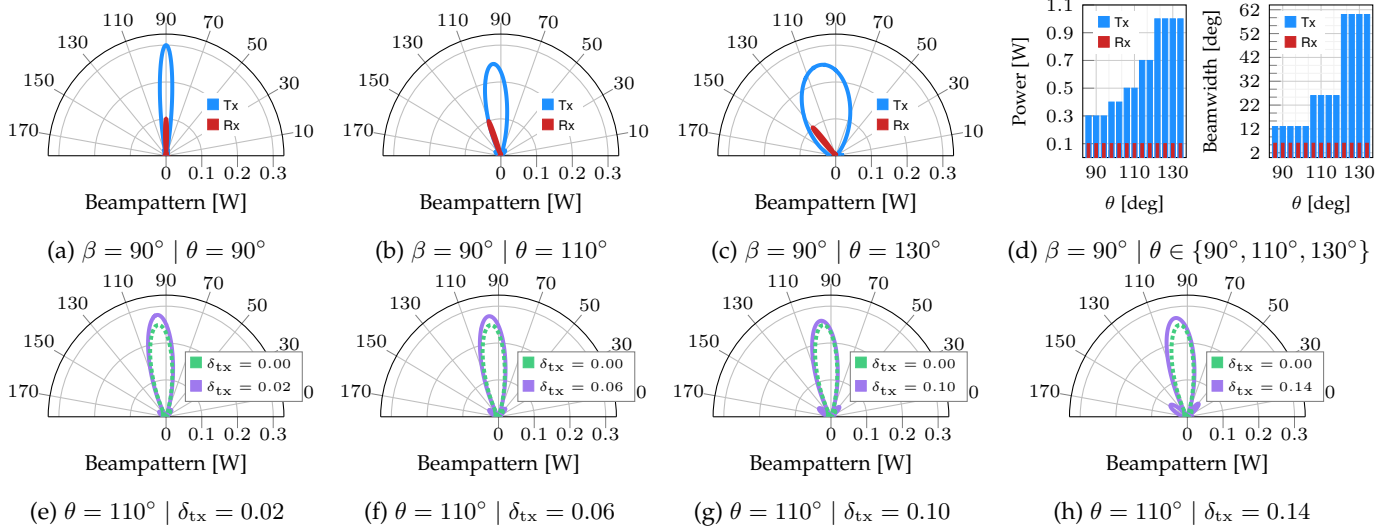


Fig. 3: Impact of user-target alignment on beam adaptation (Scenario I). The system can dynamically adapt beam direction, beamwidth, and transmit power in response to variations in user-target alignment, thereby ensuring that both communication and sensing requirements are satisfied. In addition, mutual coupling increases power/energy consumption by inducing energy leakage among adjacent antennas, which distorts the beampattern and reduces the effective power concentrated in the main lobe.

When the target reaches 130° , as illustrated in Fig. 3(c), a more pronounced behavior is observed. Specifically, the transmit beam is steered to 100° , while broadening its beamwidth to 60° . To counteract the significant loss in directionality caused by the wider beam, the transmit power is further increased to 1 W.

Meanwhile, Fig. 3(d) provides a more granular view, displaying transmit and receive power alongside beamwidth across a broader range of θ values. Additionally, since this setting enforces a shared timeslot for the user and the target, it allows us to analyze channel similarity, which takes the values 1, 0.2232, and 0.1438 for Fig. 3(a), Fig. 3(b), and Fig. 3(c), respectively, clearly illustrating the strong correlation between channel similarity and user-target alignment.

Fig. 3(e) to Fig. 3(h) illustrate the impact of mutual coupling on the beampattern, considering $\beta = 90^\circ$ and $\theta = 110^\circ$ (as in Fig. 3(b)). In this setting, the receive-side coupling is fixed to $\delta_{rx} = 0.02$, while the transmit-side coupling is varied as $\delta_{tx} = \{0.02, 0.06, 0.10, 0.14\}$. As δ_{tx} increases, stronger interactions among neighboring antenna elements arise, leading to increased power leakage. Consequently, higher transmit power is required to satisfy the sensing and communication constraints, since the coupling matrix \mathbf{Z}_{tx} in (2) induces phase distortions that reduce coherent combining across the array. Across all four cases in Fig. 3, the resulting beampatterns under mutual coupling exhibit higher main-lobe energy than the ideal case (with $\delta_{tx} = \delta_{rx} = 0$), indicating that both sensing and communication requirements remain satisfied. However, this comes at the cost of increased transmit power. Specifically, the selected powers for $\delta_{tx} = \{0.02, 0.06, 0.10, 0.14\}$ are 0.6W, 0.7W, 0.8W and 1W, respectively, whereas the nominal case without mutual coupling requires only 0.5W. This increase represents the additional power needed to guarantee the ISAC constraints under coupling effects. Furthermore, the sidelobe levels become more pronounced as δ_{tx} increases, reflecting the growing distortion of the array response due

to mutual coupling.

4.2 Scenario II: Impact of SNR/SINR requirements and functionality selection

In this scenario, we analyze how energy consumption varies under different SNR and SINR requirements. We also investigate how functionality selection influences performance. The setup consists of a single user and a single target, with requirements $\Upsilon_{\text{snr}} = [10, 150]$ and $\Lambda_{\text{sirr}} = [0, 15]$.

In Fig. 4, the consumed energy is depicted using a color heatmap across five instances, where the user’s LoS angle is fixed at $\beta = 90^\circ$, and the target’s AOD θ takes values from $\{90^\circ, 100^\circ, 110^\circ, 120^\circ\}$. In Fig. 4(a) to Fig. 4(d), we set $S = 1$, meaning the user and target share the same timeslot. This reflects a common assumption in the existing literature, where timeslot functionality is static, forcing both functionalities to be active simultaneously. In Fig. 4(e), we set $S = 2$, allowing the user and target to be time-multiplexed when a single timeslot is insufficient to serve both. This configuration enables flexible functionality selection across timeslots, mitigating allocation infeasibility.

In Fig. 4(a), due to the high alignment between user and target, all allocations are feasible, with energy consumption not exceeding 0.7 mJ. In Fig. 4(b), a misalignment of $\theta - \beta = 10^\circ$, leads to the appearance of infeasible regions, represented by white areas, particularly for $\Lambda_{\text{sirr}} \geq 12$. Fig. 4(c) illustrates a misalignment of $\theta - \beta = 20^\circ$, leading to a more noticeable reduction in the feasible regions. Moreover, the number of allocations requiring high energy consumption rises significantly compared to previous cases. In Fig. 4(d), with a misalignment of $\theta - \beta = 30^\circ$, total energy consumption increases sharply, even for moderate SNR and SINR requirements. Additionally, regions requiring maximum energy expand noticeably, while those with minimal energy contract. The number of infeasible regions also increases significantly.

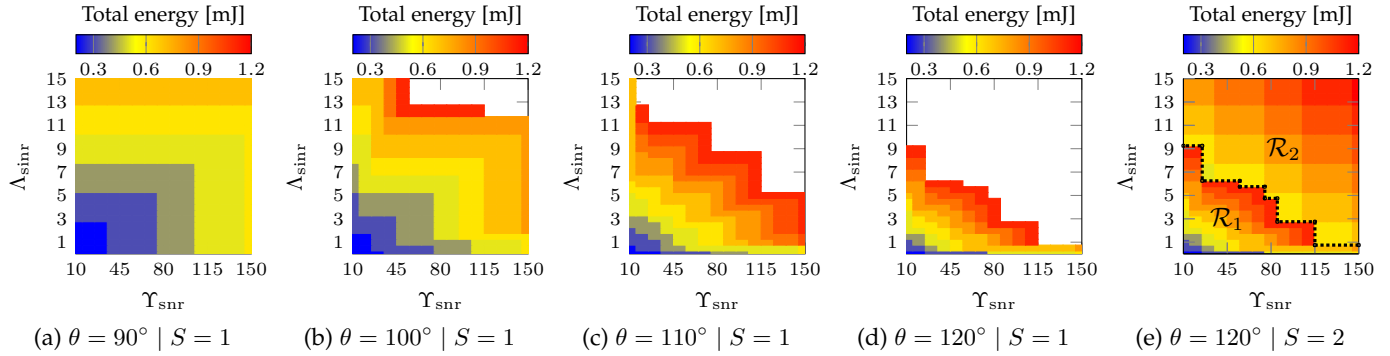


Fig. 4: Impact of SNR/SINR requirements and functionality selection on energy consumption (*Scenario II*). The energy consumption is affected by SNR and SINR requirements, with higher demands leading to greater infeasible regions. While static functionality selection (Fig. 4(a) to Fig. 4(d)) is more prone to infeasibility, flexible functionality selection (Fig. 4(e)) significantly increases the feasible solution space and improves adaptability via intelligent switching between joint and separate user/target service.

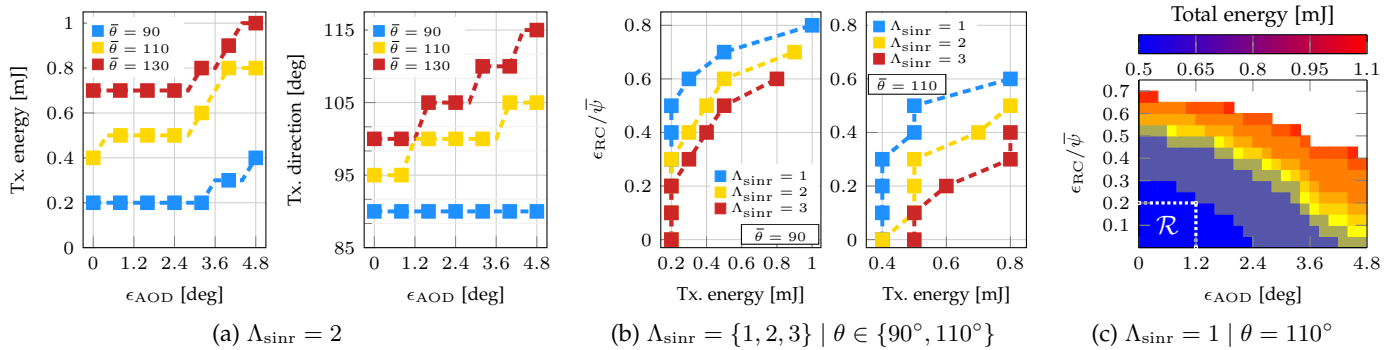


Fig. 5: Impact of imperfect AOD and RC on energy consumption (*Scenario III*). Energy expenditure is impacted by AOD and RC uncertainty. Their combined effect reveals operational regions characterized by constant total energy consumption despite imperfect information. This stability is attributed to the discrete power levels, which often provides a surplus margin in satisfying SNR and SINR requirements, thereby providing an inherent degree of robustness.

Fig. 4(e) illustrates how enabling flexible functionality selection resolves allocation infeasibility. The operating conditions are identical to those in Fig. 4(d). The black dotted line partitions the energy plane into two regions: \mathcal{R}_1 , where a single timeslot is used, and \mathcal{R}_2 , where two timeslots are active. This boundary marks the point at which the system switches from one to two timeslots. The weighting parameters ($\eta_1 = 1$ and $\eta_2 = 2$) are chosen such that the second timeslot becomes active only when allocation under a single timeslot is infeasible. Immediately to the left of the boundary (within \mathcal{R}_1), the allocated energies are high and approach their maximum feasible values. Just to the right of the boundary (within \mathcal{R}_2), the energies drop sharply because the system time-multiplexes the user and the target. In this mode, each can be served with a narrower beam and therefore with less energy, at the expense of using additional time resources. Overall, enabling flexible functionality selection on a per-timeslot basis expands the feasible solution space by approximately 250%.

4.3 Scenario III: Impact of imperfect AOD and RC

In this scenario, we investigate how the transmit beam adapts to varying levels of uncertainty in the target's AOD and RC. We also examine how combined uncertainties in AOD and RC influence the energy consumption. The setup

remains consistent with assumptions in **Scenario II**. The communication SNR requirement is $\Upsilon_{\text{snr}} = 50$, and the user's LoS is $\beta = 90^\circ$. The estimated target's AOD $\bar{\theta}$ varies within $\{90^\circ, 110^\circ, 130^\circ\}$, while the estimated RC is set to $\bar{\psi} = 10^{-3}$. Here, AOD and RC errors range the intervals $\epsilon_{\text{AOD}} \in [0^\circ, 4.8^\circ]$ and $\frac{\epsilon_{\text{RC}}}{\bar{\psi}} \in [0, 1]$, respectively.

Fig. 5(a) illustrates the transmit energy and direction as functions of ϵ_{AOD} . Both the transmit energy and the steering angle exhibit monotonically non-decreasing trends as ϵ_{AOD} increases. Specifically, addressing AOD uncertainty requires maintaining sufficient radiated energy in the angular neighborhood of $\bar{\theta}$ to satisfy the SINR requirement. While beam widening could mitigate this issue, it is unsuitable in the considered setting, as doubling the beamwidth would at least halve the directional gain, thereby requiring a proportional increase in transmit power and substantially degrading the objective function. Instead, the system combats AOD uncertainty through power and direction adaptation. In particular, increasing transmit power while maintaining the beamwidth incurs a lower cost than widening the beam to achieve the required performance. However, when power increment alone is insufficient, the transmit beam is steered closer to $\bar{\theta}$. As this shift reduces the energy delivered to the user, a compensatory increase in transmit power may be needed to maintain the communication SNR requirement.

Fig. 5(b) shows the impact of RC uncertainty on transmit energy for $\bar{\theta} = \{90^\circ, 110^\circ\}$. As expected, greater RC uncertainty degrades sensing performance. For $\bar{\theta} = 90^\circ$, the system remains feasible under $\Lambda_{\text{sinr}} = 1$, even with RC errors up to 80%. However, stricter $\Lambda_{\text{sinr}} = \{2, 3\}$ reduce the tolerable error to 70% and 60%, respectively, beyond which the allocation becomes infeasible. For $\bar{\theta} = 110^\circ$, a similar trend is observed, though energy consumption increases more sharply, even for small RC errors.

Fig. 5(c) illustrates the combined effect of AOD and RC uncertainty on total energy consumption for $\bar{\theta} = 110^\circ$ and $\Lambda_{\text{sinr}} = 1$. The results show that this configuration can tolerate moderate RC errors up to 20% and AOD deviations up to 1.2° , as represented by region \mathcal{R} , without incurring additional energy costs. This stems from the discrete nature of power levels, which often results in achieved SNR and SINR exceeding the required thresholds, rather than matching them precisely, thereby providing resilience to errors.

4.4 Scenario IV: Impact of imperfect CSI and RSI

In this scenario, we examine how varying levels of uncertainty in CSI and RSI affect energy consumption. The same parameter settings as in **Scenario III** are maintained. The normalized CSI error varies within $\frac{\epsilon_{\text{CSI}}}{\sigma_{\text{com}}} \in [0, 10]$, while the normalized RSI error is controlled by $\frac{\epsilon_{\text{RSI}}}{\|\mathbf{R}\|_F} \in [0, 1]$.

Fig. 6(a) shows that transmit energy increases with growing CSI error for both $\Upsilon_{\text{snr}} = 50$ and $\Upsilon_{\text{snr}} = 70$. When the user and target are well aligned (i.e., $\theta = 90^\circ$), the impact is moderate, even for errors up to $10\sigma_{\text{com}}$. However, CSI error becomes more detrimental with stronger misalignment (i.e., $\theta = 110^\circ$ and $\theta = 130^\circ$), which significantly amplifies energy consumption. Specifically, for $\theta = 130^\circ$, the system becomes infeasible for CSI errors as small as $2\sigma_{\text{com}}$ and σ_{com} when $\Upsilon_{\text{snr}} = 50$ and $\Upsilon_{\text{snr}} = 70$, respectively.

Fig. 6(b) illustrates the impact of RSI as a function of the distance between the transmit and receive arrays, focusing on the deterministic component whose severity is governed by v . For closely spaced arrays (i.e., $\bar{d}_c = 0.1$ m), RSI causes a pronounced increase in the required transmit energy, even for small values of v , which correspond to highly effective self-interference cancellation. As the inter-array distance increases, the influence of RSI progressively weakens, consistent with trends reported in prior studies (e.g., [66]). For instance, at $\bar{d}_c = 0.3$ m, the influence is modest, with transmit energy remaining at 0.4 mJ for $v \leq 0.2$, and rising slightly to 0.5 mJ for $0.2 < v < 0.45$.

Fig. 6(c) illustrates the impact of the stochastic RSI component on transmit energy, assuming $v = 0.15$ and $\bar{d}_c = 0.2$ m. The results demonstrate that, across all three Λ_{sinr} levels, the system can tolerate relatively large stochastic residuals. This resilience is attributed to both effective self-interference cancellation and sufficiently distanced arrays, which jointly mitigate the impact of direct coupling.

Fig. 6(d) examine the joint impact of CSI and RSI uncertainties on total energy consumption when $\theta = 110^\circ$, $\Upsilon_{\text{snr}} = 50$, and $\Lambda_{\text{sinr}} = 1$. Notably, the system demonstrates greater robustness to RSI variations compared to CSI errors, primarily due to the small value of $v = 0.1$, which reflects effective self-interference cancellation. Remarkably, energy consumption remains stable within region \mathcal{R} , despite the

presence of both uncertainties. This behavior mirrors the robustness observed in Fig. 5(c), and is largely attributed to the use of discrete power levels, which often satisfy system requirements with excess power.

4.5 Scenario V: Impact of tradeoff weights design

In this scenario, we investigate the impact of weights η_1 and η_2 on time and energy consumption. We also analyze how the weights ω_s (within function $f_2(\mathbf{\Omega})$) influence the cohesiveness of timeslot allocation. The parameters remain consistent with **Scenario III**, considering the following: $\beta = 90^\circ$, $\theta = 110^\circ$, $S_{\text{com}} = 4$, $S_{\text{sen}} = 2$, and $S = 10$.

Fig. 7(a) corresponds to the case $\eta_1 = 10$ and $\eta_2 = 0$, where the objective focuses exclusively on minimizing energy consumption. Under this criterion, the system attains the minimum total energy expenditure of 1.2 mJ by assigning the user and the target to disjoint timeslots. This separation avoids the additional energy cost associated with joint servicing, caused by the poor angular alignment between the user and the target. However, this energy-optimal strategy results in the maximum number of active timeslots, namely 6, corresponding to a time consumption of 6 ms. This figure also shows the specific timeslots in which the target is sensed and the transmit beampatterns for each timeslot. Notably, S_2, S_3, S_7 , and S_{10} employ the same transmit beam, as it achieves the minimum energy required to satisfy the SNR constraint. Similarly, S_1 and S_6 , employ the same transmit beam to illuminate the target, satisfying its SINR requirement at minimum energy.

Fig. 7(b) illustrates the opposite extreme, with $\eta_1 = 0$ and $\eta_2 = 10$, where the objective is to minimize time consumption only, assuming uniform weights $\omega_s = 1$. Here, the user and target are jointly served in S_5 and S_7 , while the user is served independently in S_1 and S_9 . In particular, the minimum possible number of timeslots is achieved, totaling 4 and requiring 4 ms. Since energy consumption is not included in the objective, multiple solutions can achieve this minimum time, and the resulting total energy consumption (3.2 ms) is not optimized. Moreover, the active timeslots are non-contiguous, highlighting the lack of any intrinsic preference for cohesive allocation. Furthermore, four distinct beampatterns are observed, specifically, red beams correspond to joint user-target servicing, while blue beams represent timeslots where only the user is served.

Fig. 7(c) considers the same time-only objective ($\eta_1 = 0$, $\eta_2 = 10$) but with structured weights ω_s defined according to **Lemma 1**. While the minimum time consumption of 4 ms is again achieved, the introduction of non-uniform weights promotes cohesive allocation, resulting in exactly four contiguous active timeslots. This contrasts with the non-contiguous pattern observed in Fig. 7(b). As energy is still excluded from the objective, the total energy consumption remains unoptimized, amounting to 3.6 mJ. Additionally, four distinct beampatterns are shown, corresponding to each active timeslot.

Fig. 7(d) corresponds to $\eta_1 = 1$ and $\eta_2 = 10$, following the weight selection guideline in **Proposition 8**, which prioritizes time minimization while retaining energy awareness. The weights ω_s again follow **Lemma 1**, promoting contiguous timeslot usage. The minimum time consumption

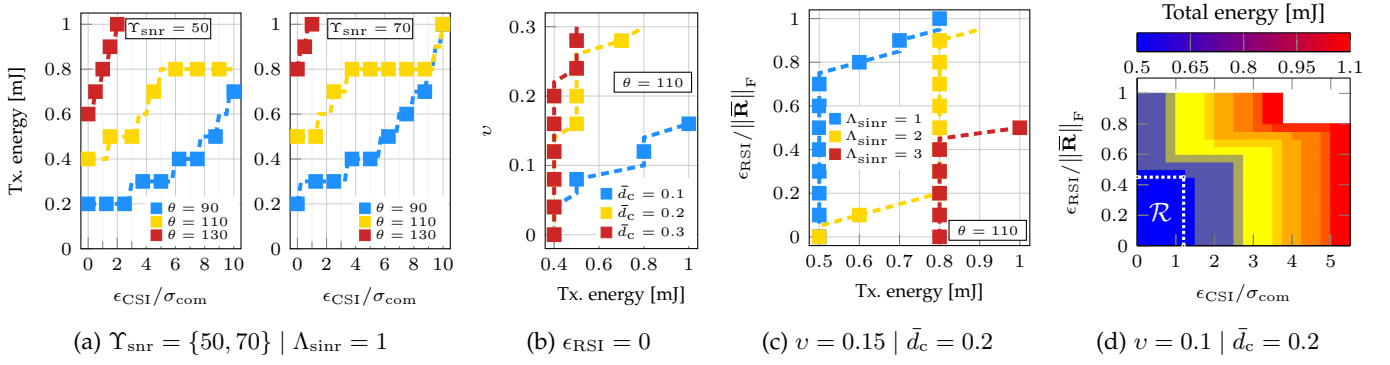


Fig. 6: Impact of imperfect CSI and RSI on energy consumption (*Scenario IV*). Effective self-interference cancellation (small v) results in minimal energy increase, whereas ineffective cancellation (large v) can result in excessive power demands and infeasible allocations. Furthermore, maintaining a reasonable inter-array distance significantly reduces self-interference effects.

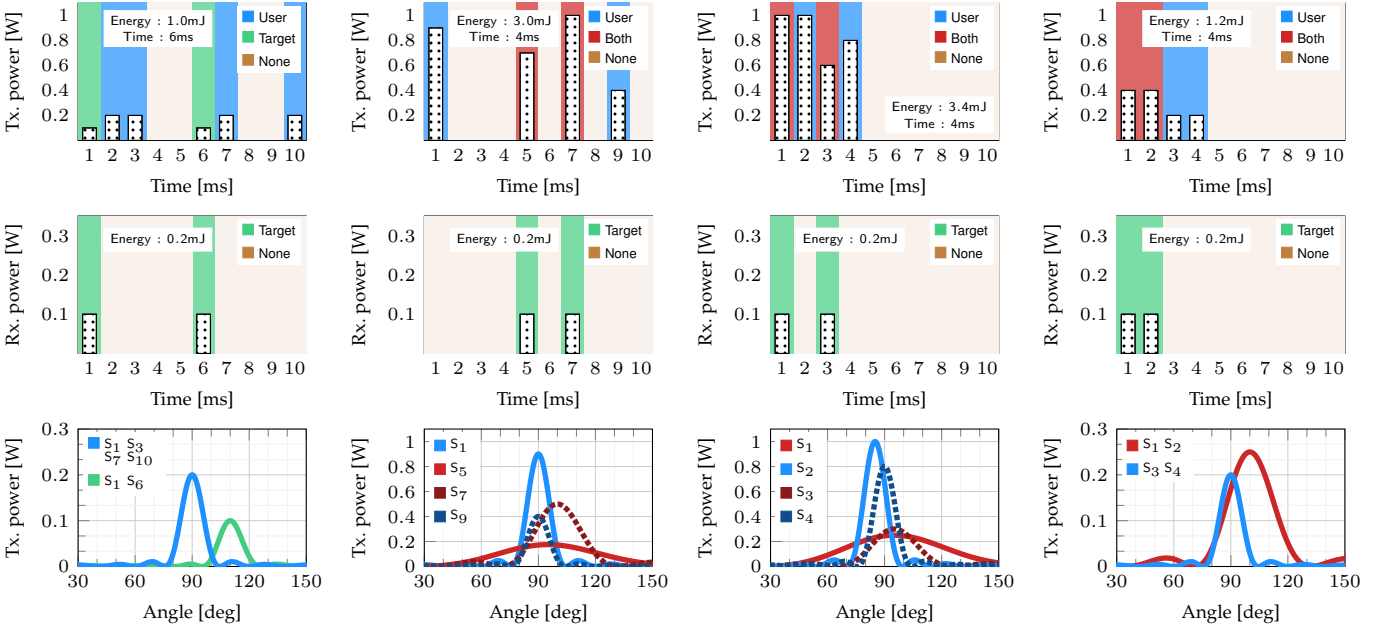


Fig. 7: Impact of weight design on resource economy and timeslot cohesion (*Scenario V*). The weights η_1 and η_2 play a critical role in steering the optimization between energy and time consumption. The choice of weights also influences whether joint user-target servicing is favored or whether individual servicing is more energy- or time-efficient. Importantly, the use of structured weights ω_s proves effective in promoting cohesive timeslot usage.

of 4 ms is preserved. Owing to constraint K_2 , the per-timeslot energies are sorted in decreasing order, yielding a total energy consumption of 1.4 mJ. This value is slightly higher than the energy-optimal case in Fig. 7(a), where energy minimization was the sole objective, but significantly lower than in the purely time-driven cases. Moreover, only two distinct beampatterns are required: one for joint user-target servicing, and another for the user when served individually.

4.6 Scenario VI: Impact of flexible user-target pairing

In this scenario, we evaluate the performance of dynamic user-target pairing in contrast to fixed-criterion pairing. The configuration considers $U = 3$, $T = 2$, $S = 5$, $\Upsilon_{\text{snr}} = 50$,

and $\Lambda_{\text{sinr}} = 4$, with random values for β_u , θ_t , r_u , and $\bar{\psi}_t$ drawn from the ranges specified in **Table 1**.

Figure 8 shows the allocation outcomes for the first 10 realizations (out of 50) using our proposed approach (**OPT**) and a state-of-the-art baseline (**BL1**) adapted from [38]. In particular, **OPT** ensures dynamic and optimal user-target pairing, while **BL1** constructs a bipartite graph with users and targets as nodes, where edge weights represent channel similarity. A matching game is then solved to determine pairings that maximize overall alignment, reducing resource consumption through beam and timeslot sharing. To illustrate the pairing decisions, the figure displays the specific user and target served in each timeslot, along with the corresponding time and transmit energy consumption per realization.

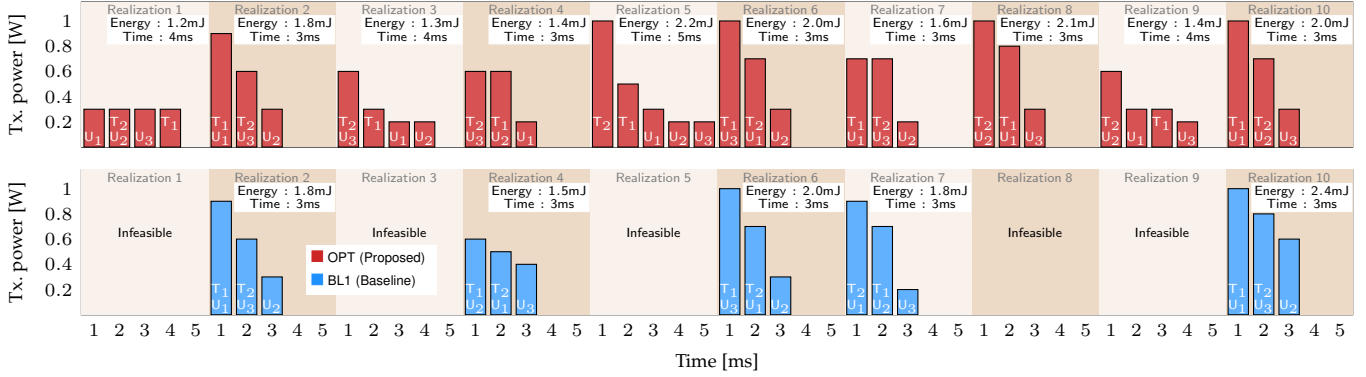


Fig. 8: Impact of flexible user-target pairing on resource economy (Scenario VI). Dynamic pairing is beneficial for improving both feasibility and resource efficiency. Unlike fixed strategies, the proposed approach adapts pairings based on the system conditions and service requirements, reducing the likelihood of infeasibility and enabling joint or separate servicing as needed. This flexibility is critical for ensuring energy-efficient operation and avoiding costly re-allocations due to infeasibility.

In **OPT**, the number of active timeslots per realization ranges from 3 (when user and targets are paired) to 5 (when users and targets are served separately). In contrast, **BL1**, enforces pairings via matching, and consequently always employs exactly 3 timeslots, i.e., the maximum of U and T . Here, **OPT** yields feasible allocations in all first 10 realization, whereas **BL1** achieves feasibility in only 5. Of these, only 2 (realizations 2 and 6) achieve the same optimal value as **OPT**, while the remaining feasible allocations (realizations 4, 7, and 10) incur higher energy consumption due to suboptimal pairings. Across all 50 realizations, **OPT** yields only 4 infeasible allocations, caused by insufficient power to overcome low RC values or adverse CSI conditions, resulting in a 92% feasibility rate. In contrast, **BL1** produces feasible outcomes in only 27 realizations (54%), significantly underperforming compared to **OPT**. This performance gap stems from the baseline’s limited ability to account for the complexity of real-world conditions. Its reliance on a fixed, single criterion fails to capture contextual factors, which are essential for making optimal pairing decisions.

4.7 Scenario VII: Impact of imperfect information and comparison with baseline methods

In this scenario, we evaluate the impact of imperfect information on energy and time consumption. Additionally, we compare our proposed approach against five baselines that differ in their strategies for user-target pairing, beam adaptation, timeslot functionality selection, and in whether they optimize for energy or time minimization alone. The scenario considers $U = 6, T = 4, S_{\text{com}} = 3, S_{\text{sen}} = 3$, with the remaining parameters detailed in **Table 1**.

Figure 9(a) illustrates the energy and time consumption of the proposed approach under both perfect and imperfect information conditions, plotted as a function of Λ_{sinr} . To capture performance variability, representative individual error levels in AOD ($\epsilon_{\text{AOD}} = 3^\circ$), RC ($\epsilon_{\text{RC}} = 0.3\psi$), RSI ($v = 0.2, \epsilon_{\text{RSI}} = 0.6\|\mathbf{R}\|_{\text{F}}$), and CSI ($\epsilon_{\text{CSI}} = 14\sigma_{\text{com}}$) are considered, along with a scenario that incorporates all sources of uncertainty ($\epsilon_{\text{AOD}} = 2^\circ, \epsilon_{\text{RC}} = 0.1\psi, v = 0.2, \epsilon_{\text{RSI}} = 0.3\|\mathbf{R}\|_{\text{F}}, \epsilon_{\text{CSI}} = 4\sigma_{\text{com}}$). Separate plots are provided for energy and time consumption, along with a third plot depicting their combined consumption. Uncertainty is counteracted through increased energy usage, extended

transmission time, or a combination of both, depending on the severity and nature of the errors. Given the higher priority assigned to minimizing time consumption, the system initially mitigates uncertainty by increasing transmit power, deferring the activation of extra timeslots as a secondary measure. As a result, energy consumption exhibits pronounced non-monotonic fluctuations as Λ_{sinr} increases, whereas time consumption grows gradually and monotonically. This occurs because the activation of additional timeslots (as a last resort to preserve feasibility) enables individual servicing of users or targets, which can often be accomplished with narrower beams and reduced transmit power. Consequently, energy consumption may drop even as time usage increases, reflecting a transition to a different operating point.

Figure 9(b) compares the performance of six schemes across three plots: energy consumption, time consumption, and a joint metric combining both, similarly to Fig. 9(a). The benchmarked schemes are as follows:

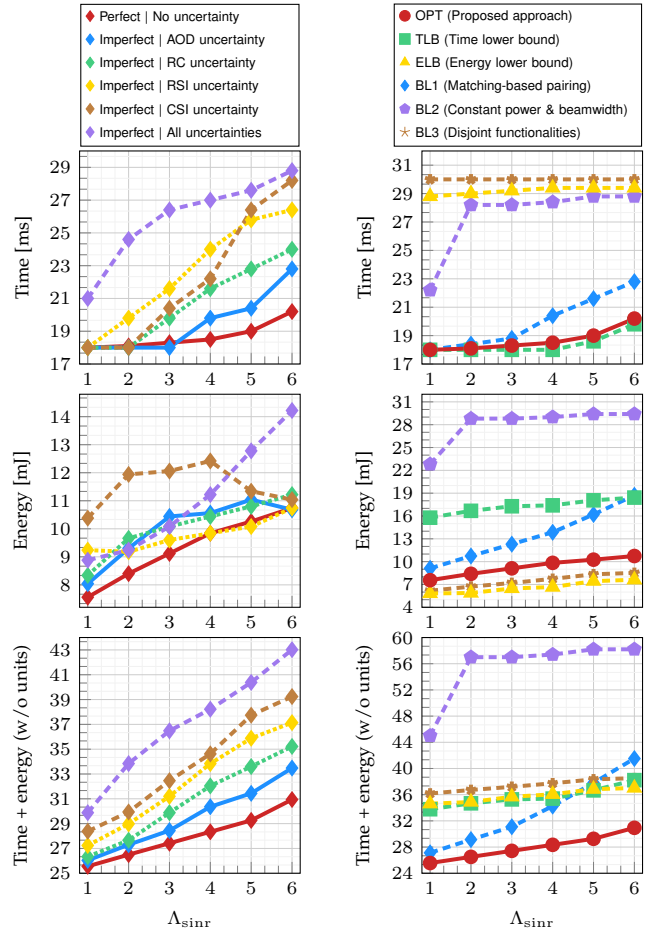
- OPT**: The proposed approach prioritizes minimizing time consumption over energy. It ensures optimal timeslot allocation, pairing, beam adaptation, and functionality selection.
- TLB**: This baseline serves as a time lower bound, as it considers only time minimization in its objective function, completely disregarding energy consumption.
- ELB**: This baseline serves as an energy lower bound, as it considers only energy minimization in its objective function, entirely disregarding time consumption.
- BL1**: A baseline which, like **OPT**, prioritizes time over energy. However, it relies on heuristic user-target pairing, adapted from [38], enforcing always concurrent service.
- BL2**: A baseline which, like **OPT**, prioritizes time over energy, but has limited beam adaptation, as it uses constant transmit power and beamwidth, similar to [20], [21].
- BL3**: This baseline separates communication and sensing into distinct timeslots, disallowing joint operation, as in [37].

REMARK 5. To mitigate infeasibility, particularly in less flexible schemes such as **BL1**, which often yield a high number of infeasible allocations, a simple fallback strategy is employed. In particular, users and targets are assigned to disjoint timeslots and served using maximum transmit power with the narrowest beam directed along the LoS or AOD direction. If this allocation satisfies all the

constraints, it is accepted as a feasible solution. Otherwise, the realization is excluded from the analysis.

In terms of time consumption, **TLB** performs best, as it completely ignores energy consumption. **OPT** closely follows, achieving comparable time efficiency with a performance gap of less than 2%, while simultaneously maintaining energy awareness. **ELB** performs poorly in terms of time consumption, as time is excluded from its optimization objective. Any favorable outcomes occur coincidentally, typically when users and targets are well aligned, enabling timeslot sharing. **BL1** performs well at low values of Λ_{sinr} , but its effectiveness deteriorates rapidly as Λ_{sinr} increases. This decline stems from its rigid pairing, which becomes increasingly infeasible under stricter sensing requirements and the demand for joint servicing. In such cases, fallback reallocation (see *Remark 5*) leads to additional resource use. **BL2** underperforms due to its fixed transmit power and beamwidth configuration, which limits adaptability to varying alignment conditions. In particular, the use of narrow beams, unless user and target are highly aligned, impedes joint servicing, frequently requiring additional timeslots to meet system requirements. **BL3** yields the worst performance in terms of time, as it enforces disjoint communication and sensing by design, resulting in consistently higher time consumption. At $\Lambda_{\text{sinr}} = 6$, compared to **OPT**, the additional time consumption incurred by **BL1**, **BL2**, **ELB**, and **BL3** is 13%, 43%, 45%, and 49%, respectively.

Regarding energy consumption, **ELB** achieves the best performance, as it exclusively optimizes for energy, completely disregarding time consumption. Despite prioritizing time minimization, the proposed approach **OPT** still performs competitively, maintaining a low energy consumption. As expected, **TLB** exhibits poor energy performance since energy is not accounted for in its optimization objective. **BL1** incurs significantly higher energy consumption than **OPT**, primarily due to suboptimal user-target pairings that demand more transmit power than the optimal case. **BL2** shows degraded energy performance as it operates under a fixed power and beamwidth regime, which limits adaptability to changing conditions. Although it always transmits at a constant power level, its energy consumption is not flat across Λ_{sinr} values. This is because occasional alignment between users and targets can still enable beam sharing, yielding energy savings, though this effect is primarily confined to low Λ_{sinr} values. Lastly, **BL3** achieves excellent energy performance by decoupling communication and sensing into separate timeslots. This separation enables the use of highly directional beams and minimal power tailored to each function, making it more energy-efficient than joint servicing. However, this advantage comes at the cost of time efficiency, as **BL3** consistently employs the maximum number of timeslots, an unfavorable outcome given the problem's emphasis on minimizing time consumption. We also show the joint consumption of time and energy, demonstrating that **OPT** achieves the best trade-off. It outperforms **ELB**, **TLB**, **BL3**, **BL1**, and **BL2** by 20%, 24%, 25%, 34%, and 88%, respectively.



(a) Impact of imperfect information (b) Comparison with baseline methods

Fig. 9: Impact of imperfect information on resource economy and comparison with baseline methods (*Scenario VII*). **OPT** is effective under both perfect and imperfect information conditions. Despite prioritizing time minimization, it preserves energy efficiency and is robust against uncertainties. Compared to five baseline schemes, it achieves the most favorable balance between time and energy consumption. These results highlight the critical role of optimized timeslot allocation, dynamic user-target pairing, adaptive beamforming, and flexible functionality selection in enabling efficient joint communication and sensing.

5 CONCLUSIONS

This work investigated a comprehensive RRM framework for ISAC systems, in which discrete power control, beam direction, and beamwidth at both the transmitter and receiver are jointly optimized. The proposed design further incorporates timeslot allocation, dynamic user-target pairing, and flexible functionality selection, all under imperfect information arising from estimation errors in AOD, RC, CSI, and RSI. The objective is to jointly minimize time and energy consumption, with a strict prioritization of time efficiency. The resulting RRM problem is formulated as a multi-objective, semi-infinite, nonconvex MINLP. By exploiting the underlying problem structure and revealing hidden convexity, we derived an exact reformulation as a MISDP, which enables the computation of globally optimal solutions using general-purpose solvers. Through extensive simulations, we demonstrated the individual and joint im-

pact of the key design components, namely timeslot allocation, adaptive beam configuration, dynamic user-target pairing, and timeslot-level functionality selection. The results show that the proposed framework effectively allocates resources to preserve feasibility under increasingly stringent requirements and imperfect information conditions. In particular, feasibility is primarily maintained through adaptive transmit power increases, with timeslot extension serving as a secondary mechanism, in accordance with the imposed prioritization of time minimization. Compared to a broad range of baseline schemes, the proposed approach consistently achieves the most favorable tradeoff between time and energy consumption. It closely approaches the performance of the time-optimal lower bound while substantially outperforming energy-centric and non-adaptive baselines. Overall, this work provides a versatile and practically grounded optimization framework for ISAC systems, offering valuable design insights for future high-frequency networks operating under time-critical, energy-constrained, and imperfect-information conditions.

ACKNOWLEDGMENT

This research was supported by the Federal Ministry of Research, Technology and Space (BMFTR) under Grant 16KIS2411.

REFERENCES

- [1] F. Liu, C. Masouros, A. P. Petropulu, H. Griffiths, and L. Hanzo, "Joint radar and communication design: Applications, state-of-the-art, and the road ahead," *IEEE Trans. Commun.*, vol. 68, no. 6, pp. 3834–3862, 2020.
- [2] A. R. Balef, S. Maghsudi, and S. Stanczak, "Adaptive energy-efficient waveform design for joint communication and sensing using multiobjective multiarmed bandits," in *Proc. of WSA & SCC*, 2023, pp. 1–6.
- [3] F. Liu, Y. Cui, C. Masouros, J. Xu, T. X. Han, Y. C. Eldar, and S. Buzzi, "Integrated sensing and communications: Toward dual-functional wireless networks for 6G and beyond," *IEEE J. Sel. Areas Commun.*, vol. 40, no. 6, pp. 1728–1767, 2022.
- [4] G. Yao and Y. Pi., "Terahertz active imaging radar: preprocessing and experiment results," vol. 10, no. 1, pp. 1–8, 2014.
- [5] R. Askar, J. Chung, L. John, T. Merkle, S. Wittig, M. Schmieder, Y. Suh, J. Lee, B. Baumann, M. Peter, T. Hausteiner, W. Keusgen, and S. Stanczak, "Mobilizing the terahertz beam: D-band analog-beamforming front-end prototyping and long-range 6G trials," *IEEE Wireless Commun.*, pp. 1–8, 2024.
- [6] T. Mao, J. Chen, Q. Wang, C. Han, Z. Wang, and G. K. Karagiannis, "Waveform design for joint sensing and communications in millimeter-wave and low terahertz bands," *IEEE Trans. Commun.*, vol. 70, no. 10, pp. 7023–7039, 2022.
- [7] Y. Zhuo, T. Mao, H. Li, C. Sun, Z. Wang, Z. Han, and S. Chen, "Multi-beam integrated sensing and communication: State-of-the-art, challenges and opportunities," *IEEE Commun. Mag.*, vol. 62, no. 9, pp. 90–96, 2024.
- [8] L. F. Abanto-Leon and S. Maghsudi, "Hierarchical functionality prioritization in multicast ISAC: Optimal admission control and discrete-phase beamforming," *IEEE Commun. Lett.*, pp. 1–5, 2024.
- [9] Z. Ren, Y. Peng, X. Song, Y. Fang, L. Qiu, L. Liu, D. W. K. Ng, and J. Xu, "Fundamental CRB-rate tradeoff in multi-antenna ISAC systems with information multicasting and multi-target sensing," *IEEE Trans. Wireless Commun.*, vol. 23, no. 4, pp. 3870–3885, 2024.
- [10] L. Xu, S. Sun, Y. D. Zhang, and A. Petropulu, "Joint antenna selection and beamforming in integrated automotive radar sensing-communications with quantized double phase shifters," in *Proc. of IEEE ICASSP*, 2023, pp. 1–5.
- [11] D. Cong, S. Guo, S. Dang, and H. Zhang, "Vehicular behavior-aware beamforming design for integrated sensing and communication systems," *IEEE Trans. Intell. Transp. Syst.*, vol. 24, no. 6, pp. 5923–5935, 2023.
- [12] S. Ma, H. Sheng, R. Yang, H. Li, Y. Wu, C. Shen, N. Al-Dhahir, and S. Li, "Covert beamforming design for integrated radar sensing and communication systems," *IEEE Trans. Wireless Commun.*, vol. 22, no. 1, pp. 718–731, 2023.
- [13] A. Bazzi and M. Chafii, "Secure full duplex integrated sensing and communications," *IEEE Trans. Inf. Forensics Security*, vol. 19, pp. 2082–2097, 2024.
- [14] K. Dong, S. A. Vorobyov, H. Yu, and T. Taleb, "Beamforming design for integrated sensing, over-the-air computation, and communication in Internet of Robotic Things," *IEEE Internet Things J.*, vol. 11, no. 20, pp. 32478–32489, 2024.
- [15] L. F. Abanto-Leon, M. Hollick, B. Clerckx, and G. H. A. Sim, "Sequential parametric optimization for rate-splitting precoding in non-orthogonal unicast and multicast transmissions," in *Proc. of IEEE ICC*, 2022, pp. 3904–3910.
- [16] L. F. Abanto-Leon and G. H. A. Sim, "Fairness-aware hybrid precoding for mmwave NOMA unicast/multicast transmissions in industrial IoT," in *Proc. of IEEE ICC*, 2020, pp. 1–7.
- [17] A. M. Elbir, A. Celik, and A. M. Eltawil, "Hybrid beamforming for integrated sensing and communications with low resolution DACs," *IEEE Wireless Commun. Lett.*, pp. 1–5, 2024.
- [18] I. K. Jain, S. Mm, and D. Bharadia, "CommRad: Context-aware sensing-driven millimeter-wave networks," in *Proc. of ACM Sensys*, 2024, p. 633–646.
- [19] R. Zhao, T. Woodford, T. Wei, K. Qian, and X. Zhang, "M-Cube: A millimeter-wave massive MIMO software radio," in *Proc. of ACM MobiCom*, 2020.
- [20] Z. Xiao, S. Chen, and Y. Zeng, "Simultaneous multi-beam sweeping for mmWave massive MIMO integrated sensing and communication," *IEEE Trans. Veh. Technol.*, vol. 73, no. 6, pp. 8141–8152, 2024.
- [21] M. L. Rahman, P.-F. Cui, J. A. Zhang, X. Huang, Y. J. Guo, and Z. Lu, "Joint communication and radar sensing in 5G mobile network by compressive sensing," in *Proc. of ISCIT*, 2019, pp. 599–604.
- [22] L. Wang and L. F. Abanto-Leon, "Resource allocation for ISAC networks with application to target tracking," in *Proc. of IEEE GLOBECOM Workshops*, 2024, pp. 1–7.
- [23] R. Hersyandika, A. Sakhnini, Y. Miao, Q. Wang, and S. Pollin, "Guard Beams: Coverage enhancement of UE-centered ISAC via analog multi-beamforming," *IEEE Access*, vol. 12, pp. 163507–163523, 2024.
- [24] Y. Ding, V. Fusco, A. Shitvov, Y. Xiao, and H. Li, "Beam index modulation wireless communication with analog beamforming," *IEEE Trans. Veh. Technol.*, vol. 67, no. 7, pp. 6340–6354, 2018.
- [25] Z. Du, F. Liu, W. Yuan, C. Masouros, Z. Zhang, S. Xia, and G. Caire, "Integrated sensing and communications for V2I networks: Dynamic predictive beamforming for extended vehicle targets," *IEEE Trans. Wireless Commun.*, vol. 22, no. 6, pp. 3612–3627, 2023.
- [26] H. Zhang, T. Yang, X. Wu, Z. Guo, and B. Hu, "Robust beamforming design for UAV communications based on integrated sensing and communication," *J. Wireless Com. Network*, vol. 88, pp. 1–24, 2023.
- [27] Y. Karaçora, C. Chaccour, A. Sezgin, and W. Saad, "Event-based beam tracking with dynamic beamwidth adaptation in terahertz (THz) communications," *IEEE Trans. Commun.*, vol. 71, no. 10, pp. 6195–6210, 2023.
- [28] M. Feng, B. Akgun, I. Aykin, and M. Krunz, "Beamwidth optimization for 5G NR millimeter wave cellular networks: A multi-armed bandit approach," in *Proc. of IEEE ICC*, 2021, pp. 1–6.
- [29] H. Chung, J. Kang, H. Kim, Y. M. Park, and S. Kim, "Adaptive beamwidth control for mmWave beam tracking," *IEEE Commun. Lett.*, vol. 25, no. 1, pp. 137–141, 2021.
- [30] C. B. Barneto, T. Riihonen, S. D. Liyanaarachchi, M. Heino, N. González-Prelcic, and M. Valkama, "Beamformer design and optimization for joint communication and full-duplex sensing at mm-waves," *IEEE Trans. Commun.*, vol. 70, no. 12, pp. 8298–8312, 2022.
- [31] Z. Liu, S. Aditya, H. Li, and B. Clerckx, "Joint transmit and receive beamforming design in full-duplex integrated sensing and communications," *IEEE J. Sel. Areas Commun.*, vol. 41, no. 9, pp. 2907–2919, 2023.
- [32] X. Liu, Z.-H. Xu, L. Wang, W. Dong, and S. Xiao, "Cognitive dwell time allocation for distributed radar sensor networks tracking via cone programming," *IEEE Sensors J.*, vol. 20, no. 10, pp. 5092–5101, 2020.

- [33] H. Zhang, W. Liu, J. Yan, J. Shi, and Q. Zhang, "A fast solver for dwell time allocation in a phased array radar," *IEEE Trans. Veh. Technol.*, vol. 72, no. 8, pp. 10 345–10 356, 2023.
- [34] L. F. Abanto-Leon, M. Hollick, and G. H. Sim, "Hydrawave: Multi-group multicast hybrid precoding and low-latency scheduling for ubiquitous Industry 4.0 mmWave communications," in *Proc. of IEEE WoWMoM*, 2020, pp. 98–107.
- [35] V.-D. Nguyen, H. D. Tuan, T. Q. Duong, O.-S. Shin, and H. V. Poor, "Joint fractional time allocation and beamforming for downlink multiuser MISO systems," *IEEE Commun. Lett.*, vol. 21, no. 12, pp. 2650–2653, 2017.
- [36] D. Xu, Y. Xu, Z. Wei, S. Song, and D. W. Kwan Ng, "Sensing-enhanced secure communication: Joint time allocation and beamforming design," in *Proc. of WiOpt*, 2023, pp. 673–680.
- [37] G. Li, S. Wang, K. Ye, M. Wen, D. W. K. Ng, and M. Di Renzo, "Multi-point integrated sensing and communication: Fusion model and functionality selection," *IEEE Wireless Commun. Lett.*, vol. 11, no. 12, pp. 2660–2664, 2022.
- [38] C. Dou, N. Huang, Y. Wu, L. Qian, and T. Q. S. Quek, "Channel sharing aided integrated sensing and communication: An energy-efficient sensing scheduling approach," *IEEE Trans. Wireless Commun.*, vol. 23, no. 5, pp. 4802–4814, 2024.
- [39] L. Cazzella, M. Mizmizi, D. Tagliaferri, D. Badini, M. Matteucci, and U. Spagnolini, "Deep learning-based target-to-user association in integrated sensing and communication systems," *IEEE J. Sel. Topics Signal Process.*, vol. 18, no. 5, pp. 886–900, 2024.
- [40] L. F. Abanto-Leon and S. Maghsudi, "Optimal user and target scheduling, user-target pairing, and low-resolution phase-only beamforming for ISAC systems," *IEEE Trans. Veh. Technol.*, pp. 1–6, 2025.
- [41] H. Jia, X. Li, and L. Ma, "Physical layer security optimization with Cramér–Rao bound metric in ISAC systems under sensing-specific imperfect CSI model," *IEEE Trans. Veh. Technol.*, vol. 73, no. 5, pp. 6980–6992, 2024.
- [42] W. Lyu, S. Yang, Y. Xiu, X. Chen, Z. Zhang, C. Assi, and C. Yuen, "Dual-robust integrated sensing and communication: Beamforming under CSI imperfection and location uncertainty," *IEEE Wireless Commun. Lett.*, vol. 13, no. 11, pp. 3124–3128, 2024.
- [43] A. Khalili and R. Schober, "Advanced ISAC design: Movable antennas and accounting for dynamic RCS," in *Proc. of IEEE Globecom*, 2024, pp. 1–6.
- [44] A. Tang, S. Li, and X. Wang, "Self-interference-resistant IEEE 802.11ad-based joint communication and automotive radar design," *IEEE J. Sel. Topics Signal Process.*, vol. 15, no. 6, pp. 1484–1499, 2021.
- [45] Z. He, W. Xu, H. Shen, D. W. K. Ng, Y. C. Eldar, and X. You, "Full-duplex communication for ISAC: Joint beamforming and power optimization," *IEEE J. Sel. Areas Commun.*, vol. 41, no. 9, pp. 2920–2936, 2023.
- [46] Y. Huang, Y. Fang, X. Li, and J. Xu, "Coordinated power control for network integrated sensing and communication," *IEEE Trans. Veh. Technol.*, vol. 71, no. 12, pp. 13 361–13 365, 2022.
- [47] G. Desaulniers, J. Desrosiers, and M. M. Solomon, *Column generation*. Springer New York, NY, 2005.
- [48] G. Wolosinski, H. Tataria, and V. Fusco, "Closed form characterization of mutual coupling in uniform linear arrays," in *Proc. of EuCAP*, 2020, pp. 1–5.
- [49] Y. Pan, X. Xu, and A. Yang, "Joint estimation of DOA and mutual coupling via imposing an annihilation constraint," *Digit. Signal Process.*, vol. 130, p. 7, 2022.
- [50] J. Zhao, D. Gündüz, O. Simeone, and D. Gómez-Barquero, "Non-orthogonal unicast and broadcast transmission via joint beamforming and LDM in cellular networks," *IEEE Trans. Broadcast.*, vol. 66, no. 2, pp. 216–228, 2020.
- [51] Z. Ren, L. Qiu, J. Xu, and D. W. K. Ng, "Robust transmit beamforming for secure integrated sensing and communication," *IEEE Trans. Commun.*, vol. 71, no. 9, pp. 5549–5564, 2023.
- [52] D. Xu, Y. Sun, D. W. K. Ng, and R. Schober, "Multiuser MISO UAV communications in uncertain environments with no-fly zones: Robust trajectory and resource allocation design," *IEEE Trans. Commun.*, vol. 68, no. 5, pp. 3153–3172, 2020.
- [53] —, "Robust resource allocation for UAV systems with UAV jittering and user location uncertainty," in *Proc. of IEEE Globecom Workshops*, 2018, pp. 1–6.
- [54] F. Liu, Y.-F. Liu, A. Li, C. Masouros, and Y. C. Eldar, "Cramér–Rao bound optimization for joint radar-communication beamforming," *IEEE Trans. Signal Process.*, vol. 70, pp. 240–253, 2022.
- [55] M. I. Skolnik, *Introduction to radar systems*. McGraw-Hill, 2001.
- [56] M. A. Richards, *Fundamentals of radar signal processing*. McGraw-Hill, 2005.
- [57] C. Cao, J. Zhang, J. Meng, X. Zhang, and X. Mao, "Clutter suppression and target tracking by the low-rank representation for airborne maritime surveillance radar," *IEEE Access*, vol. 8, pp. 160 774–160 789, 2020.
- [58] S.-M. Kim, Y.-G. Lim, L. Dai, and C.-B. Chae, "Performance analysis of self-interference cancellation in full-duplex massive MIMO systems: Subtraction versus spatial suppression," *IEEE Trans. Wireless Commun.*, vol. 22, no. 1, pp. 642–657, 2023.
- [59] L. J. Rodriguez, N. H. Tran, and T. Le-Ngoc, "Optimal power allocation and capacity of full-duplex AF relaying under residual self-interference," *IEEE Wireless Commun. Lett.*, vol. 3, no. 2, pp. 233–236, 2014.
- [60] D. Liu, Y. Shen, S. Shao, Y. Tang, and Y. Gong, "On the analog self-interference cancellation for full-duplex communications with imperfect channel state information," *IEEE Access*, vol. 5, pp. 9277–9290, 2017.
- [61] Z. Wang, X. Mu, and Y. Liu, "Near-field integrated sensing and communications," *IEEE Commun. Lett.*, vol. 27, no. 8, pp. 2048–2052, 2023.
- [62] D. Tse and P. Viswanath, *Fundamentals of wireless communication*. Cambridge University Press, 2005.
- [63] Y. Cheng and M. Pesavento, "Joint discrete rate adaptation and downlink beamforming using mixed integer conic programming," *IEEE Trans. Signal Process.*, vol. 63, no. 7, pp. 1750–1764, 2015.
- [64] L. F. Abanto-Leon, A. Krishnamoorthy, A. Garcia-Saavedra, G. H. Sim, R. Schober, and M. Hollick, "Radio resource management design for RSMA: Optimization of beamforming, user admission, and discrete/continuous rates with imperfect SIC," *IEEE Trans. Mobile Comput.*, vol. 23, no. 12, pp. 11 498–11 518, 2024.
- [65] 3GPP, "Study on channel model for frequencies from 0.5 to 100 GHz," 3rd Generation Partnership Project (3GPP), Technical Report (TR) 38.901, 2020, version 16.1.0.
- [66] L. F. Abanto-Leon and S. Maghsudi, "Resilient full-duplex ISAC in the face of imperfect SI cancellation: Globally optimal timeslot allocation and beam selection," in *Proc. of European Wireless*, 2025.



radio resource management in 5G/6G wireless networks.



many, and a Senior Research Scientist with the Fraunhofer Heinrich-Hertz Institute. Her research interests include the intersection of network analysis and optimization, game theory, machine learning, and data science. She was the recipient several competitive fellowships, awards, and research grants from different institutes, including the German Research Foundation, German Ministry of Education and Research, and Japan Society for the Promotion of Science.

Luis F. Abanto-Leon received the M.Sc. degree in communications engineering from Tohoku University, Japan, in 2015, and the Ph.D. degree in computer science from Technische Universität Darmstadt, Germany, in 2023. Since March 2024, he has been a Postdoctoral Researcher with the Faculty of Electrical Engineering and Information Technology, Ruhr-Universität Bochum, Germany. His research expertise include optimization theory, signal processing, and machine learning, with a focus on algorithm design for

Setareh Maghsudi received the Ph.D. degree (summa cum laude) from the Technical University of Berlin, Berlin, Germany, in 2015. From 2015 to 2017, she was a Postdoctoral with the University of Manitoba, Winnipeg, MB, Canada, and Yale University, New Haven, CT, USA. From 2017 to 2023, she was an Assistant Professor with the Technical University of Berlin, Berlin, Germany, and Tübingen University, Tübingen, Germany. She is currently a full Professor with the Ruhr-University of Bochum, Bochum, Germany,

APPENDIX A: RELATED WORK

Table A.1 (see next page) provides a concise visual summary of the key distinctions between the problem addressed in this work and existing studies in the literature, clearly highlighting the substantial differences.

In particular, compared with prior work, our approach uniquely integrates timeslot allocation into the RRM design, enables adaptive beam control across multiple dimensions (direction, transmit/receive power, and beamwidth), incorporates functionality selection at the timeslot level, and allows for optimizable user-target pairing.

APPENDIX B: MAIN PARAMETERS

Table B.1 summarizes the most relevant parameters and variable used in the system model.

TABLE B.1: Parameters and variables

Parameters and Variables	Notation
Number of transmit antennas at the BS	N_{tx}
Number of receive antennas at the BS	N_{rx}
Number of transmit codewords at the BS	L_{tx}
Number of receive codewords at the BS	L_{rx}
Number of users	U
Number of targets	T
Finite horizon	S
Set indexing the transmit codewords	\mathcal{L}_{tx}
Set indexing the receive codewords	\mathcal{L}_{rx}
Set indexing the users	\mathcal{U}
Set indexing the targets	\mathcal{T}
Set indexing the timeslots	\mathcal{S}
Set of channel vectors with errors for U_u	\mathcal{H}_u
Set of angles of arrival with errors for T_t	Θ_t
Set of reflection coefficients with errors for T_t	Ψ_t
Communication channel between the BS and U_u	\mathbf{h}_u
Sensing channel between the BS and T_t	\mathbf{g}_t
Residual self-interference channel of the BS's transceiver	\mathbf{R}
Communication SNR threshold for U_u	$\Upsilon_{snr,u}$
Sensing SINR threshold for T_t	$\Lambda_{sint,t}$
Number of timeslots allocated to U_u	$S_{com,u}$
Number of timeslots allocated to T_t	$S_{sen,t}$
Communication noise power	σ_{com}^2
Sensing noise power	σ_{sen}^2
Timeslot duration	S_{dur}
Variable indicating whether S_s is used for communication	κ_s
Variable indicating whether S_s is used for sensing	ζ_s
Variable indicating whether S_s is used	γ_s
Variable indicating whether U_u is served in S_s	$\mu_{u,s}$
Variable indicating whether T_t is served in S_s	$\tau_{t,s}$
Variable indicating whether \mathbf{b}_b is used in S_s	$\chi_{b,s}$
Variable indicating whether c_c is used in S_s	$\rho_{c,s}$
Transmit beamformer in S_s	\mathbf{w}_s
Receive beamformer in S_s	\mathbf{v}_s

APPENDIX C: DETAILS ON PARAMETERS S AND \tilde{S}

Without considering pairing, the total number of timeslots required for communication is $\hat{S} = \sum_{u \in \mathcal{U}} S_{com,u}$ and the total number of timeslots required for sensing is $\check{S} = \sum_{t \in \mathcal{T}} S_{sen,t}$.

In the worst case, the BS requires up to $\tilde{S} = \hat{S} + \check{S}$ timeslots, which corresponds to independent timeslot allocation for users and targets without any pairing. In contrast, the minimum number of required timeslots is $\bar{S} = \max\{\hat{S}, \check{S}\}$ which is achieved when the maximum possible number of user-target pairs share the same timeslots.

Consequently, the finite scheduling horizon must satisfy $\bar{S} \leq S \leq \tilde{S}$. In practice, we intentionally choose $S \ll \tilde{S}$, since a smaller finite horizon naturally promotes user-target pairing and promotes timeslot sharing whenever feasible.

APPENDIX D: DETAILS ON USER-TARGET PAIRING

Constraints $C_1, C_2, C_5, C_6, C_7,$ and C_8 ensure one-to-one pairing between users and targets whenever feasible, as explained in the following.

For any timeslot S_s , constraints $C_1, C_2, C_6,$ and C_8 enforce $\sum_{u \in \mathcal{U}} \mu_{u,s} \in \{0, 1\}$ and $\sum_{t \in \mathcal{T}} \tau_{t,s} \in \{0, 1\}$. If either or both summations are zero, no pairing occurs in S_s since both sensing and communication must be feasible in a timeslot for pairing to be established. When both summations equal one, constraints C_5 and C_7 ensure that exactly one variable $\mu_{u,s}$ and one variable $\tau_{t,s}$ are equal to one. This implies that exactly one user and one target are served in S_s , establishing a one-to-one pairing between them.

Importantly, pairing may vary across timeslots, as the user and target requirements can differ. Importantly, pairing is not predetermined but rather optimized through RRM design, being established only when providing time or energy savings.

APPENDIX E: EXTENDED MODEL

From (5) and (6), we have the following relation

$$\mathbf{A}(\theta_t) = \frac{1}{\sqrt{N_{rx}N_{tx}}} e^{j\phi_{rx} \cos(\theta_t)} \left(e^{j\phi_{tx} \cos(\theta_t)} \right)^H \quad (\text{E.1})$$

Particularly, note that $e^{j\phi_{rx} \cos(\theta_t)} \left(e^{j\phi_{tx} \cos(\theta_t)} \right)^H = e^{j\phi_{rx} \cos(\theta_t)} \left(e^{-j\phi_{tx} \cos(\theta_t)} \right)^T = e^{j\phi_{rx} \cos(\theta_t)} e^{-j\phi_{tx}^T \cos(\theta_t)}$. To simplify the expression, we define $\Phi = \mathbf{1}^T \otimes \phi_{rx} - \mathbf{1} \otimes \phi_{tx}^T$, which allows us to express $\mathbf{A}(\theta_t)$ as $\mathbf{A}(\theta_t) = e^{j\Phi \cos(\theta_t)}$. Taking the first-order Taylor expansion of $\mathbf{A}(\theta_t)$ around $\bar{\theta}_t$, results in

$$\mathbf{A}(\theta_t) \approx \mathbf{A}(\bar{\theta}_t) + \nabla_{\theta_t} \mathbf{A}(\theta_t) \Big|_{\theta_t = \bar{\theta}_t} (\theta_t - \bar{\theta}_t), \quad (\text{E.2})$$

where $\nabla_{\theta_t} \mathbf{A}(\theta_t) = \mathbf{A}(\theta_t) \circ \mathbf{E}(\theta_t)$ and $\mathbf{E}(\theta_t) = -j\Phi \sin(\theta_t)$. Noting that $\Delta\theta_t = \theta_t - \bar{\theta}_t$ and defining $\tilde{\mathbf{A}}(\theta_t) = \mathbf{A}(\theta_t) \circ \mathbf{E}(\theta_t)$ leads to

$$\mathbf{A}(\theta_t) \approx \mathbf{A}(\bar{\theta}_t) + \tilde{\mathbf{A}}(\bar{\theta}_t) \Delta\theta_t, \quad (\text{E.3})$$

which is the same expression shown in (8).

APPENDIX F: WEIGHT DESIGN

To ensure cohesive timeslot allocation, it is essential to prioritize consecutive timeslots while giving higher precedence to the earliest available timeslots. Using mathematical induction, we derive a simple weighting policy based on an arithmetic sequence.

Given S timeslots, we first assume that the RRM task is fulfilled using a single timeslot, i.e., $\sum_{s \in \mathcal{S}} \gamma_s = 1$. The optimal allocation satisfying the cohesiveness requirement is given by $\gamma_1 = 1$ and $\gamma_s = 0, \forall s \in \mathcal{S} \setminus \{1\}$, yielding $\omega_1 < \omega_{i_1}, \forall i_1 \in \{2, 3, \dots, S\}$.

Next, we consider the case where the RRM task is fulfilled using two timeslots, i.e., $\sum_{s \in \mathcal{S}} \gamma_s = 2$. The most cohesive allocation is $\gamma_1 = \gamma_2 = 1$ and $\gamma_s = 0, \forall s \in \mathcal{S} \setminus \{1, 2\}$. This implies that $\omega_1 + \omega_2 < \omega_{i_1} + \omega_{i_2}$ for all pairs $(i_1, i_2) \neq (1, 2)$. To tighten this inequality, we assume $\omega_1 = \omega_{i_1}$, leading to $\omega_2 < \omega_{i_2}, \forall i_2 \in \{3, 4, \dots, S\}$.

Following the induction process, we generalize to the case where all but one timeslot is allocated, i.e., $\sum_{s \in \mathcal{S}} \gamma_s =$

TABLE A.1: Categorization of most relevant related work.

Works	System	Integration level	Time allocation	Beamforming type	Beam adaptation				Functionality selection	User-target pairing	Imperfect information				Resource economy
					Direction	Power	Beamwidth	Side			CSI	AOD	RC	RSI	
[20], [21]	ISAC	Single waveform	N/A	Analog	Adaptive & discrete	Fixed	Fixed	Tx & Rx	N/A	Fixed	✗	✗	✗	✗	None
[22]	ISAC	Single waveform	Discrete multi-slot	Analog	Adaptive & discrete	Adaptive & continuous	Fixed	Tx & Rx	N/A	Fixed	✗	✗	✗	✗	None
[23], [24]	ISAC	Single waveform	N/A	Analog	Adaptive & discrete	Adaptive & continuous	Fixed	Tx & Rx	N/A	Fixed	✗	✗	✗	✗	None
[27]–[29]	Comm.	N/A	N/A	Analog	Fixed	Fixed	Adaptive & continuous	Tx & Rx	N/A	N/A	✗	✗	✗	✗	None
[25], [26]	ISAC	Single waveform	N/A	Analog	Fixed	Fixed	Adaptive & continuous	Tx & Rx	N/A	Fixed	✗	✗	✗	✗	None
[32], [33]	Sens.	N/A	Continuous	Digital	Fixed	Adaptive & continuous	Fixed	Tx & Rx	N/A	N/A	✗	✗	✗	✗	None
[34], [35]	Comm.	N/A	Continuous	Digital	Beamformer design not subject to practical considerations			Tx	N/A	N/A	✗	✗	✗	✗	Time
[36]	ISAC	Independent waveforms	Continuous	Digital	Beamformer design not subject to practical considerations			Tx	N/A	Fixed	✗	✓	✓	✗	None
[37]	ISAC	Single waveform	N/A	Digital	Fixed	Adaptive & continuous	Fixed	Tx & Rx	One at a time	Fixed	✗	✗	✗	✗	None
[8]	ISAC	Single waveform	N/A	Analog	Adaptive & discrete	Fixed	Fixed	Tx & Rx	One is prioritized	Fixed	✗	✓	✗	✗	None
[38]	ISAC	Independent waveforms	N/A	Digital	Beamformer design not subject to practical considerations			Tx & Rx	N/A	Dynamic	✗	✗	✗	✗	None
[39]	ISAC	Single waveform	N/A	Hybrid	Beamformer design not subject to practical considerations			Tx & Rx	N/A	Dynamic	✗	✗	✗	✗	None
[40]	ISAC	Single waveform	N/A	Analog	Adaptive & continuous	Fixed	Adaptive & continuous	Tx & Rx	N/A	Dynamic	✗	✗	✗	✗	None
[45]	ISAC	Independent waveforms	N/A	Digital	Beamformer design not subject to practical considerations			Tx & Rx	N/A	N/A	✗	✗	✗	✗	Energy
[46]	ISAC	Single waveform	N/A	N/A	Power control involving multiple single-antenna BSs			Tx	N/A	Fixed	✗	✗	✗	✗	Energy
[41]	ISAC	Independent waveforms	N/A	Digital	Beamformer design not subject to practical considerations			Tx & Rx	N/A	N/A	✗	✗	✗	✗	None
[42]	ISAC	Independent waveforms	N/A	Digital	Beamformer design not subject to practical considerations			Tx	N/A	N/A	✓	✓	✗	✗	None
[43]	ISAC	Independent waveforms	N/A	Digital	Beamformer design not subject to practical considerations			Tx & Rx	N/A	N/A	✗	✗	✓	✗	Energy
[44]	ISAC	Single waveform	N/A	Analog	Fixed	Fixed	Fixed	Tx & Rx	N/A	Fixed	✗	✗	✗	✓	None
Proposed	ISAC	Single waveform	Discrete multi-slot	Analog	Adaptive & discrete	Adaptive & discrete	Adaptive & discrete	Tx & Rx	None, one, or two	Dynamic	✓	✓	✓	✓	Energy & time

$S - 1$. The optimal allocation is $\gamma_1 = \gamma_2 = \dots = \gamma_{S-1} = 1$ and $\gamma_S = 0$, resulting in $\omega_1 + \omega_2 + \dots + \omega_{S-1} < \omega_{i_1} + \omega_{i_2} + \dots + \omega_{i_{S-1}}$, $\forall (i_1, i_2, \dots, i_{S-1}) \neq (1, 2, \dots, S-1)$. To refine this inequality, we assume $\omega_s = \omega_{i_s}, \forall s \in \{1, 2, \dots, S-2\}$, yielding $\omega_{S-1} < \omega_S$.

Collecting all results, we derive the general rule that achieving cohesive timeslot allocation requires satisfying $\omega_s < \omega_{s+1}$. To generalize this rule in a structured manner, we adopt an arithmetic sequence, defined as $\omega_s = \Delta_0 + (s - 1) \cdot \Delta_\omega$, where Δ_0 is the initial value and Δ_ω represents the increment.

APPENDIX G: PROOF TO PROPOSITION 1

Leveraging the binary nature of κ_s and ζ_s , we apply propositional calculus to eliminate the binding logical operation between these variables. Thus, we introduce the substitutions $a = \gamma_s$, $b = \kappa_s$, and $\zeta_s = c$ to simplify notation. The steps involved in the decoupling process are shown below.

$$\begin{aligned}
 a &\leftrightarrow b \vee c, \\
 &\equiv (a \rightarrow (b \vee c)) \wedge ((b \vee c) \rightarrow a), \\
 &\equiv (\neg a \vee (b \vee c)) \wedge (\neg (b \vee c) \vee a), \\
 &\equiv (\neg a \vee b \vee c) \wedge ((\neg b \wedge \neg c) \vee a), \\
 &\equiv (\neg a \vee b \vee c) \wedge ((\neg b \vee a) \wedge (\neg c \vee a)),
 \end{aligned}$$

$$\begin{aligned}
 &\equiv (\neg a \vee b \vee c) \wedge (\neg b \vee a) \wedge (\neg c \vee a), \\
 &\equiv ((1 - a) + b + c \geq 1) \wedge ((1 - b) + a \geq 1) \\
 &\quad \wedge ((1 - c) + a \geq 1), \\
 &\equiv (a \leq b + c) \wedge (a \geq b) \wedge (a \geq c).
 \end{aligned}$$

We know that a must be binary since it results from a logical operation. Yet, this condition is not always enforced by the inequalities above, particularly, when $b = c = 1$. While adding constraint $a \in \{0, 1\}$ would prevent this issue, an alternative approach is to define a within a continuous set, as specified by constraint $a \leq 1$. This choice maintains the integrality of a while reducing the number of binary variables, thereby lowering the complexity associated with binary variable search.

Hence, from the results above, constraint C_3 can be equivalently expressed as the intersection of $D_1 : \gamma_s \leq \kappa_s + \zeta_s, \forall s \in \mathcal{S}$, $D_2 : \gamma_s \geq \kappa_s, \forall s \in \mathcal{S}$, $D_3 : \gamma_s \geq \zeta_s, \forall s \in \mathcal{S}$, and $D_4 : \gamma_s \leq 1, \forall s \in \mathcal{S}$.

APPENDIX H: PROOF TO PROPOSITION 2

Using the definitions in (4), and substituting \mathbf{w}_s , as defined in C_{11} , into C_{16} leads to constraint $E_{\text{aux},1} : \min_{\mathbf{h}_u \in \mathcal{H}_u} |\sum_{b \in \mathcal{L}_{\text{tx}}} \mathbf{h}_u^H \mathbf{Z}_{\text{tx}} \mathbf{b}_b \cdot \chi_{b,s} \cdot \mu_{u,s}|^2 \geq \Upsilon_{\text{snr},u} \cdot \sigma_{\text{com}}^2$.

$\mu_{u,s}, \forall u \in \mathcal{U}, s \in \mathcal{S}$. By analyzing $\mu_{u,s}$ in $E_{\text{aux},1}$, we distinguish two distinct cases, shown in the following.

Case ① \Rightarrow When $\mu_{u,s} = 0$, the inequality is tight as both sides collapse to zero.

Case ② \Rightarrow When $\mu_{u,s} = 1$, the inequality collapses to $\min_{\mathbf{h}_u \in \mathcal{H}_u} \left| \sum_{b \in \mathcal{L}_{\text{tx}}} \mathbf{h}_u^H \mathbf{Z}_{\text{tx}} \mathbf{b}_b \cdot \chi_{b,s} \right|^2 \geq \Upsilon_{\text{snr},u} \cdot \sigma_{\text{com}}^2, \forall u \in \mathcal{U}, s \in \mathcal{S}$.

The two cases above can be combined into a single constraint, leading to $E_{\text{aux},2}$: $\min_{\mathbf{h}_u \in \mathcal{H}_u} \left| \sum_{b \in \mathcal{L}_{\text{tx}}} \mathbf{h}_u^H \mathbf{Z}_{\text{tx}} \mathbf{b}_b \cdot \chi_{b,s} \right|^2 \geq \Upsilon_{\text{snr},u} \cdot \sigma_{\text{com}}^2 \cdot \mu_{u,s}, \forall u \in \mathcal{U}, s \in \mathcal{S}$. Note that the LHS of $E_{\text{aux},2}$ is not necessarily zero when $\mu_{u,s} = 0$. This is because $\mu_{u,s} = 0$ only indicates that U_u is not served in S_s , but it does not preclude S_s from being used to serve another $U_{u'}$, where $u' \neq u$. To improve the tractability of $E_{\text{aux},2}$, where variables $\chi_{b,s}$ are coupled both additively and multiplicatively in its LHS, we apply Jensen's inequality to uncover useful relationships.

Considering arbitrary U_u and S_s , and applying Jensen's inequality to the absolute value term in $E_{\text{aux},2}$, we obtain $E_{\text{aux},3}$: $\left| \sum_{b \in \mathcal{L}_{\text{tx}}} \mathbf{h}_u^H \mathbf{Z}_{\text{tx}} \mathbf{b}_b \cdot \chi_{b,s} \right| \leq \sum_{b \in \mathcal{L}_{\text{tx}}} \left| \mathbf{h}_u^H \mathbf{Z}_{\text{tx}} \mathbf{b}_b \cdot \chi_{b,s} \right|$. Let \mathbf{b}_i denote the beamformer serving U_u in S_s . Since only one transmit beamformer can be selected per active timeslot (as enforced by constraint C_{10}), we have $\chi_{i,s} = 1$ and $\chi_{b,s} = 0, \forall b \in \mathcal{L}_{\text{tx}} \setminus \{i\}$. With this observation, $E_{\text{aux},3}$ simplifies to the equivalent form $E_{\text{aux},4}$: $\left| \sum_{b \neq i} \mathbf{h}_u^H \mathbf{Z}_{\text{tx}} \mathbf{b}_b \cdot \chi_{b,s} + \mathbf{h}_u^H \mathbf{Z}_{\text{tx}} \mathbf{b}_i \cdot \chi_{i,s} \right| \leq \sum_{b \neq i} \left| \mathbf{h}_u^H \mathbf{Z}_{\text{tx}} \mathbf{b}_b \cdot \chi_{b,s} \right| + \left| \mathbf{h}_u^H \mathbf{Z}_{\text{tx}} \mathbf{b}_i \cdot \chi_{i,s} \right|$. Exponentiating both sides yields $E_{\text{aux},5}$: $\left| \sum_{b \neq i} \mathbf{h}_u^H \mathbf{Z}_{\text{tx}} \mathbf{b}_b \cdot \chi_{b,s} + \mathbf{h}_u^H \mathbf{Z}_{\text{tx}} \mathbf{b}_i \cdot \chi_{i,s} \right|^2 \leq \left(\sum_{b \neq i} \left| \mathbf{h}_u^H \mathbf{Z}_{\text{tx}} \mathbf{b}_b \cdot \chi_{b,s} \right| \right)^2 + \left| \mathbf{h}_u^H \mathbf{Z}_{\text{tx}} \mathbf{b}_i \cdot \chi_{i,s} \right|^2 + 2 \left(\sum_{b \neq i} \left| \mathbf{h}_u^H \mathbf{Z}_{\text{tx}} \mathbf{b}_b \cdot \chi_{b,s} \right| \right) \left| \mathbf{h}_u^H \mathbf{Z}_{\text{tx}} \mathbf{b}_i \cdot \chi_{i,s} \right|$. Note that the terms under the summations are zero, which makes $E_{\text{aux},5}$ hold at the equality, i.e., $\left| \sum_{b \in \mathcal{L}_{\text{tx}}} \mathbf{h}_u^H \mathbf{Z}_{\text{tx}} \mathbf{b}_b \cdot \chi_{b,s} \right|^2 = \sum_{b \in \mathcal{L}_{\text{tx}}} \left| \mathbf{h}_u^H \mathbf{Z}_{\text{tx}} \mathbf{b}_b \cdot \chi_{b,s} \right|^2$. This means that Jensen's inequality is tight when applied to $E_{\text{aux},2}$, allowing us to equivalently express $E_{\text{aux},2}$ as $E_{\text{aux},6}$: $\min_{\mathbf{h}_u \in \mathcal{H}_u} \sum_{b \in \mathcal{L}_{\text{tx}}} \left| \mathbf{h}_u^H \mathbf{Z}_{\text{tx}} \mathbf{b}_b \cdot \chi_{b,s} \right|^2 \geq \Upsilon_{\text{snr},u} \cdot \sigma_{\text{com}}^2 \cdot \mu_{u,s}, \forall u \in \mathcal{U}, s \in \mathcal{S}$. Note that extracting the summation from the quadratic term leads to an expression with simplified structure.

Although $E_{\text{aux},6}$ is more tractable than C_{16} , it still contains an infinite number of constraints due to all possible channels for U_u , as defined by C_{15} . Thus, we let $E_{\text{aux},6}$ absorb C_{15} , leading to $E_{\text{aux},7}$: $\min_{\|\Delta \mathbf{h}_u\|_2^2 \leq \epsilon_{\text{CSI}}} \sum_{b \in \mathcal{L}_{\text{tx}}} \frac{1}{\sigma_{\text{com}}^2} \left| (\bar{\mathbf{h}}_u^H + \Delta \mathbf{h}_u^H) \mathbf{Z}_{\text{tx}} \mathbf{b}_b \right|^2 \chi_{b,s} - \Upsilon_{\text{snr},u} \cdot \mu_{u,s} \geq 0, \forall u \in \mathcal{U}, s \in \mathcal{S}$, where $\chi_{b,s}$ has been factored out of the absolute value since $\chi_{b,s}^2 = \chi_{b,s}$. In particular, $E_{\text{aux},7}$ can be split into constraints $E_{\text{aux},8}$ and $E_{\text{aux},9}$, defined as follows: $E_{\text{aux},8}$: $\Delta \mathbf{h}_u^H \Delta \mathbf{h}_u - \epsilon_{\text{CSI}}^2 \leq 0, \forall u \in \mathcal{U}$, and $E_{\text{aux},9}$: $\Delta \mathbf{h}_u^H \mathbf{L}_s \Delta \mathbf{h}_u + \mathbf{h}_u^H \mathbf{L}_s \Delta \mathbf{h}_u + \Delta \mathbf{h}_u^H \mathbf{L}_s \bar{\mathbf{h}}_u + \bar{\mathbf{h}}_u^H \mathbf{L}_s \bar{\mathbf{h}}_u + \Upsilon_{\text{snr},u} \cdot \mu_{u,s} \leq 0, \forall u \in \mathcal{U}, s \in \mathcal{S}$, where $\mathbf{L}_s = -\sum_{b \in \mathcal{L}_{\text{tx}}} \frac{1}{\sigma_{\text{com}}^2} \mathbf{Z}_{\text{tx}} \mathbf{b}_b \mathbf{b}_b^H \mathbf{Z}_{\text{tx}}^H \chi_{b,s}$.

We apply **Lemma 2** to $E_{\text{aux},8}$ and $E_{\text{aux},9}$, leading to

constraints E_1 and E_2 , shown below,

$$E_1 : \begin{bmatrix} \mathbf{E}_{u,s}^a & \mathbf{e}_{u,s}^b \\ \mathbf{e}_{u,s}^c & e_{u,s}^d \end{bmatrix} \succcurlyeq \mathbf{0}, \forall u \in \mathcal{U}, s \in \mathcal{S},$$

$$E_2 : \alpha_u \geq 0, \forall u \in \mathcal{U},$$

where $\mathbf{E}_{u,s}^a = \alpha_u \mathbf{I} - \mathbf{L}_s$, $\mathbf{e}_{u,s}^b = -\mathbf{L}_s \bar{\mathbf{h}}_u$, $\mathbf{e}_{u,s}^c = -\bar{\mathbf{h}}_u^H \mathbf{L}_s$, $e_{u,s}^d = -\alpha_u \cdot \epsilon_{\text{CSI}}^2 - \bar{\mathbf{h}}_u^H \mathbf{L}_s \bar{\mathbf{h}}_u - \Upsilon_{\text{snr},u} \cdot \mu_{u,s}$, and α_u are newly introduced auxiliary variables needed by the *S-Procedure*.

APPENDIX I: PROOF TO PROPOSITION 3

The numerator and denominator of $\text{SINR}_{\text{sen}}^{t,s}$, as defined in (12), exhibit couplings between \mathbf{w}_s , \mathbf{v}_s , and $\tau_{t,s}$. By substituting the definitions of \mathbf{w}_s and \mathbf{v}_s , as specified in C_{11} and C_{14} , into C_{21} , we obtain constraint $F_{\text{aux},1}$: $\min_{\psi_t \in \Psi_t} \min_{\theta_t \in \Theta_t} \min_{\mathbf{R} \in \mathcal{R}} \frac{\left| \sum_{c \in \mathcal{L}_{\text{rx}}} \sum_{b \in \mathcal{L}_{\text{tx}}} \mathbf{c}_c^H \mathbf{Z}_{\text{rx}}^H \mathbf{G}_t \mathbf{Z}_{\text{tx}} \mathbf{b}_b \cdot \chi_{b,s} \cdot \rho_{c,s} \cdot \tau_{t,s} \right|^2}{\left| \sum_{c \in \mathcal{L}_{\text{rx}}} \sum_{b \in \mathcal{L}_{\text{tx}}} \mathbf{c}_c^H \mathbf{Z}_{\text{rx}}^H \mathbf{R} \mathbf{Z}_{\text{tx}} \mathbf{b}_b \cdot \chi_{b,s} \cdot \rho_{c,s} \cdot \tau_{t,s} \right|^2 + \sigma_{\text{sen}}^2 \sum_{c \in \mathcal{L}_{\text{rx}}} \|\mathbf{Z}_{\text{rx}} \mathbf{c}_c\|_2^2 \rho_{c,s}} \geq \Lambda_{\text{snr},t} \cdot \tau_{t,s}, \forall t \in \mathcal{T}, s \in \mathcal{S}$, revealing a triple coupling between $\chi_{b,s}$, $\rho_{c,s}$, and $\tau_{t,s}$, complicating tractability⁶.

Thus, we introduce new variables $\pi_{b,c,t,s}$, defined in constraint $F_{\text{aux},2}$: $\pi_{b,c,t,s} = \chi_{b,s} \cdot \rho_{c,s} \cdot \tau_{t,s}, \forall b \in \mathcal{L}_{\text{tx}}, c \in \mathcal{L}_{\text{rx}}, t \in \mathcal{T}, s \in \mathcal{S}$, and use propositional calculus to get rid of the coupling between $\chi_{b,s}$, $\rho_{c,s}$, and $\tau_{t,s}$. This process results in constraints F_1, F_2, F_3 , and F_4 , which are derived as shown at the top of the next page.

Additionally, note that variables $\pi_{b,c,t,s}$ must be binary, which is not always enforced by F_1, F_2, F_3 , and F_4 . While we could explicitly define $\pi_{b,c,t,s}$ as binary, we instead define these variables within a continuous closed set, as specified in constraint F_5 : $\pi_{b,c,t,s} \in [0, 1], \forall b \in \mathcal{L}_{\text{tx}}, c \in \mathcal{L}_{\text{rx}}, t \in \mathcal{T}, s \in \mathcal{S}$. This formulation is valid because the integrality of $\pi_{b,c,t,s}$ is inherently preserved, given that the resulting inequalities intersect only at 0 or 1, thereby reducing the number of explicitly defined binary variables. Substituting $\pi_{b,c,t,s}$ into $F_{\text{aux},1}$ leads to F_6 : $\min_{\psi_t \in \Psi_t} \min_{\theta_t \in \Theta_t} \min_{\mathbf{R} \in \mathcal{R}} \frac{\left| \sum_{c \in \mathcal{L}_{\text{rx}}} \sum_{b \in \mathcal{L}_{\text{tx}}} \mathbf{c}_c^H \mathbf{Z}_{\text{rx}}^H \mathbf{G}_t \mathbf{Z}_{\text{tx}} \mathbf{b}_b \cdot \pi_{b,c,t,s} \right|^2}{\left| \sum_{c \in \mathcal{L}_{\text{rx}}} \sum_{b \in \mathcal{L}_{\text{tx}}} \mathbf{c}_c^H \mathbf{Z}_{\text{rx}}^H \mathbf{R} \mathbf{Z}_{\text{tx}} \mathbf{b}_b \cdot \pi_{b,c,t,s} \right|^2 + \sigma_{\text{sen}}^2 \sum_{c \in \mathcal{L}_{\text{rx}}} \|\mathbf{Z}_{\text{rx}} \mathbf{c}_c\|_2^2 \rho_{c,s}} \geq \Lambda_{\text{snr},t} \cdot \tau_{t,s}, \forall t \in \mathcal{T}, s \in \mathcal{S}$. As a result, C_{11}, C_{14} , and C_{21} are equivalently recast as the intersection of F_1, F_2, F_3, F_4, F_5 , and F_6 .

APPENDIX J: PROOF TO PROPOSITION 4

By leveraging (5), we equivalently express F_6 as constraint $G_{\text{aux},1}$: $\min_{\psi_t \in \Psi_t} |\psi_t|^2 \left\{ \min_{\theta_t \in \Theta_t} \min_{\mathbf{R} \in \mathcal{R}} \frac{\left| \sum_{c \in \mathcal{L}_{\text{rx}}} \sum_{b \in \mathcal{L}_{\text{tx}}} \mathbf{c}_c^H \mathbf{Z}_{\text{rx}}^H \mathbf{A}(\theta_t) \mathbf{Z}_{\text{tx}} \mathbf{b}_b \cdot \pi_{b,c,t,s} \right|^2}{\left| \sum_{c \in \mathcal{L}_{\text{rx}}} \sum_{b \in \mathcal{L}_{\text{tx}}} \mathbf{c}_c^H \mathbf{Z}_{\text{rx}}^H \mathbf{R} \mathbf{Z}_{\text{tx}} \mathbf{b}_b \cdot \pi_{b,c,t,s} \right|^2 + \sigma_{\text{sen}}^2 \sum_{c \in \mathcal{L}_{\text{rx}}} \|\mathbf{Z}_{\text{rx}} \mathbf{c}_c\|_2^2 \rho_{c,s}} \right\} \geq \Lambda_{\text{snr},t} \cdot \tau_{t,s}, \forall t \in \mathcal{T}, s \in \mathcal{S}$, since $|\psi_t|^2$ depends only on t , and can therefore be repositioned within the expression. Further manipulating $G_{\text{aux},1}$ leads to $G_{\text{aux},2}$: $\min_{\theta_t \in \Theta_t} \min_{\mathbf{R} \in \mathcal{R}} \frac{\left| \sum_{c \in \mathcal{L}_{\text{rx}}} \sum_{b \in \mathcal{L}_{\text{tx}}} \mathbf{c}_c^H \mathbf{Z}_{\text{rx}}^H \mathbf{A}(\theta_t) \mathbf{Z}_{\text{tx}} \mathbf{b}_b \cdot \pi_{b,c,t,s} \right|^2}{\left| \sum_{c \in \mathcal{L}_{\text{rx}}} \sum_{b \in \mathcal{L}_{\text{tx}}} \mathbf{c}_c^H \mathbf{Z}_{\text{rx}}^H \mathbf{R} \mathbf{Z}_{\text{tx}} \mathbf{b}_b \cdot \pi_{b,c,t,s} \right|^2 + \sigma_{\text{sen}}^2 \sum_{c \in \mathcal{L}_{\text{rx}}} \|\mathbf{Z}_{\text{rx}} \mathbf{c}_c\|_2^2 \rho_{c,s}} \geq \frac{\Lambda_{\text{snr},t}}{\min_{\psi_t \in \Psi_t} |\psi_t|^2} \cdot \tau_{t,s}, \forall t \in \mathcal{T}, s \in \mathcal{S}$.

6. The noise term in the denominator, expressed originally as $\sigma_{\text{sen}}^2 \|\mathbf{v}_s\|_2^2$, can be equivalently recast as $\sigma_{\text{sen}}^2 \sum_{c \in \mathcal{L}_{\text{rx}}} \|\mathbf{Z}_{\text{rx}} \mathbf{c}_c\|_2^2 \rho_{c,s}$. Further elaboration on the transformation of this quadratic term can be found in **Appendix N**.

$$\begin{aligned}
 & \pi_{b,c,t,s} \leftrightarrow \chi_{b,s} \cdot \rho_{c,s} \cdot \tau_{t,s}, \forall b \in \mathcal{L}_{\text{tx}}, c \in \mathcal{L}_{\text{rx}}, t \in \mathcal{T}, s \in \mathcal{S}, \\
 & \equiv (\pi_{b,c,t,s} \rightarrow (\chi_{b,s} \wedge \rho_{c,s} \wedge \tau_{t,s})) \wedge ((\chi_{b,s} \wedge \rho_{c,s} \wedge \tau_{t,s}) \rightarrow \pi_{b,c,t,s}), \forall b \in \mathcal{L}_{\text{tx}}, c \in \mathcal{L}_{\text{rx}}, t \in \mathcal{T}, s \in \mathcal{S}, \\
 & \equiv (\neg \pi_{b,c,t,s} \vee (\chi_{b,s} \wedge \rho_{c,s} \wedge \tau_{t,s})) \wedge (\neg (\chi_{b,s} \wedge \rho_{c,s} \wedge \tau_{t,s}) \vee \pi_{b,c,t,s}), \forall b \in \mathcal{L}_{\text{tx}}, c \in \mathcal{L}_{\text{rx}}, t \in \mathcal{T}, s \in \mathcal{S}, \\
 & \equiv ((\neg \pi_{b,c,t,s} \vee \chi_{b,s}) \wedge (\neg \pi_{b,c,t,s} \vee \rho_{c,s})) \wedge (\neg \pi_{b,c,t,s} \vee \tau_{t,s}) \wedge ((\neg \chi_{b,s} \vee \neg \rho_{c,s} \vee \neg \tau_{t,s}) \vee \pi_{b,c,t,s}), \forall b \in \mathcal{L}_{\text{tx}}, c \in \mathcal{L}_{\text{rx}}, t \in \mathcal{T}, s \in \mathcal{S}, \\
 & \equiv ((1 - \pi_{b,c,t,s}) + \chi_{b,s} \geq 1) \wedge ((1 - \pi_{b,c,t,s}) + \rho_{c,s} \geq 1) \wedge ((1 - \pi_{b,c,t,s}) + \tau_{t,s} \geq 1) \wedge \\
 & \quad ((1 - \chi_{b,s}) + (1 - \rho_{c,s}) + (1 - \tau_{t,s}) + \pi_{b,c,t,s} \geq 1), \forall b \in \mathcal{L}_{\text{tx}}, c \in \mathcal{L}_{\text{rx}}, t \in \mathcal{T}, s \in \mathcal{S}, \\
 & \equiv \underbrace{(\pi_{b,c,t,s} \leq \chi_{b,s})}_{F_1} \wedge \underbrace{(\pi_{b,c,t,s} \leq \rho_{c,s})}_{F_2} \wedge \underbrace{(\pi_{b,c,t,s} \leq \tau_{t,s})}_{F_3} \wedge \underbrace{(2 + \pi_{b,c,t,s} \geq \chi_{b,s} + \rho_{c,s} + \tau_{t,s})}_{F_4}, \forall b \in \mathcal{L}_{\text{tx}}, c \in \mathcal{L}_{\text{rx}}, t \in \mathcal{T}, s \in \mathcal{S}.
 \end{aligned}$$

To ensure that the sensing performance is met even under the worst-case RC, we derive the corresponding worst-case SINR threshold by analyzing the right-hand-side (RHS) of $G_{\text{aux},2}$. Particularly, the worst-case sensing SINR threshold occurs when the denominator of the RHS of $G_{\text{aux},2}$ is minimum because it maximizes the ratio $\frac{\Lambda_{\text{sinr},t}}{\min_{\psi_t \in \Psi_t} |\psi_t|^2}$, thereby imposing a more demanding constraint. Hence, let us consider $G_{\text{aux},3} : \min_{\psi_t \in \Psi_t} |\psi_t|^2$, which is equivalent to $G_{\text{aux},4} : \min_{|\Delta\psi_t|^2 \leq \epsilon_{\text{RC}}^2} |\bar{\psi}_t + \Delta\psi_t|^2$ upon letting it absorb C_{19} .

Note that the quadratic term in $G_{\text{aux},4}$ reaches its minimum when the unknown error $\Delta\psi_t$ is aligned with the known value $\bar{\psi}_t$ but in opposite sense and has maximum power ϵ_{RC}^2 , i.e., $\Delta\psi_t = -\frac{\bar{\psi}_t}{|\bar{\psi}_t|} \epsilon_{\text{RC}}$. Substituting this expression into $G_{\text{aux},4}$ yields the worst-case sensing SINR threshold, denoted as $\bar{\Lambda}_{\text{sinr},t} = \frac{\Lambda_{\text{sinr},t}}{(|\bar{\psi}_t| - \epsilon_{\text{RC}})^2}$.

As a result, we can equivalently recast F_6 and C_{19} as $G_1 : \min_{\theta_t \in \Theta_t} \min_{\mathbf{R} \in \mathcal{R}} \frac{|\sum_{c \in \mathcal{L}_{\text{rx}}} \sum_{b \in \mathcal{L}_{\text{tx}}} \mathbf{c}_c^H \mathbf{Z}_{\text{rx}}^H \mathbf{A}(\theta_t) \mathbf{Z}_{\text{tx}} \mathbf{b}_b \cdot \pi_{b,c,t,s}|^2}{|\sum_{c \in \mathcal{L}_{\text{rx}}} \sum_{b \in \mathcal{L}_{\text{tx}}} \mathbf{c}_c^H \mathbf{Z}_{\text{rx}}^H \mathbf{R} \mathbf{Z}_{\text{tx}} \mathbf{b}_b \cdot \pi_{b,c,t,s}|^2 + \sigma_{\text{sen}}^2 \sum_{c \in \mathcal{L}_{\text{rx}}} \|\mathbf{Z}_{\text{rx}} \mathbf{c}_c\|_2^2 \rho_{c,s}} \geq \bar{\Lambda}_{\text{sinr},t} \cdot \tau_{t,s}, \forall t \in \mathcal{T}, s \in \mathcal{S}$.

APPENDIX K: PROOF TO PROPOSITION 5

Since AOD errors appear only in the numerator and RSI errors only in the denominator, we can equivalently express G_1 as $H_{\text{aux},1} : \frac{\min_{\theta_t \in \Theta_t} |\sum_{c \in \mathcal{L}_{\text{rx}}} \sum_{b \in \mathcal{L}_{\text{tx}}} \mathbf{c}_c^H \mathbf{Z}_{\text{rx}}^H \mathbf{A}(\theta_t) \mathbf{Z}_{\text{tx}} \mathbf{b}_b \cdot \pi_{b,c,t,s}|^2}{\max_{\mathbf{R} \in \mathcal{R}} |\sum_{c \in \mathcal{L}_{\text{rx}}} \sum_{b \in \mathcal{L}_{\text{tx}}} \mathbf{c}_c^H \mathbf{Z}_{\text{rx}}^H \mathbf{R} \mathbf{Z}_{\text{tx}} \mathbf{b}_b \cdot \pi_{b,c,t,s}|^2 + \sigma_{\text{sen}}^2 \sum_{c \in \mathcal{L}_{\text{rx}}} \|\mathbf{Z}_{\text{rx}} \mathbf{c}_c\|_2^2 \rho_{c,s}} \geq \bar{\Lambda}_{\text{sinr},t} \cdot \tau_{t,s}, \forall t \in \mathcal{T}, s \in \mathcal{S}$. Further manipulation allows $H_{\text{aux},1}$ to be recast as $H_{\text{aux},2} : \frac{1}{\sigma_{\text{sen}}^2} \min_{\theta_t \in \Theta_t} |\sum_{c \in \mathcal{L}_{\text{rx}}} \sum_{b \in \mathcal{L}_{\text{tx}}} \mathbf{c}_c^H \mathbf{Z}_{\text{rx}}^H \mathbf{A}(\theta_t) \mathbf{Z}_{\text{tx}} \mathbf{b}_b \cdot \pi_{b,c,t,s}|^2 \geq \frac{1}{\sigma_{\text{sen}}^2} \bar{\Lambda}_{\text{sinr},t} \cdot \tau_{t,s} \max_{\mathbf{R} \in \mathcal{R}} |\sum_{c \in \mathcal{L}_{\text{rx}}} \sum_{b \in \mathcal{L}_{\text{tx}}} \mathbf{c}_c^H \mathbf{Z}_{\text{rx}}^H \mathbf{R} \mathbf{Z}_{\text{tx}} \mathbf{b}_b \cdot \pi_{b,c,t,s}|^2 + \bar{\Lambda}_{\text{sinr},t} \cdot \tau_{t,s} \sum_{c \in \mathcal{L}_{\text{rx}}} \|\mathbf{Z}_{\text{rx}} \mathbf{c}_c\|_2^2 \rho_{c,s}, \forall t \in \mathcal{T}, s \in \mathcal{S}$.

Leveraging the transitivity property of inequalities, we introduce new variables $H_1 : z_{t,s} \geq 0, \forall t \in \mathcal{T}, s \in \mathcal{S}$, which allows us to decouple the LHS and RHS of $H_{\text{aux},2}$. This process yields $H_2 : \frac{1}{\sigma_{\text{sen}}^2} \min_{\theta_t \in \Theta_t} |\sum_{c \in \mathcal{L}_{\text{rx}}} \sum_{b \in \mathcal{L}_{\text{tx}}} \mathbf{c}_c^H \mathbf{Z}_{\text{rx}}^H \mathbf{A}(\theta_t) \mathbf{Z}_{\text{tx}} \mathbf{b}_b \cdot \pi_{b,c,t,s}|^2 \geq z_{t,s}, \forall t \in \mathcal{T}, s \in \mathcal{S}$, and $H_3 : \frac{1}{\sigma_{\text{sen}}^2} \bar{\Lambda}_{\text{sinr},t} \cdot \tau_{t,s} \cdot \max_{\mathbf{R} \in \mathcal{R}} |\sum_{c \in \mathcal{L}_{\text{rx}}} \sum_{b \in \mathcal{L}_{\text{tx}}} \mathbf{c}_c^H \mathbf{Z}_{\text{rx}}^H \mathbf{R} \mathbf{Z}_{\text{tx}} \mathbf{b}_b \cdot \pi_{b,c,t,s}|^2 + \bar{\Lambda}_{\text{sinr},t} \cdot \tau_{t,s} \sum_{c \in \mathcal{L}_{\text{rx}}} \|\mathbf{Z}_{\text{rx}} \mathbf{c}_c\|_2^2 \rho_{c,s} \leq z_{t,s}, \forall t \in \mathcal{T}, s \in \mathcal{S}$.

Additionally, to enforce that variable $z_{t,s}$ remains zero when T_t is not allocated S_s , we introduce constraint $H_4 : z_{t,s} \leq \tau_{t,s} \cdot \bar{M}_t^{\text{UB}}, \forall t \in \mathcal{T}, s \in \mathcal{S}$. Particularly, $\tau_{t,s} = 0$

forces $\pi_{b,c,t,s} = 0$, which in turn makes the LHS of H_2 zero. Here, \bar{M}_t^{UB} is an upper bound for $z_{t,s}$, obtained by maximizing the LHS term in H_2 , under the ideal assumption that there is no AOD error. It is defined as $\bar{M}_t^{\text{UB}} = \max_{b \in \mathcal{L}_{\text{tx}}} \max_{c \in \mathcal{L}_{\text{rx}}} \frac{|\mathbf{c}_c^H \mathbf{Z}_{\text{rx}}^H \mathbf{A}(\theta_t) \mathbf{Z}_{\text{tx}} \mathbf{b}_b|^2}{\sigma_{\text{sen}}^2}$.

APPENDIX L: PROOF TO PROPOSITION 6

To uncover hidden structural relationships within H_2 , we apply Jensen's inequality, which helps simplify the expression, revealing insights that may not be immediately apparent from the original form.

Considering arbitrary T_t and S_s , and applying Jensen's inequality we obtain $I_{\text{aux},1} : |\sum_{c \in \mathcal{L}_{\text{rx}}} \sum_{b \in \mathcal{L}_{\text{tx}}} \mathbf{c}_c^H \mathbf{Z}_{\text{rx}}^H \mathbf{A}(\theta_t) \mathbf{Z}_{\text{tx}} \mathbf{b}_b \cdot \pi_{b,c,t,s}|^2 \leq \sum_{c \in \mathcal{L}_{\text{rx}}} \sum_{b \in \mathcal{L}_{\text{tx}}} |\mathbf{c}_c^H \mathbf{Z}_{\text{rx}}^H \mathbf{A}(\theta_t) \mathbf{Z}_{\text{tx}} \mathbf{b}_b \cdot \pi_{b,c,t,s}|^2$. This result is derived by applying a procedure similar to that used in **Proposition 2**, where the analysis begins with the absolute value terms, followed by exponentiation and elimination of zero-valued terms.

If \mathbf{b}_i and \mathbf{c}_j denote the transmit and receive code-words for T_t in S_s , then $\chi_{i,s} = 1$ and $\rho_{j,s} = 1$, whereas $\chi_{b,s} = 0, \forall b \in \mathcal{L}_{\text{tx}} \setminus \{i\}$, and $\rho_{c,s} = 0, \forall c \in \mathcal{L}_{\text{rx}} \setminus \{j\}$, since only one transmit and one receive codeword can be chosen per timeslot when sensing is active. Selectively expanding the summations of both sides, $I_{\text{aux},1}$ is equivalent to $I_{\text{aux},2} : |\sum_{(c,b) \neq (j,i)} \mathbf{c}_c^H \mathbf{Z}_{\text{rx}}^H \mathbf{A}(\theta_t) \mathbf{Z}_{\text{tx}} \mathbf{b}_b \cdot \pi_{b,c,t,s} + \mathbf{c}_j^H \mathbf{Z}_{\text{rx}}^H \mathbf{A}(\theta_t) \mathbf{Z}_{\text{tx}} \mathbf{b}_i \cdot \pi_{i,j,t,s}|^2 \leq \sum_{(c,b) \neq (j,i)} |\mathbf{c}_c^H \mathbf{Z}_{\text{rx}}^H \mathbf{A}(\theta_t) \mathbf{Z}_{\text{tx}} \mathbf{b}_b \cdot \pi_{b,c,t,s}|^2 + |\mathbf{c}_j^H \mathbf{Z}_{\text{rx}}^H \mathbf{A}(\theta_t) \mathbf{Z}_{\text{tx}} \mathbf{b}_i \cdot \pi_{i,j,t,s}|^2$.

The terms affected under the summations are all zero, making $I_{\text{aux},2}$ hold at the equality and showing that Jensen's inequality is tight when applied to H_2 . Based on this outcome, we equivalently redefine H_2 as $I_{\text{aux},3} : \frac{1}{\sigma_{\text{sen}}^2} \min_{\theta_t \in \Theta_t} \sum_{c \in \mathcal{L}_{\text{rx}}} \sum_{b \in \mathcal{L}_{\text{tx}}} |\mathbf{c}_c^H \mathbf{Z}_{\text{rx}}^H \mathbf{A}(\theta_t) \mathbf{Z}_{\text{tx}} \mathbf{b}_b|^2 \pi_{b,c,t,s} \geq z_{t,s}, \forall t \in \mathcal{T}, s \in \mathcal{S}$, where $\pi_{b,c,t,s}$ can be factored out of the absolute value since it is binary.

Considering $\mathbf{d}_{b,c} = (\mathbf{Z}_{\text{tx}}^* \mathbf{b}_b^*) \otimes (\mathbf{Z}_{\text{rx}} \mathbf{c}_c)$ and $\mathbf{a}(\theta_t) = \text{vec}(\mathbf{A}(\theta_t))$, the equivalence $\mathbf{c}_c^H \mathbf{Z}_{\text{rx}}^H \mathbf{A}(\theta_t) \mathbf{Z}_{\text{tx}} \mathbf{b}_b = \mathbf{d}_{b,c}^H \mathbf{a}(\theta_t)$ holds. Hence, $I_{\text{aux},3}$ can be expressed as $I_{\text{aux},4} : \frac{1}{\sigma_{\text{sen}}^2} \min_{\theta_t \in \Theta_t} \sum_{c \in \mathcal{L}_{\text{rx}}} \sum_{b \in \mathcal{L}_{\text{tx}}} |\mathbf{d}_{b,c}^H \mathbf{a}(\theta_t)|^2 \pi_{b,c,t,s} \geq z_{t,s}, \forall t \in \mathcal{T}, s \in \mathcal{S}$. Employing (8) and C_{18} , constraint $I_{\text{aux},4}$ can be equivalently expressed as $I_{\text{aux},5} : \frac{1}{\sigma_{\text{sen}}^2} \min_{|\Delta\theta_t|^2 \leq \epsilon_{\text{AOD}}^2} \sum_{c \in \mathcal{L}_{\text{rx}}} \sum_{b \in \mathcal{L}_{\text{tx}}} |\mathbf{d}_{b,c}^H(\bar{\theta}_t) + \tilde{\mathbf{a}}(\bar{\theta}_t) \Delta\theta_t|^2 \pi_{b,c,t,s} \geq z_{t,s}, \forall t \in \mathcal{T}, s \in \mathcal{S}$, where $\mathbf{a}(\bar{\theta}_t) = \text{vec}(\mathbf{A}(\bar{\theta}_t))$ and $\tilde{\mathbf{a}}(\bar{\theta}_t) = \text{vec}(\tilde{\mathbf{A}}(\bar{\theta}_t))$.

We can separate $I_{\text{aux},5}$ into two constraints, specifically, $I_{\text{aux},6} : |\Delta\theta_t|^2 - \epsilon_{\text{AOD}}^2 \leq 0, \forall t \in \mathcal{T}$, and $I_{\text{aux},7} : z_{t,s} - \sum_{c \in \mathcal{L}_{\text{rx}}} \sum_{b \in \mathcal{L}_{\text{tx}}} \frac{1}{\sigma_{\text{sen}}^2} |\mathbf{d}_{b,c}^H(\mathbf{a}(\bar{\theta}_t) + \tilde{\mathbf{a}}(\bar{\theta}_t) \Delta\theta_t)|^2 \pi_{b,c,t,s} \leq 0, \forall t \in \mathcal{T}, s \in \mathcal{S}$.

Next, we apply **Lemma 2** to $I_{\text{aux},6}$ and $I_{\text{aux},7}$, leading to constraints I_1 and I_2 , shown below,

$$I_1 : \begin{bmatrix} i_{t,s}^a & i_{t,s}^b \\ i_{t,s}^c & i_{t,s}^d \end{bmatrix} \succcurlyeq \mathbf{0}, \forall t \in \mathcal{T}, s \in \mathcal{S},$$

$$I_2 : \xi_t \geq 0, \forall t \in \mathcal{T},$$

where $i_{t,s}^a = \xi_t - \tilde{\mathbf{a}}(\bar{\theta}_t)^H \mathbf{F}_{t,s} \tilde{\mathbf{a}}(\bar{\theta}_t)$, $i_{t,s}^b = -\tilde{\mathbf{a}}(\bar{\theta}_t)^H \mathbf{F}_{t,s} \mathbf{a}(\bar{\theta}_t)$, $i_{t,s}^c = -\mathbf{a}(\bar{\theta}_t)^H \mathbf{F}_{t,s} \tilde{\mathbf{a}}(\bar{\theta}_t)$, $i_{t,s}^d = -\xi_t \cdot \epsilon_{\text{AOD}}^2 - \mathbf{a}(\bar{\theta}_t)^H \mathbf{F}_{t,s} \mathbf{a}(\bar{\theta}_t) - z_{t,s}$, $\mathbf{F}_{t,s} = -\sum_{c \in \mathcal{L}_{\text{rx}}} \sum_{b \in \mathcal{L}_{\text{tx}}} \frac{1}{\sigma_{\text{sen}}^2} \mathbf{d}_{b,c} \mathbf{d}_{b,c}^H \pi_{b,c,t,s}$, and ξ_t are newly introduced variables needed by the *S-Procedure*.

APPENDIX M: PROOF TO PROPOSITION 7

Due to the complexity of H_3 , we begin by analyzing this constraint for arbitrary \mathcal{T}_t and \mathcal{S}_s . Assuming $\mathbf{d}_{b,c} = (\mathbf{Z}_{\text{tx}}^H \mathbf{b}_b^*) \otimes (\mathbf{Z}_{\text{rx}} \mathbf{c}_c)$ and $\mathbf{r} = \text{vec}(\mathbf{R})$, the equivalence $\mathbf{c}_c^H \mathbf{Z}_{\text{rx}}^H \mathbf{R} \mathbf{Z}_{\text{tx}} \mathbf{b}_b = \mathbf{d}_{b,c}^H \mathbf{r}$ holds. Hence, we have $J_{\text{aux},1} : \frac{1}{\sigma_{\text{sen}}^2} \bar{\Lambda}_{\text{sinr},t} \tau_{t,s} \cdot \max_{\mathbf{r} \in \mathcal{R}'} \left| \sum_{c \in \mathcal{L}_{\text{rx}}} \sum_{b \in \mathcal{L}_{\text{tx}}} \mathbf{d}_{b,c}^H \mathbf{r} \cdot \pi_{b,c,t,s} \right|^2 + \bar{\Lambda}_{\text{sinr},t} \tau_{t,s} \sum_{c \in \mathcal{L}_{\text{rx}}} \|\mathbf{Z}_{\text{rx}} \mathbf{c}_c\|_2^2 \rho_{c,s} \leq z_{t,s}$, where $\mathbf{r} = v\bar{\mathbf{r}} + v\Delta\mathbf{r}$, $\bar{\mathbf{r}} = \text{vec}(\bar{\mathbf{R}})$, $\Delta\mathbf{r} = \text{vec}(\Delta\mathbf{R})$, and $\mathcal{R}' \triangleq \{\mathbf{r} \mid \mathbf{r} = v\bar{\mathbf{r}} + v\Delta\mathbf{r}, \|\Delta\mathbf{r}\|_2^2 \leq \epsilon_{\text{RSI}}^2\}$.

Note that $\pi_{b,c,t,s}$ includes $\tau_{t,s}$, as detailed in **Proposition 3**. Hence, $\tau_{t,s}$ can be absorbed, transforming $J_{\text{aux},1}$ into $J_{\text{aux},2} : \frac{1}{\sigma_{\text{sen}}^2} \bar{\Lambda}_{\text{sinr},t} \max_{\mathbf{r} \in \mathcal{R}'} \left| \sum_{c \in \mathcal{L}_{\text{rx}}} \sum_{b \in \mathcal{L}_{\text{tx}}} \mathbf{d}_{b,c}^H \mathbf{r} \cdot \pi_{b,c,t,s} \right|^2 + \bar{\Lambda}_{\text{sinr},t} \tau_{t,s} \sum_{c \in \mathcal{L}_{\text{rx}}} \|\mathbf{Z}_{\text{rx}} \mathbf{c}_c\|_2^2 \rho_{c,s} \leq z_{t,s}$.

To uncover hidden relationships, we apply Jensen's inequality to the quadratic term on the LHS of $J_{\text{aux},2}$, which involves additive and multiplicative couplings among multiple variables. This leads us to $J_{\text{aux},3} : \left| \sum_{c \in \mathcal{L}_{\text{rx}}} \sum_{b \in \mathcal{L}_{\text{tx}}} \mathbf{d}_{b,c}^H \mathbf{r} \cdot \pi_{b,c,t,s} \right|^2 \leq \sum_{c \in \mathcal{L}_{\text{rx}}} \sum_{b \in \mathcal{L}_{\text{tx}}} |\mathbf{d}_{b,c}^H \mathbf{r} \cdot \pi_{b,c,t,s}|^2$. This result is obtained by first applying Jensen's inequality to the absolute value terms, followed by exponentiation and the elimination of zero-valued terms, in a manner similar to that used in **Proposition 2**.

Assuming that \mathbf{b}_i and \mathbf{c}_j are the selected transmit and receive codewords, we expand the summations, yielding $J_{\text{aux},4} : \left| \sum_{(c,b) \neq (j,i)} \mathbf{d}_{b,c}^H \mathbf{r} \cdot \pi_{b,c,t,s} + \mathbf{d}_{i,j}^H \mathbf{r} \cdot \pi_{i,j,t,s} \right|^2 \leq \sum_{(c,b) \neq (j,i)} |\mathbf{d}_{b,c}^H \mathbf{r} \cdot \pi_{b,c,t,s}|^2 + |\mathbf{d}_{i,j}^H \mathbf{r} \cdot \pi_{i,j,t,s}|^2$.

Since each target in an active timeslot can only be assigned one transmit/receive codeword pair, the terms under the summation vanish, ensuring that $J_{\text{aux},4}$ holds with equality. Additionally, $\pi_{b,c,t,s}$ can be factored out of the absolute value because it is binary. Consequently, we can reformulate $J_{\text{aux},1}$ as $J_{\text{aux},5} : \frac{1}{\sigma_{\text{sen}}^2} \bar{\Lambda}_{\text{sinr},t} \max_{\mathbf{r} \in \mathcal{R}'} \sum_{c \in \mathcal{L}_{\text{rx}}} \sum_{b \in \mathcal{L}_{\text{tx}}} |\mathbf{d}_{b,c}^H \mathbf{r}|^2 \pi_{b,c,t,s} + \bar{\Lambda}_{\text{sinr},t} \tau_{t,s} \sum_{c \in \mathcal{L}_{\text{rx}}} \|\mathbf{Z}_{\text{rx}} \mathbf{c}_c\|_2^2 \rho_{c,s} \leq z_{t,s}$, which is more amenable for further manipulation.

Next, we tackle the coupling between $\rho_{c,s}$ and $\tau_{t,s}$. Leveraging results from **Proposition 3**, we reformulate this coupling as an intersection of multiple constraints. Specifically, the product $\rho_{c,s} \tau_{t,s}$ can be re-expressed through the intersecting constraints, $J_1 : \delta_{c,t,s} \leq \rho_{c,s}, \forall c \in \mathcal{L}_{\text{rx}}, t \in$

$\mathcal{T}, s \in \mathcal{S}, J_2 : \delta_{c,t,s} \leq \tau_{t,s}, \forall c \in \mathcal{L}_{\text{rx}}, t \in \mathcal{T}, s \in \mathcal{S}$, and $J_3 : \delta_{c,t,s} \geq \rho_{c,s} + \tau_{t,s} - 1, \forall c \in \mathcal{L}_{\text{rx}}, t \in \mathcal{T}, s \in \mathcal{S}$, enabling a more tractable optimization approach⁷. Here, $\delta_{c,t,s}$ are newly introduced variables that, by definition, must be binary. However, we can relax $\delta_{c,t,s}$ to a continuous variable to reduce the number of binary variables, thereby lowering computational complexity of the binary search process. To enforce its binary nature in all cases, we impose constraint $J_4 : \delta_{c,t,s} \in [0, 1], \forall c \in \mathcal{L}_{\text{rx}}, t \in \mathcal{T}, s \in \mathcal{S}$.

Leveraging the results in $J_{\text{aux},5}$, we generalize for all targets and timeslots, allowing us to recast H_3 as $J_{\text{aux},6} : \frac{1}{\sigma_{\text{sen}}^2} \bar{\Lambda}_{\text{sinr},t} \max_{\mathbf{r} \in \mathcal{R}'} \sum_{c \in \mathcal{L}_{\text{rx}}} \sum_{b \in \mathcal{L}_{\text{tx}}} |\mathbf{d}_{b,c}^H \mathbf{r}|^2 \pi_{b,c,t,s} + \bar{\Lambda}_{\text{sinr},t} \sum_{c \in \mathcal{L}_{\text{rx}}} \|\mathbf{Z}_{\text{rx}} \mathbf{c}_c\|_2^2 \delta_{c,t,s} \leq z_{t,s}, \forall t \in \mathcal{T}, s \in \mathcal{S}$.

Note that we can express $J_{\text{aux},6}$ as $J_{\text{aux},7} : \frac{1}{\sigma_{\text{sen}}^2} \bar{\Lambda}_{\text{sinr},t} \cdot \max_{\Delta\mathbf{r}} \|\Delta\mathbf{r}\|_2^2 \leq \epsilon_{\text{RSI}}^2 \sum_{c \in \mathcal{L}_{\text{rx}}} \sum_{b \in \mathcal{L}_{\text{tx}}} |\mathbf{d}_{b,c}^H (v\bar{\mathbf{r}} + v\Delta\mathbf{r})|^2 \pi_{b,c,t,s} + \bar{\Lambda}_{\text{sinr},t} \sum_{c \in \mathcal{L}_{\text{rx}}} \|\mathbf{Z}_{\text{rx}} \mathbf{c}_c\|_2^2 \delta_{c,t,s} \leq z_{t,s}, \forall t \in \mathcal{T}, s \in \mathcal{S}$, after letting $J_{\text{aux},6}$ absorb \mathcal{R}' . Here, $J_{\text{aux},7}$ can be split into $J_{\text{aux},8} : \Delta\mathbf{r}^H \Delta\mathbf{r} - \epsilon_{\text{RSI}}^2 \leq 0$ and $J_{\text{aux},9} : \frac{1}{\sigma_{\text{sen}}^2} \bar{\Lambda}_{\text{sinr},t} \cdot \sum_{c \in \mathcal{L}_{\text{rx}}} \sum_{b \in \mathcal{L}_{\text{tx}}} |\mathbf{d}_{b,c}^H (v\bar{\mathbf{r}} + v\Delta\mathbf{r})|^2 \pi_{b,c,t,s} + \bar{\Lambda}_{\text{sinr},t} \sum_{c \in \mathcal{L}_{\text{rx}}} \|\mathbf{Z}_{\text{rx}} \mathbf{c}_c\|_2^2 \delta_{c,t,s} - z_{t,s} \leq 0, \forall t \in \mathcal{T}, s \in \mathcal{S}$.

Applying **Lemma 2** to $J_{\text{aux},8}$ and $J_{\text{aux},9}$, leads to constraints J_5 and J_6 , shown below,

$$J_5 : \begin{bmatrix} \mathbf{j}_{t,s}^a & \mathbf{j}_{t,s}^b \\ \mathbf{j}_{t,s}^c & \mathbf{j}_{t,s}^d \end{bmatrix} \succcurlyeq \mathbf{0}, \forall t \in \mathcal{T}, s \in \mathcal{S},$$

$$J_6 : \iota \geq 0,$$

where $\mathbf{j}_{t,s}^a = \iota \mathbf{I} + v^2 \bar{\Lambda}_{\text{sinr},t} \mathbf{F}_{t,s}$, $\mathbf{j}_{t,s}^b = v^2 \bar{\Lambda}_{\text{sinr},t} \mathbf{F}_{t,s} \bar{\mathbf{r}}$, $\mathbf{j}_{t,s}^c = v^2 \bar{\Lambda}_{\text{sinr},t} \bar{\mathbf{r}}^H \mathbf{F}_{t,s}$, $\mathbf{j}_{t,s}^d = -\iota \cdot \epsilon_{\text{RSI}}^2 + v^2 \bar{\Lambda}_{\text{sinr},t} \bar{\mathbf{r}}^H \mathbf{F}_{t,s} \bar{\mathbf{r}} - \bar{\Lambda}_{\text{sinr},t} \sum_{c \in \mathcal{L}_{\text{rx}}} \|\mathbf{Z}_{\text{rx}} \mathbf{c}_c\|_2^2 \delta_{c,t,s} + z_{t,s}$, $\mathbf{F}_{t,s} = -\sum_{c \in \mathcal{L}_{\text{rx}}} \sum_{b \in \mathcal{L}_{\text{tx}}} \frac{1}{\sigma_{\text{sen}}^2} \mathbf{d}_{b,c} \mathbf{d}_{b,c}^H \pi_{b,c,t,s}$, and ι is a newly introduced variable needed by the *S-Procedure*.

APPENDIX N: PROOF TO PROPOSITION 8

Since $f_1(\Omega)$ and $f_2(\Omega)$ depend on binary variables constrained to $\{0, 1\}$, we can analyze their extremal values and derive optimal weights η_1 and η_2 that enforce a strict prioritization, specifically, favoring the minimization of time consumption over energy expenditure.

Let $P_{\text{tx}}^{\text{max}}$ and $P_{\text{rx}}^{\text{max}}$ denote the maximum transmit and receive powers, respectively, and $P_{\text{tx}}^{\text{min}}$ and $P_{\text{rx}}^{\text{min}}$ their minimum counterparts. Thus, for a single active timeslot, $f_1(\Omega)$ lies in the interval $[S_{\text{dur}} P_{\text{tx}}^{\text{min}} + S_{\text{dur}} P_{\text{rx}}^{\text{min}}, S_{\text{dur}} P_{\text{tx}}^{\text{max}} + S_{\text{dur}} P_{\text{rx}}^{\text{max}}]$. Extending this to all timeslots, $f_1(\Omega)$ is in the interval $[S' S_{\text{dur}} P_{\text{tx}}^{\text{min}} + S' S_{\text{dur}} P_{\text{rx}}^{\text{min}}, S' S_{\text{dur}} P_{\text{tx}}^{\text{max}} + S' S_{\text{dur}} P_{\text{rx}}^{\text{max}}]$, where $S' \leq S$ is the number of active timeslots.

Meanwhile, function $f_2(\Omega)$ takes values in the interval $[r_1, r_2]$, where $r_1 = S_{\text{dur}} \Delta_0$ and $r_2 = S_{\text{dur}} S' \Delta_0 + S_{\text{dur}} \frac{\Delta_\omega}{2} (S' - 2)(S' - 1)$. Here, r_2 corresponds to the cumulative sum of all weights ω_s , as defined in **Lemma 1**, over S' timeslots.

Notably, the images of $f_1(\Omega)$ and $f_2(\Omega)$ may overlap depending on the values of S_{dur} , $P_{\text{tx}}^{\text{min}}$, $P_{\text{rx}}^{\text{min}}$, $P_{\text{tx}}^{\text{max}}$, $P_{\text{rx}}^{\text{max}}$, Δ_0 , and Δ_ω . To ensure completely non-overlapping intervals for the images of these functions and a strict

7. Constraints J_1 , J_2 , and J_3 can be directly derived from **Proposition 3** by setting one of the binary variables to 1.

prioritization of $f_2(\Omega)$, we impose the condition $\eta_2 f_2(\Omega) > \eta_1 f_1(\Omega)$, where η_1 and η_2 are weighting coefficients.

For simplicity, we consider the extreme case where the minimum value of $\eta_2 f_2$ (i.e., $\eta_2 S_{\text{dur}} \Delta_0$) must exceed the maximum value of $\eta_1 f_1$ (i.e., $\eta_1 S S_{\text{dur}} P_{\text{tx}}^{\text{max}} + \eta_1 S S_{\text{dur}} P_{\text{rx}}^{\text{max}}$), occurring when $S' = S$. This leads to the sufficient condition

$$\eta_2 > \eta_1 \frac{S(P_{\text{tx}}^{\text{max}} + P_{\text{rx}}^{\text{max}})}{\Delta_0}.$$

We now address the complexity of $f_1(\Omega)$, which arises from its quadratic terms. In contrast, $f_2(\Omega)$ is linear and straightforward to handle.

Given the structural similarity between the terms $\sum_{s \in S} \|\mathbf{w}_s\|_2^2$ and $\sum_{s \in S} \|\mathbf{v}_s\|_2^2$, we start by analyzing the first term and later extend the approach to the second. Let us focus on an arbitrary S_s . Using the definition in C_{11} , we have $\|\mathbf{w}_s\|_2^2 = \mathbf{w}_s^H \mathbf{w}_s = \left(\sum_{b \in \mathcal{L}_{\text{tx}}} \mathbf{b}_b \cdot \chi_{b,s} \right)^H \left(\sum_{b' \in \mathcal{L}_{\text{tx}}} \mathbf{b}_{b'} \cdot \chi_{b',s} \right) = \sum_{b \in \mathcal{L}_{\text{tx}}} \sum_{b' \in \mathcal{L}_{\text{tx}}} \mathbf{b}_b^H \mathbf{b}_{b'} \cdot \chi_{b,s} \chi_{b',s}$.

Employing C_{10} , we distinguish two cases, which we leverage to simplify the expression above, as shown in the following.

Case ① \Rightarrow If S_s is idle, i.e., $\gamma_s = 0$, then $\sum_{b \in \mathcal{L}_{\text{tx}}} \chi_{b,s} = 0$, which implies that $\chi_{b,s} = 0, \forall b \in \mathcal{L}_{\text{tx}}$, ensuring that no codeword is selected in S_s . Hence, $\|\mathbf{w}_s\|_2^2 = 0$.

Case ② \Rightarrow If S_s is active, i.e., $\gamma_s = 1$, then $\sum_{b \in \mathcal{L}_{\text{tx}}} \chi_{b,s} = 1$, which implies that $\chi_{i,s} = 1$ and $\chi_{b,s} = 0, \forall b \in \mathcal{L}_{\text{tx}} \setminus \{i\}$, assuming that \mathbf{b}_i denotes the selected codeword. Hence, $\|\mathbf{w}_s\|_2^2 = \sum_{(b,b') \neq (i,i)} \mathbf{b}_b^H \mathbf{b}_{b'} \cdot \chi_{b,s} \chi_{b',s} + \mathbf{b}_i^H \mathbf{b}_i \cdot \chi_{i,s} \chi_{i,s}$. The term under the summation yields zero, thereby resulting in $\|\mathbf{w}_s\|_2^2 = \mathbf{b}_i^H \mathbf{b}_i$.

We can combine the two cases above, resulting in $\|\mathbf{w}_s\|_2^2 = \sum_{b \in \mathcal{L}_{\text{tx}}} \|\mathbf{b}_b\|_2^2 \cdot \chi_{b,s}$. Employing C_{13} and C_{14} , and following a similar procedure as above, we obtain $\|\mathbf{v}_s\|_2^2 = \sum_{c \in \mathcal{L}_{\text{rx}}} \|\mathbf{c}_c\|_2^2 \cdot \rho_{c,s}$. As a result, we redefine $f_1(\Omega)$ as $f'_1(\Omega') = S_{\text{dur}} \sum_{s \in S} \sum_{b \in \mathcal{L}_{\text{tx}}} \|\mathbf{b}_b\|_2^2 \cdot \chi_{b,s} + S_{\text{dur}} \sum_{s \in S} \sum_{c \in \mathcal{L}_{\text{rx}}} \|\mathbf{c}_c\|_2^2 \cdot \rho_{c,s}$, which leads to $f'(\Omega') \triangleq \eta_1 f'_1(\Omega') + \eta_2 f'_2(\Omega')$, assuming $f'_2(\Omega') = f_2(\Omega)$.

APPENDIX O: DERIVATION OF CUTTING PLANES

To eliminate infeasible solutions without exhaustively searching for the optimal transmit codeword, we derive an upper bound for the numerator of (4), which helps prune reduce infeasible solutions.

Specifically, when user U_u is served in S_s , the power of the signal received by the user is given by $K_{\text{aux},1} : |\mathbf{h}_u^H \mathbf{Z}_{\text{tx}} \mathbf{w}_s|^2 = |(\bar{\mathbf{h}}_u^H + \Delta \mathbf{h}_u^H) \mathbf{Z}_{\text{tx}} \mathbf{w}_s|^2$, where $\Delta \mathbf{h}_u$ denotes the channel perturbation.

Applying the triangle inequality and the Cauchy-Schwarz inequality twice, the highest received signal power with respect to the CSI uncertainty can be upper bounded as $|(\bar{\mathbf{h}}_u^H + \Delta \mathbf{h}_u^H) \mathbf{Z}_{\text{tx}} \mathbf{w}_s| \leq |\bar{\mathbf{h}}_u^H \mathbf{Z}_{\text{tx}} \mathbf{w}_s| + \epsilon_{\text{CSI}} \|\mathbf{Z}_{\text{tx}} \mathbf{w}_s\|_2 \leq |\bar{\mathbf{h}}_u^H \mathbf{Z}_{\text{tx}} \mathbf{w}_s| + \epsilon_{\text{CSI}} \|\mathbf{Z}_{\text{tx}}\|_{\text{F}} \|\mathbf{w}_s\|_2$. Hence, an upper bound for $K_{\text{aux},1}$ is expressed by the relation: $K_{\text{aux},2} : |\mathbf{h}_u^H \mathbf{Z}_{\text{tx}} \mathbf{w}_s|^2 \leq (|\bar{\mathbf{h}}_u^H \mathbf{Z}_{\text{tx}} \mathbf{w}_s| + \epsilon_{\text{CSI}} \|\mathbf{Z}_{\text{tx}}\|_{\text{F}} \|\mathbf{w}_s\|_2)^2$.

Next, we maximize the RHS term of $K_{\text{aux},2}$ with respect to the beamformer \mathbf{w}_s . The term is maximized when \mathbf{w}_s is chosen to be colinear with $\mathbf{Z}_{\text{tx}}^H \bar{\mathbf{h}}_u$, i.e., $\mathbf{w}_s =$

$\frac{\mathbf{Z}_{\text{tx}}^H \bar{\mathbf{h}}_u}{\|\mathbf{Z}_{\text{tx}}^H \bar{\mathbf{h}}_u\|_2} \sqrt{P_{\text{tx}}^{\text{max}}}$, where $P_{\text{tx}}^{\text{max}}$ denotes the maximum transmit power at the BS, i.e., $P_{\text{tx}}^{\text{max}} = \max_{b \in \mathcal{L}_{\text{tx}}} \|\mathbf{b}_b\|_2^2$.

Under this choice, the maximum received signal power admits the upper bound $K_{\text{aux},3} : (\|\mathbf{Z}_{\text{tx}}^H \bar{\mathbf{h}}_u\|_2 + \epsilon_{\text{CSI}} \|\mathbf{Z}_{\text{tx}}\|_{\text{F}})^2 P_{\text{tx}}^{\text{max}}$. Consequently, we obtain the following cutting plane, $K_1 : |\mathbf{h}_u^H \mathbf{Z}_{\text{tx}} \mathbf{w}_s|^2 \leq (\|\mathbf{Z}_{\text{tx}}^H \bar{\mathbf{h}}_u\|_2 + \epsilon_{\text{CSI}} \|\mathbf{Z}_{\text{tx}}\|_{\text{F}})^2 P_{\text{tx}}^{\text{max}}$.

To further eliminate equally optimal solutions that differ only in the temporal order of user and target assignments, we introduce an additional cutting plane. Specifically, we define constraint $K_{\text{aux},4} : \|\mathbf{w}_{s+1}\|_2^2 + \|\mathbf{v}_{s+1}\|_2^2 \geq \|\mathbf{w}_s\|_2^2 + \|\mathbf{v}_s\|_2^2, \forall s \in S \setminus \{S\}$, which enforces that the total transmit power does not increase over successive time slots. This constraint introduces a temporal ordering to the allocation, reducing redundant permutations that yield the same objective value.

To address the quadratic terms in $K_{\text{aux},4}$, we leverage the relationships derived in **Appendix N**, which allow for a simplification of these expressions. As a result $K_{\text{aux},4}$ can be reformulated into a more tractable form, denoted as $K_2 : \sum_{b \in \mathcal{L}_{\text{tx}}} \|\mathbf{b}_b\|_2^2 \cdot \chi_{b,s+1} + \sum_{c \in \mathcal{L}_{\text{rx}}} \|\mathbf{c}_c\|_2^2 \cdot \rho_{c,s+1} \geq \sum_{b \in \mathcal{L}_{\text{tx}}} \|\mathbf{b}_b\|_2^2 \cdot \chi_{b,s} + \sum_{c \in \mathcal{L}_{\text{rx}}} \|\mathbf{c}_c\|_2^2 \cdot \rho_{c,s}, \forall s \in S \setminus \{S\}$, yielding a simplified version of the cutting plane.

APPENDIX P: TRANSFORMED PROBLEM

For completeness, the problem $\mathcal{P}'(\Omega')$, with all constraints explicitly detailed, is presented in the next page.

APPENDIX Q: IMPACT OF TIMESLOT REQUIREMENTS AND TRADEOFF WEIGHTS

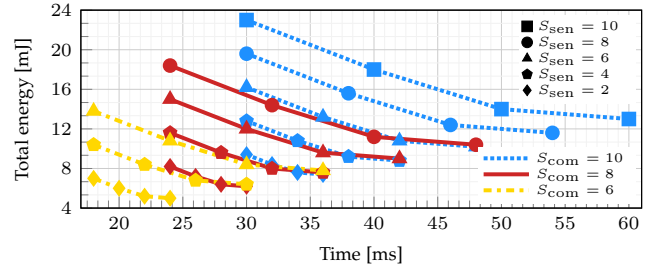


Fig. 10: Impact of timeslot requirements and tradeoff weights on resource economy (Scenario VIII). Weight selection serves as an effective mechanism to navigate the tradeoff between energy and time consumption. Also, the chosen weights implicitly influence whether joint or individual servicing of users and targets is favored. Finally, both energy and time consumption scale with the total timeslot requirements.

In this scenario, we investigate how varying timeslot requirements influence both energy and time consumption. Unlike previous scenarios, which prioritized minimizing time consumption through specific weight selections (η_1 and η_2), we now explore a broader range of weight configurations to illustrate the tradeoff between energy and time across diverse priority settings. We consider $U = 3, T = 3, S_{\text{com}} = \{6, 8, 10\}$, and $S_{\text{sen}} = \{2, 4, 6, 8, 10\}$. The detailed parameter setting is shown in Table B.1.

$$\begin{aligned}
 \mathcal{P}'(\Omega') : \min_{\Omega'} & \quad f'(\Omega') \\
 \text{s.t.} & \quad C_1 : \kappa_s = \{0, 1\}, \forall s, \\
 & \quad C_2 : \zeta_s = \{0, 1\}, \forall s, \\
 & \quad C_4 : \sum_{s \in \mathcal{S}} \gamma_s \leq S, \\
 & \quad C_5 : \mu_{u,s} \in \{0, 1\}, \forall u, s, \\
 & \quad C_6 : \kappa_s = \sum_{u \in \mathcal{U}} \mu_{u,s}, \forall s, \\
 & \quad C_7 : \tau_{t,s} \in \{0, 1\}, \forall t, s, \\
 & \quad C_8 : \zeta_s = \sum_{t \in \mathcal{T}} \tau_{t,s}, \forall s, \\
 & \quad C_9 : \chi_{b,s} \in \{0, 1\}, \forall b, s, \\
 & \quad C_{10} : \sum_{b \in \mathcal{L}_{\text{tx}}} \chi_{b,s} = \gamma_s, \forall s, \\
 & \quad C_{12} : \rho_{c,s} \in \{0, 1\}, \forall c, s, \\
 & \quad C_{13} : \sum_{c \in \mathcal{L}_{\text{rx}}} \rho_{c,s} = \zeta_s, \forall s, \\
 & \quad C_{17} : \sum_{s \in \mathcal{S}} \mu_{u,s} = S_{\text{com},u}, \forall u, \\
 & \quad C_{22} : \sum_{s \in \mathcal{S}} \tau_{t,s} = S_{\text{sent},t}, \forall t, \\
 & \quad D_1 : \gamma_s \leq \kappa_s + \zeta_s, \forall s, \\
 & \quad D_2 : \gamma_s \geq \kappa_s, \forall s, \\
 & \quad D_3 : \gamma_s \geq \zeta_s, \forall s, \\
 & \quad D_4 : \gamma_s \leq 1, \forall s, \\
 & \quad E_1 : \begin{bmatrix} \mathbf{E}_{u,s}^a & \mathbf{e}_{u,s}^b \\ \mathbf{e}_{u,s}^c & e_{u,s}^d \end{bmatrix} \succcurlyeq \mathbf{0}, \forall u, s, \\
 & \quad E_2 : \alpha_u \geq 0, \forall u, \\
 & \quad F_1 : \chi_{b,s} \geq \pi_{b,c,t,s}, \forall b, c, t, s, \\
 & \quad F_2 : \rho_{c,s} \geq \pi_{b,c,t,s}, \forall b, c, t, s, \\
 & \quad F_3 : \tau_{t,s} \geq \pi_{b,c,t,s}, \forall b, c, t, s, \\
 & \quad F_4 : 2 + \pi_{b,c,t,s} \geq \chi_{b,s} + \rho_{c,s} + \tau_{t,s}, \forall b, c, t, s, \\
 & \quad F_5 : \pi_{b,c,t,s} \in [0, 1], \forall b, c, t, s, \\
 & \quad H_1 : z_{t,s} \geq 0, \forall t, s, \\
 & \quad H_4 : z_{t,s} \leq \tau_{t,s} \cdot \ddot{M}_t^{\text{UB}}, \forall t, s, \\
 & \quad I_1 : \begin{bmatrix} i_{t,s}^a & i_{t,s}^b \\ i_{t,s}^c & i_{t,s}^d \end{bmatrix} \succcurlyeq \mathbf{0}, \forall t, s, \\
 & \quad I_2 : \xi_t \geq 0, \forall t, \\
 & \quad J_1 : \delta_{c,t,s} \leq \rho_{c,s}, \forall c, t, s, \\
 & \quad J_2 : \delta_{c,t,s} \leq \tau_{t,s}, \forall c, t, s, \\
 & \quad J_3 : \delta_{c,t,s} \geq \rho_{c,s} + \tau_{t,s} - 1, \forall c, t, s, \\
 & \quad J_4 : \delta_{c,t,s} \geq 0, \forall c, t, s, \\
 & \quad J_5 : \begin{bmatrix} \mathbf{J}_{t,s}^a & \mathbf{j}_{t,s}^b \\ \mathbf{j}_{t,s}^c & j_{t,s}^d \end{bmatrix} \succcurlyeq \mathbf{0}, \forall t, s, \\
 & \quad J_6 : \iota \geq 0. \\
 & \quad K_1 : \left| \mathbf{h}_u^H \mathbf{w}_s \right|^2 \leq \ddot{M}_u^{\text{UB}}, \forall u \in \mathcal{U}, s \in \mathcal{S}, \\
 & \quad K_2 : \bar{\ell}_{s+1}(\Omega') \geq \bar{\ell}_s(\Omega'), \forall s \in \mathcal{S} \setminus \{S\}.
 \end{aligned}$$

a strong emphasis on minimizing time consumption and little regard for energy, while the rightmost points prioritize energy minimization at the expense of time. Notably, the leftmost allocations typically favor joint servicing of users and targets, resulting in fewer active timeslots. In contrast, the rightmost allocations tend to assign separate timeslots to users and targets to minimize energy consumption, particularly in cases of poor alignment.

Each curve in Fig. 10 is generated by varying the weights η_1 and η_2 , thereby adjusting the relative importance assigned to energy and time consumption. For any given curve, the leftmost points represent configurations with

TABLE B.1: Simulation parameters.

Scenario	U	T	S_{com}	S_{sen}	S	β_u	$\theta_t \mid \bar{\theta}_t$	r_u	$\psi_t \mid \bar{\psi}_t$	Υ_{snr}	Λ_{sinr}	$\frac{\epsilon_{\text{CSI}}}{\sigma_{\text{com}}}$	ϵ_{AOD}	$\frac{\epsilon_{\text{RC}}}{\psi}$	$\frac{\epsilon_{\text{RSI}}}{\ \mathbf{R}\ _F}$	v	\bar{d}_c
VIII	3	3	[6, 10]	[2, 10]	60	[50, 85]	[75, 100]	[40, 60]	[8, 12] 10^{-4}	50	2	0	0	0	0	0	—